Energy Harvesting from the Human Body for Wearable and Mobile Devices

Mingyi Liu

Dissertation submitted to the Faculty of the
Virginia Polytechnic Institute and State University
in partial fulfillment of the requirements for the degree of

Doctor of Philosophy
in
Mechanical Engineering

Lei Zuo, Chair
Robin M. Queen, Co-chair
Muhammad R. Hajj
Roop L. Mahajan
Rober G. Parker
Wei-Che Tai

May, 13, 2020
Blacksburg, Virginia

Keywords: energy harvesting, human body, backpack, negative muscle work, ankle energy harvester, energy harvesting tile/paver
Copyright 2020, Mingyi Liu

Energy Harvesting from the Human Body for Wearable and Mobile Devices

Mingyi Liu

ABSTRACT

Wearable and mobile devices are an important part of our daily life. Most of those devices are powered by batteries. The limited life span of batteries constitutes a limitation, especially in a multiple-day expedition, where electrical power can not access conveniently. At the same time, there is a huge amount of energy stored in the human body. While walking, there is a large amount of power dissipated in the human body as negative muscle work and the energy loss by impact. By sourcing locally and using locally, human body energy harvesting is a promising solution. This dissertation focuses on harvesting energy from the human body to power wearable and mobile devices while poses a minimum burden on the human body. Three topics related to the human body energy harvesting are explored, i.e, energy harvesting backpack, negative muscle work harvester, and energy harvesting tile/paver. The energy harvesting backpack was invented in 2006. Extensive work was done to improve the performance of backpack energy harvester. The backpack is modeled as a spring-mass-damper system. Mechanical Motion Rectifier was added to the spring-mass-damper system to increase the frequency bandwidth. A spring is added to the spring-mass-damper system, between the harvester and the backpack mass, and a inerter-based 2DOF (degree-of-freedom) backpack is created. The inerter-based 2DOF backpack improves the power output, frequency bandwidth, and power stroke ratio performance. MMR was added to the inerter-based 2DOF backpack to reduce the peak stroke. Compared with the conventional spring-mass-damper backpack, the MMR and inerter-based 2DOF backpack can harvest more power with large bandwidth at a small sacrifice of stroke. The electric damping was also tuned to increase the power output and bandwidth for the energy harvesting backpack. The negative work harvester mounts on the human ankle and harvests energy in the terminal stance phase in human walking, when the calf muscle is doing negative muscle work. This harvester is an analogy to regenerative brake in vehicles. The energy harvesting paver/tile harvests energy when the heel contacts with ground and energy are dissipated by impact.

Keywords: energy harvesting, human body, backpack, negative muscle work, ankle energy harvester, energy harvesting tile/paver

Energy Harvesting from the Human Body for Wearable and Mobile Devices

Mingyi Liu

GENERAL AUDIENCE ABSTRACT

Wearable and mobile devices are an important part of our daily life. Most of those devices are powered by batteries. The limited life span of batteries constitutes a limitation, especially in a multiple-day expedition, where electrical power can not access conveniently. At the same time, there is a huge amount of energy stored in the human body. While walking, there is a large amount of power dissipated in the human body as negative muscle work and the energy loss by impact. By sourcing locally and using locally, human body energy harvesting is a promising solution. This dissertation focuses on harvesting energy from the human body to power wearable and mobile devices while minimize burden on the human body. Three topics related to the human body energy harvesting are explored, i.e, energy harvesting backpack, negative muscle work harvester, and energy harvesting tile/paver. The energy harvesting backpack was invented in 2006. Extensive work was done to improve the performance of backpack energy harvester. Innovation mechanical design was done in this dissertation to make the energy harvesting backpack perform well in various walking speeds. At the same time, the backpack oscillation stroke is also limited. A ankle energy harvester was designed and harvests negative muscle work. This harvester is an analogy to regenerative brake in vehicles. The energy harvesting paver/tile harvests energy when the heel contacts with ground and energy are dissipated by impact.

Keywords: energy harvesting, human body, backpack, negative muscle work, ankle energy harvester, energy harvesting tile/paver

Dedication

To my father, who worked so hard to provide me and my four siblings with everything we need to thrive.

Acknowledgments

The research presented in this dissertation received support from the U.S. Army Communications-Electronics Research, Development and Engineering Center (CERDEC) via GTS-S-16-041, U.S. Navy Office of Naval Research (ONR) via N00014-18-1-2190, National Science Foundation (NSF) via 1530122 and 1530508, Virginia Tech Institute for Critical Technology and Applied Science (VT ICTAS), Virginia Tech Student Engineers' Council (VT SEC), and VT Drillfield Path project. I am grateful for all the funding support listed above.

It is a long journey for me to finish my Ph.D., starting from 2014. I am in debt to many people. I could not do it without them.

First of all, I could not do my Ph.D. without the support of my adviser, Prof. Lei Zuo. He provided me not only guidance but also financial support. With his support, I had two babies while studying my Ph.D.

I am also in deep gratitude with my co-advisor, Prof. Robin Queen. Dr. Queen guided me into the human body dynamics world. She also helped me a lot in the energy harvesting device design.

Dr. Tai was a Post-doc in the Energy Harvesting lab when I first start my Ph.D. and he leads the projects. Dr. Tai is not only a great mentor but also a role model. He showed me how to be successful in academics.

I am also grateful for the advice, critics, and suggestions from my dissertation committee. Dr. Rober Park always has a sharp mind and leads me to do critical thinking. Dr. Roop Mahajan is visionary and inspiring. Dr. Mahajan always guides me to think about my scientific contribution. Prof. Muhammad Hajj and Prof. Margarita McGrath lead the tile/paver project and we spend a lot of time together. I am grateful for the advice day in and day out. Although I did not make it, I am still grateful for the support from Prof. Kevin Davy, Glen Reid, and Cherice Hughes-Oliver for

their support on the human experiment.

I would like to thank Dr. Rolf Mueller for support and introduce Virginia Tech to me. I appreciate Dr. Rolf Mueller, Dr. Michael Garvin, and Dr. Moore Ignacio for bring biology and bio-inspired technology to me. I might be disappointing for them, but bio-inspired will be carved in my mind and I will always looking into opportunities in bio-inspired.

I am grateful for the support of my family. My mom and my parents in law come to help us taking care of the babies, while both my wife and I can focus on study.

While I am studying here in the U.S.A., my brother, sisters, and in-laws, all support me from China.

To my son James, and my daughter Alice, and all the nices/nephews, thank you for sharing your passion for life and showing me hope for the future.

Although he is not with me, I am thinking of my father all the time, wherever I go. This gives me endless strength.

To my grandfather, I am sorry I can not be with you for the past 6 years. Looking forward to bring my kids to you and let's share the big moment.

To all my friends and family in Blacksburg that I can not come up with a complete list, thank you for sharing your life with me. I will miss all of you.

Last but certainly not least, for my wife Yingying. I am so fortunate to have you. I am looking forward to the next 70 years with you.

Contents

1 Introduction **1**

1.1 Background 1

1.2 Objective and contribution of this dissertation 7

1.3 Dissertation organization 10

2 Mechanical Motion Rectify based Energy Harvesting Backpack **11**

2.1 Chapter introduction 11

2.2 Influence of inerter on energy harvesting performance 14

2.3 Concept, design, and modeling of MMR based energy harvester . . . 20

2.3.1 Concept and design 20

2.3.2 System modeling 22

2.3.3 Equivalent Electrical Model 24

2.4 Simulation the influence of MMR on energy harvesting 25

2.5 Experiment verification of MMR based energy harvesting 27

2.5.1 Experiment set up and parameter identification 27

2.5.2 Experiment validation 30

2.5.3 Influence of MMR on force profile 33

2.6 Difference between experiment and modeling 35

2.7 Backpack energy harvester experiment with human subjects 37

2.8 Why MMR can increase the energy harvesting frequency bandwidth . 39
2.9 Performance of MMR in systems under excitation with constant force amplitude 43

3 Two-degree-of-freedom based Energy Harvesting Backpack 48
3.1 Chapter introduction 48
3.2 Performance limitations of SDOF harvesters 51
3.3 Design and Modeling of inerter-based 2DOF energy harvesting system 55
3.4 Analysis and optimization 57
3.5 Experiment validation 58
3.6 Discussions 60
3.6.1 Force-displacement profile of inerter-based 2DOF system . . . 60
3.6.2 Influence of the mechanical damping ξ_m and mass ratio μ at the target frequency with stroke limit 61
3.6.3 Power output of the inerter-based 2DOF system at target frequency can be large by tuning the springs 62
3.6.4 Influence of mass ratio μ on bandwidth 64
3.6.5 Inerter-based 2DOF system vs. conventional 2DOF energy harvesting system 65
3.6.6 Inerter-based 2DOF system vs. conventional 2DOF system . . 66

4 MMR Based 2DOF Backpack Energy Harvesting System 70
4.1 Chapter introduction 70
4.2 Motivation of adding MMR to the system 72
4.3 MMR based nonlinear inerter system design 74
4.4 Simulation 76
4.5 Optimization 79
4.6 Experiment validation 82

4.7 Discussion 85

5 Negative Muscle Work Energy Harvester 89

5.1 Chapter introduction 89

5.2 Negative work in the ankle during human walking 92

5.3 Design of negative work ankle energy harvester 96

5.4 Modeling 100

5.5 Experiment validation 103

5.6 Discussion 110

5.7 Appendix 111

6 Energy Harvesting tile/paver 113

6.1 Chapter introduction 113

6.2 Concept, design and prototype 116

6.2.1 Concept 116

6.2.2 Design and prototype 117

6.3 Modeling and simulation 118

6.3.1 Potential Energy 118

6.3.2 Overall model 120

6.3.3 Simulation and parameter optimization 122

6.4 Experiments and evaluation 128

6.5 Why the flywheel can improve the power performance 134

7 Conclusions and future work 137

Bibliography 140

List of Figures

1.1 Difference phases in a typical human walking cycle. This figure is processed from video purchased from third party. 2

1.2 Angular motion, velocity, torque, and power in each segment in typical human walking. Modified based on [1] under Creative Commons Attribution License and with open access. 4

1.3 Energy harvesting backpack by Rome *et al.* [4] 5

1.4 Energy harvesting backpack model 5

1.5 Knee energy harvester that harvests energy uses minimum effort by Donelan *et al.* [3] 7

1.6 Passive device that reduce metabolic cost of human walking Sawicki *et al.* [2] 8

2.1 Typical rotational electromagnetic generator assemble. 14

2.2 Electrical modeling of the generator. 15

2.3 Modeling of rotational electromagnetic generator based energy-harvesting system under a base excitation with constant displacement amplitude. 17

2.4 The frequency response of rotational electromagnetic generator based energy-harvesting system with different mass ratio μ. Mechanical damping ratio is 0.25. 19

2.5 Design and working principle of the MMR based energy harvesting backpack. (a) 3D view of backpack overall design; (b) detailed view of MMR based transmission system; c) one-way bearing mechanism. . 21

2.6 MMR based energy harvesting system modeling (a) engaged (b) disengaged. Note that as the system engages and disengages, it becomes a nonlinear system. 23

2.7 Equivalent electrical circuit for MMR based energy harvester. 25

2.8 The frequency response of electric power output: non-MMR system vs. MMR system. All three cases have the same mechanical damping ratio 0.25. 26

2.9 Base excitation experiment setup. 28

2.10 (a) Time-domain fitting to obtain generator damping c_g. (b) Fitting in the frequency domain to obtain engaged mechanical damping c_m and friction F_r. Excitation is $180s$, $1.0 \sim 2.5Hz$ sweep sine, 15 mm base excitation. Frequency is normalized to $2Hz$. 29

2.11 Time domain of voltage output and power output comparison: MMR vs. non-MMR. The amplitude of base excitation is $20mm$. The frequency is $2Hz$ and it is the resonance frequency of the non-MMR system. The external resistor is 15 Ω. The average power output for the MMR based system is $1.64W$. For non-MMR, it is $1.69W$. The power output at primary frequency is approximately the same. 31

2.12 Power output frequency response: experiment vs. simulation. a) without flywheel, =1.6; b) with a small flywheel, =3.6; c) with a large flywheel, =5.3. Frequency is normalized to 2 Hz. Since non-MMR is a linear system and all the system parameters are known, the power output is simulated instead of experimentally measured. 32

2.13 The force from harvester to base: MMR vs. non-MMR. The force is normalized to rotational inertia equivalent gravitational force m_e g. MMR and non-MMR system have the same base excitation $Y = 0.025\sin(4\pi t)$. Both are tuned to optimal condition and have the same optimal power output. 34

2.14 The force from harvester to the base. Excitation is $2Hz$, $20mm$ sinusoidal base excitation. $\mu = 1.6$ and external resistance is 15Ω. The force is normalized to $m_e g$. 35

2.15 Time domain comparison of experiment result and modeling results. The experiment result matches well with the modeling result with acceptable error. 36

2.16 Frequency domain comparison of experiment result and modeling results. 36

2.17 Instant power of MMR and non-MMR backpack for each subject: (a) subject A and (b) subject B. Walking speed: 4.8 km/h 38

2.18 Treadmill based human walking backpack-energy-harvesting result on frequency domain. 38

2.19 Linear (non-MMR) / MMR energy harvesting system and their electric equivalent. a) Linear energy harvesting system; b) MMR based energy harvesting system; c) equivalent electric circuit for the linear (non-MMR) energy harvesting system; d) equivalent electric circuit for the MMR based energy harvesting system. 40

2.20 The equivalent electrical model of the MMR. Instead of being the capacitor in the LC circuit, the capacitor becomes a smoothing capacitor. 40

2.21 Velocity / Voltage profile for the resistor R for three cases $\mu = 0$,$0 < \mu < \infty$, and $= \infty$. 41

2.22 MMR based energy harvesting system power output for different μ values. 42

2.23 Average power output vs. mass ratio for MMR based energy harvesting system. 42

2.24 Modeling of rotational electromagnetic generator based vibration energy harvesting system with force excitation. 43

2.25 Modeling of MMR based vibration energy harvesting system under force excitation. 45

2.26 Power output from force excitation comparison, damping ratio is $\xi_m = 0.25$. 45

3.1 Typical SDOF base excitation energy harvesting system 52

3.2 (a) Power output vs. mechanical damping, where $\mu = 1$. (b) Power output vs. stroke limit, where $\kappa = A/Y$, $\mu = 1$, and $\xi_m = 0.1$. 54

3.3 Constant amplitude base excitation energy harvesting frequency response. a) power; b) stroke; c) power-to-stroke ratio. The result is plot with $\xi_m = 0.1$. 54

3.4 System configuration of inerter-based 2DOF energy harvesting. Spring k_2 is in series with the inerter and damping. 55

3.5 Example application of inerter-based 2DOF energy harvesting backpack. a) side view; b) back view; c) detail design. 56

3.6 Frequency response of (a) power, (b) stroke and (c) power-to-stroke ratio. The frequency response is plotted at $\alpha = 0.62$, $\beta = 2.42$. The mass ratio $\mu = 1$ and mechanical damping ratio $\xi_m = 0.1$. SDOF system has the same mechanical damping coefficient with inerter-based 2DOF system. 57

3.7 Experiment setup to validate the performance of inerter-based 2DOF system. 59

3.8 Experiment validation of inerter-based 2DOF system performance: a) power, b) stroke, c) power to stroke ratio. Details of the parameters are shown in *Table 3.1.* The SDOF system has the same topology with 2DOF system except for spring k_2. The mechanical damping coefficient of the SDOF system is the same as the 2DOF system. . . . 59

3.9 Force-displacement loop analysis of the inerter-based 2DOF system vs. the optimized SDOF system. The displacement and force are nondimensionalized to excitation amplitude Y and the human body gravitation force mg respectively. The parameter used for SDOF system and 2DOF system are the same as that used in *Figure 3.2 (b)* and *Figure 3.6* respectively 61

3.10 Optimal power that can be obtained from the inerter-based 2DOF system at the targeted frequency with different mechanical damping ratios ξ_m and mass ratios μ. The stroke limit is the same as the optimal SDOF system. The power output is normalized to the optimal power of the SDOF system. 62

3.11 a)Power output at the target frequency increases as the allowed stroke limit increases; b) optimal power at limited stroke obtained process. The mass ratio $\mu = 1$ and mechanical damping ratio $\xi_m = 0.1$. 63

3.12 Power frequency response of the system with different mass ratios μ. . 64

3.13 (a) Inerter-based 2DOF energy harvesting system; (b) conventional 2DOF energy harvesting system. 65

3.14 The conventional 2DOF System power-to-stroke ratio vs. tuning frequency ratio α and spring ratio β. a) conventional 2DOF system; b) inerter-based 2DOF system. All the parameters are the same as the system shown in *Figure 3.6.* 66

3.15 Comparison of the inerter-based 2DOF system and the conventional 2DOF system. 67

3.16 Difference comparison of the equation of motion for the conventional 2DOF system and the inerter-based 2DOF system. 68

4.1 a) Inerter-based 2DOF energy harvesting system modeling. Spring k_2 is in series with the transducer [6]. b) The physical inerter-based 2DOF system. 73

4.2 a) Power output, b) stroke frequency response of linear inerter-based system with different mass ratios μ. The power and stroke are nondimensionlized. γ is frequency ratio and $\gamma = \frac{\omega}{\omega_0}$, where ω is exciation angular velocity and ω_0 is typical human walking frequency. [6] . . . 73

4.3 a) Linear inerter-based SDOF system b) nonlinear inerter-based SDOF system and c) comparison the power output frequency response of linear and nonlinear inerter-based system. It is observed that nolinear inerter-based system's behavior with $\mu = 1.5$ is pretty close to a system with $\mu = 0$. [7] 74

4.4 MMR design and working principle. a) overall view; b) cross-section view of MMR c) working mechanism of one-way-bearing. 75

4.5 Lumped model of the nonlinear inerter-based 2DOF energy harvesting backpack. 76

4.6 Analogous electrical circuit to represent the mechanical modeling. . . 78

4.7 Time domain simulation result of input voltage $\dot{x}_r$ and output voltage $\dot{x}_e$ of the rectifier bridge in electric domain. This corresponds to the input velocity and output velocity of the MMR in mechanical domain. Simulation result is obtained with $\bar{k_1} = 0.66$, $\bar{k_2} = 2.3$, $\xi_m = 0.13$, $\xi_e = 0.63$, and $\gamma = 1$. 79

4.8 Search process of golden-section search method. The results are obtained with $\bar{k_1} = 0.7$, and $\bar{k_2} = 2.5$, $\xi_m = 0.13$, and $\gamma = 1$. 80

4.9 a) Power, b) stroke, and c) power-to-stroke ratio over different frequency ratio $\bar{k_1}$ and spring ratio $\bar{k_2}$. All values are normalized to the optimal performance of SDOF system. 81

4.10 Optimal power identification with stroke limit the same as the optimal SDOF system. 81

4.11 a) Power, b) stroke, and c) power-to-stroke ratio frequency response of the nonlinear inerter-based system compared with the linear inerter-based system and the optimal SDOF system. The system parameters are $\bar{k_1} = 0.66, \bar{k_2} = 2.3$ for both nonlinear and linear case. $\xi_e = 0.61$ for nonlinear inerter-based system and $\xi_e = 1.08$ for linear inerter-based system case. Both damping ratios are close to optimal value. 82

4.12 Experiment setup. 83

4.13 Experiment results of the nonlinear and linear inerter-based system vs. simulation results. a) power output; b) stroke. 85

4.14 Power trend with respect to electric damping ξ_e 86

4.15 Simulation results of nonlinear inerter-based 2DOF system. a) power, b) stroke, c) power-to-stroke ratio frequency response. "sd." denotes small electric damping case. The parameters for small damping nonlinear inerter-based system is $\bar{k_1} = 0.66, \bar{k_2} = 2.3, \xi_e = 0.26$. The nonlinear inerter-based 2DOF system has $\xi_e = 0.58$. The parameters for the other cases can be found in *Figure 4.11.* 86

4.16 Experiment validation for the small stroke case. 87

5.1 Inverted pendulum model of human walking. This figure is processed from video purchased from third party. 94

5.2 The full cycle of ankle angle α, velocity, and power during walking. Ankle angle α is defined as the angle between the shank and the foot. (Modified based on [1][8] under Creative Commons Attribution License and with open access.) 95

5.3 The full cycle of human walking. The energy-harvesting phase is in the terminal stance. This figure is processed from video purchased from third party. 96

5.4 The modeling for energy harvesting working mechanism. a) low leg position in the starting (P1) and end (P2) of the terminal stance. b) energy harvesting phase in gait cycle. The energy harvesting phase is between P1 and P2, which is corresponding to (A) and (B) in b) (b) is modified based on [1][8] under Creative Commons Attribution License and with open access.) 97

5.5 CAD model of the ankle energy harvester. a) Overall view; b) zoomed view of the generator c) backside view of the generator. The shoe model is created by Jason Lewis via GrabCad Community 98

5.6 a) The negative energy harvester prototype; b) The device worn by a user. 99

5.7 Modeling of the ankle energy harvester. 100

5.8 Ankle angle and torque profile. (The figure is modified based on [1] [8] under Creative Commons Attribution License and with open access.) 102

5.9 Treadmill experiment setup. The volunteer (M. L.) walks at 4.8 km/h with the harvester. 103

5.10 Experimental results. a) voltage output; b) power output. Treadmill test with a constant speed at 4.8 km/h (3 mph). The average power for one phase is 0.05 W. There is one generator on each leg and each generator has three phases. Two-legs combined result in total power output $0.3 \pm 0.05W$ 104

5.11 Energy harvesting period in a full gait cycle. The photos are from testing with the participant walking on a treadmill at $4.8km/h$ (3 mph). 104

5.12 Energy harvesting in complete gait cycle. 105

5.13 Energy harvesting vs gastrocnemius muscle activity in the time domain. a) harvester displacement (between the rod and the hollow rod); b) force on the harvester; c) EMG signal in lateral and medial gastrocnemius muscle. 106

5.14 Torque analysis on the ankle joint: the muscle torque and the harvester torque. 107

5.15 Ankle motion and corresponding torque produced from harvester. . . 108

5.16 Rubber band spring illustration. 112

6.1 Working principle of the energy harvesting tile: (a) step down; (b) free rotation. 116

6.2 CAD design of the energy harvesting tile: (a) 3D view; (b) top view. 117

6.3 Prototype of the energy harvesting tile (one module). 118

6.4 Typical vertical ground reaction force (VGRF) for one step during walking, speed walking and running [9]. 119

6.5 Modeling of the electrical generator. 120

6.6 Working principle of the energy harvesting tile. Phase I: the step down and Phase II: free rotation. 121

6.7 Parameter identification result: (a) Vertical Ground Reaction Force (VGRF) from experiments; (b) voltage output comparison. 122

6.8 Numerical simulation results of the energy harvesting tile: (a) top panel displacement; (b) generator rotational angular velocity; (c) power output. All system parameters are from the energy harvester prototype. 10 ω load resistor is used in the simulation. 124

6.9 Variations of the (a) top panel displacement; (b) generator rotational speed; (c) power output as the load resistance changes. 125

6.10 Harvested energy versus load resistance. 126

6.11 Comparison of force-displacement loop of the energy harvesting tile with different flywheel rotational inertia. 127

6.12 Experiment: upon stepping on the top panel, the prototype powers an Ozark Trail 500-Lumen Spotlight. 128

6.13 Test experiment setup. 129

6.14 Experimental results: (a) Force input measured from experiments, (b) top panel displacement, (c) voltage output and (d) power output. The load resistance is 10 ω and the subject tested has a body weight of 80 kg. 129

6.15 Energy harvesting performance with respect to the load resistance. The flywheel has 1.9 times the rotational inertia of the electric generator. 130

6.16 Force-displacement analysis: (a) time domain data of force and displacement of the system without flywheel; (b) time domain data of force and displacement of the system with flywheel (1.9 times of the generator rotational inertia); (c) time domain electric power output for the system without flywheel; (d) time domain electric power output for the system with flywheel; (e) force-displacement loop of the system without flywheel; (f) force-displacement loop of the system with flywheel. 132

6.17 Energy output comparison of system with and without flywheel in walking, fast walking and running conditions. 133

6.18 Modeling of the energy-harvesting paver (left) with its force input from foot. 133

List of Tables

2.1 Equivalent terms of electrical and mechanical domain 25

2.2 Comparison of Pvalue 27

2.3 System parameters 28

2.4 System damping and friction identified by curve fitting experimental data. 30

2.5 Comparison of P value 33

3.1 System parameters of validation experiment. 60

4.1 Analogous terms in mechanical domain and electrical domain. 77

4.2 Experiment parameters. (The quantity in the bracket is the theoretical optimal value.) 84

5.1 Power exchange in the ankle during walking. The negative energy is denoted as negative. [1] 94

5.2 Parameters of generator. 100

5.3 Weight constitution of the harvester. 100

5.4 Performance comparison between different biomechanical energy harvesting (EH) devices. 110

6.1 System parameters of the energy harvesting tile. 123

Nomenclature

α The tuning ratio, which is the resonance frequency ω over the target frequency ω_0. Or the ankle angle

$\bar{P}$ The nondimensionalized power harvested by the generator

Δh The height change of the center of mass

η_e The electrical efficiency

$\gamma = \frac{\omega}{\omega_0}$ The excitation frequency ratio, which is the excitation frequency ω over primary frequency ω_0

$\kappa = \frac{A}{Y}$ The stroke limit ratio

$\mu = \frac{m_e}{m}$ The mass ratio, inertia equivalent mass over suspended mass

Ω The angular rotation velocity of the generator rotor

ω The angular frequency of the excitation

ω_0 The primary excitation frequency, which is also the targe frequency

$\omega_1 = \sqrt{\frac{k_1}{m}}$ The natural frequency of the primary system

$\omega_n = \sqrt{\frac{k}{m+m_e}}$ The natural frequency of SDOF system

τ_e The torque produced by the generator damping

τ_i The torque by the generator rotor inertia

$\xi = \frac{c}{2m\omega_0}$ The normalized damping ratio

$\xi_e = \frac{c_e}{2m\omega_0}$ The electrical damping ratio

$\xi_m = \frac{c_m}{2m\omega_0}$ The mechanical damping ratio

$\xi_{combined} = \xi_m + \xi_e$ The combined frequency ratio

A The stroke limit

C The capacitance analogous to m

c The damping coefficient

C_e The capacitance analogous to m_e

c_e The electrical damping coefficient

c_g The damping coefficient of the generator at disengaged state

c_m The mechanical damping coefficient

$F = F_0 \sin \omega t$ The force excitation

F_e The equivalent force produced on the rack by the generator damping

F_g The total force on the rack produced by the generator rotor

F_i The equivalent force produced on the rack by the generator inertia

$f_k = \frac{\omega_n}{\omega_0}$ The tuning ratio of SDOF system, which is related to spring k

$f_{k1} = \frac{\omega_1}{\omega_0}$ The tuning ratio of 2DOF system, which is related to first spring k_1

$f_{k2} = \frac{k_2}{k_1}$ The spring ratio, which is related to the second spring k_2

i Current

j The imaginary part

J_e The rotational inertia of the generator rotor

k The spring stiffness of the SDOF system

k_1 The stiffness of the first spring in the 2DOF system

k_2 The stiffness of the second spring in the 2DOF system

k_e The generator speed constant

k_t The generator torque constant

$k_{rotation}$ The rotational spring stiffness provided by the rubber band

k_{rubber} The spring stiffness of the rubber band

L Mechanical domain: The length of the rubber band spring. Electrical domain: the inductance analogous to spring stiffness

m The suspended mass

n The gear ratio

P The power harvested by the generator

r The pinion radius

R_e The resistance analogous to electrical damping c_e

R_i The generator internal resistance

R_L The generator load resistance

R_m The resistance analogous to mechanical damping c_m

r_{back} The radius of the winding mechanism at the backside of the generator

r_{ratio} The linear motion to rotation motion ratio of linear to rotation motion device

t Time

t_0 The disengage time point

T_f The Coulomb damping torque by the generator

V The voltage in the analogous circuit, and analogous to velocity v. Or the voltage produced by the generator

$VGRF$ The vertical ground reaction force

W The work done

Y The displacement amplitude

$y = Ye^{j\omega t}$ The base displacement excitation

z The relative displacement between the base and the suspension mass

Publications by the author

1. Liu, M., Zuo, L., Jung, H., Sharma, Y. (2020, April). Electrical damping tuning for broad bandwidth and human comfort in backpack energy harvesting (Conference Presentation). In *Smart Structures and NDE for Industry 4.0, Smart Cities, and Energy Systems* (Vol. 11382, p. 113820A). International Society for Optics and Photonics.

2. Liu, M., Tai, W. C., Zuo, L. (2020). Enhancing the performance of backpack energy harvester using nonlinear inerter-based two degrees of freedom design. *Smart Materials and Structures*, 29(2), 025007.

3. Tai, W. C., Liu, M., Yuan, Y., Zuo, L. (2018). On improvement of the frequency bandwidth of nonlinear vibration energy harvesters using a mechanical motion rectifier. *Journal of Vibration and Acoustics*, 140(5).

4. Liu, M., Tai, W. C., Zuo, L. (2018, September). Enhanced Vibration Energy-Harvesting Using Inerter-Based Two-Degree-of-Freedom System. In *ASME 2018 Dynamic Systems and Control Conference*. American Society of Mechanical Engineers Digital Collection.

5. Yuan, Y., Liu, M., Tai, W. C., Zuo, L. (2018). Design and treadmill test of a broadband energy harvesting backpack with a mechanical motion rectifier. *Journal of Mechanical Design*, 140(8).

6. Liu, M., Tai, W. C., Zuo, L. (2018). Toward broadband vibration energy harvesting via mechanical motion-rectification induced inertia nonlinearity. *Smart Materials and Structures*, 27(7), 075022.

7. Mi, J., Xu, L., Zhu, Z., Liu, M., Zuo, L. (2018, April). Design, modeling and testing of a one-way energy harvesting backpack. In *Active and Passive Smart Structures and Integrated Systems XII* (Vol. 10595, p. 1059520). International Society for Optics and Photonics.

8. Liu, M., Lin, R., Zhou, S., Yu, Y., Ishida, A., McGrath, M., ... Zuo, L. (2018). Design, simulation and experiment of a novel high efficiency energy harvesting paver. *Applied energy*, 212, 966-975.

9. Liu, M., Tai, W. C., Zuo, L. (2018). Energy Harvesting From Ankle: Generating Electricity by Harvesting Negative Work. In *ASME 2018 Conference on Smart Materials, Adaptive Structures and Intelligent Systems*. American Society of Mechanical Engineers Digital Collection.

10. Yuan, Y., Liu, M., Tai, W. C., Zuo, L. (2017, April). Design and experimental studies of an energy harvesting backpack with mechanical motion rectification. In *Sensors and Smart Structures Technologies for Civil, Mechanical, and Aerospace Systems* 2017 (Vol. 10168, p. 1016825). International Society for Optics and Photonics.

11. Tai, W. C., Liu, M., Yuan, Y., Zuo, L. (2017). On improvement of operation bandwidth of duffing-like vibration-based harvesters using a mechanical motion rectifier. In *ASME 2017 International Design Engineering Technical Conferences and Computers and Information in Engineering Conference*. American Society of Mechanical Engineers Digital Collection.

12. Liu, M. (2016). Evaluation of a simple model for the acoustics of bat swarms (Master thesis, Virginia Tech).

13. Guo, S., Xu, L., Liu, Y., Liu, M., Guo, X., Zuo, L. (2016). Modeling, experiments, and parameter sensitivity analysis of hydraulic electromagnetic shock absorber. In *ASME 2016 International Design Engineering Technical Conferences and Computers and Information in Engineering Conference.* American Society of Mechanical Engineers Digital Collection.

Chapter 1

Introduction

1.1 Background

Energy harvesting can power distributed sensor nodes, recharge batteries, improve system efficiency, and even enable net zero systems [10]. Energy harvesting from the human body can power wearable and mobile systems and thus has the potential to reduce the dependence on batteries or even replace batteries [1]. The wearable and mobile devices can be smartphone, laptop, tablet, GPS, smartwatch, virtual reality device, smart clothes, torchlight, night-vision device *et al.* Almost all of those devices depend on batteries for power. Batteries have limited life span and need to be replaced or recharged frequenctly. This will get the wearer tethered to an energy source or having to carry a huge battery pack for a multi-day expedition. In this wireless era, the last thing that tethers human is the power supplement.

The amount of energy needed by those electronic devices is low to the milli-watt level and is continuing to decrease due to the development of electronics technology[11]. On the other hand, the energy stored in the human body is huge, roughly equal to 1000 kg of battery [12]. The human energy expenditure is on the scale of hundreds of watts [13], which is huge compared with the energy expenditure of wearable and mobile devices. The assumption here is that if only a very small amount of that power can be harvested, it would be enough to power wearable and mobile devices. What's more, by energy harvesting from the human body for electronic devices, the energy can be sourced locally and used locally. The above-mentioned facts combined make the energy harvesting from the human body very promising.

It is important to understand the human body before doing any energy harvesting. As if the energy harvesting poses a burden to the human body, it will not be welcomed and will be considered as an energy conversion device instead of energy harvesting device. One example is the hand cranked generator. More energy can be obtained as long as the generator is cranked. However, the time and effort that has to be put in to generate energy make it less than welcoming. Another drawback of the hand-crank generator is the energy harvesting process occupies the user. The user can not do other activities while harvesting energy, such as surfing the Internet or texting message. The goal of the energy harvesting devices developed in this dissertation is to

1. Do not require extra metabolic cost for energy harvesting;
2. Do not occupy the user while harvesting energy.

Looking into the human walking, we will find out that typically human consisted of repeated cycles and each cycle follows certain phases as illustrated in *Figure 1.1*.

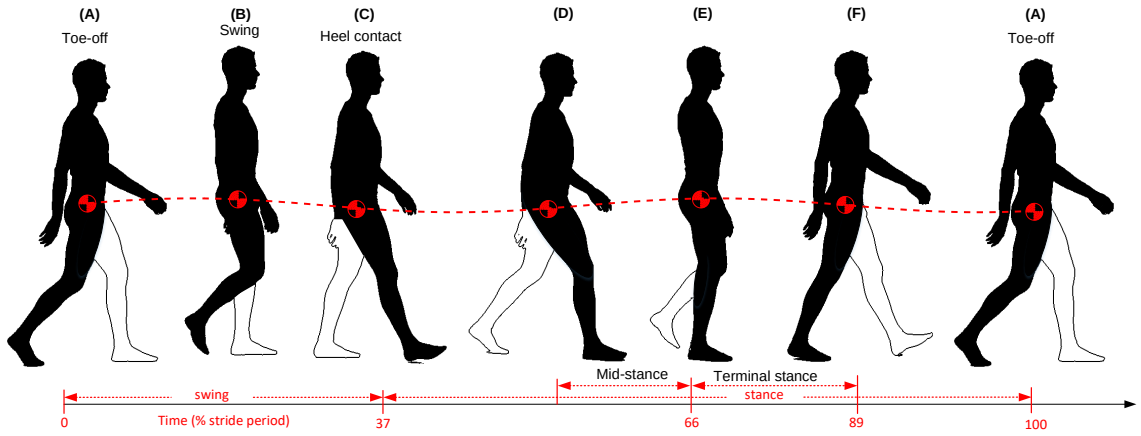


Figure 1.1: Difference phases in a typical human walking cycle. This figure is processed from video purchased from third party.

From *Figure 1.1*, the human walks in cycles, i.e. start with phase A and ends with phase A. We move around by repeating those cycles. Unlike the simple spring-mass model, where potential energy and kinetic energy are transformed back and forth in a cycle, human walking requires energy and the energy will not come back. Theoretically, constant speed human walking on level ground should not require power input, as the potential energy and kinetic energy at the end of the walking

cycle does not change compared with the start of the cycle. The energy dissipated in air drag and joint friction is neglectable compared with the energy required for walking [18]. The energy that was consumed in human walking, in this sense, is wasted. The positive work done by the muscles is almost all counteracted by the impact energy loss and negative muscle work. For every watt of positive work done by the muscles, the muscles will have to do 0.7 watts of negative work, and 0.3 watts of the power is dissipated by impact, and mostly in the heel contact [19]. One fact that needs to be noticed is that both positive muscle work and negative muscle work requires metabolic cost [20]. It would be a win-win situation if the negative muscle work can be harvested. Substantial energy can be harvested while the muscle that is supposed to do negative work can catch a rest. This is similar to the regenerative brake in vehicle systems.

By analyzing the energy flow in each phase, one will find not only positive muscle work but also negative muscle work is done in order to maintain normal human walking, as illustrated in *Figure 1.2*. As both positive muscle work and negative muscle work consume metabolic power, it is worthwhile to harvest negative muscle power while putting the corresponding muscles at rest. Harvesting negative muscle work can potentially decrease the human effort and decrease metabolic rate.

The human center of mass undergos a vertical motion due to the transition between the single stance and double stance phase. From the human model, the COM at single stance will be higher than the COM at double stance by 5 cm. It takes effort not only to move the COM up and but it also take energy to move it down. What's more, the conventional backpack moves up and down with the COM and more effort will be required. The energy harvesting backpack, as illustrated in *Figure 1.3* , is invented by Rome *et al.* [4]. It takes advantage of the COM motion and harvests 7.4 W of power while only a relative small metabolic rate increase was observed.

Among all the energy harvesting methods from the human body, such as thermal [14], piezoelectric [15], electromagnetic [4], triboelectric [16], electromagnetic energy harvesting is the most promising in terms of the amount of power harvested, efficiency, and power density [4][17]. Especially for rotational electromagnetic generator, the energy density can be increased by the using of gearbox and used extensively [17]. The electromagnetic generator is modeled as an inerter term m_e and a damping term c_e.

The energy harvesting backpack is modeled as a spring-mass-damper system with human torso motion as base excitation. As illustrated in *Figure 1.4*.

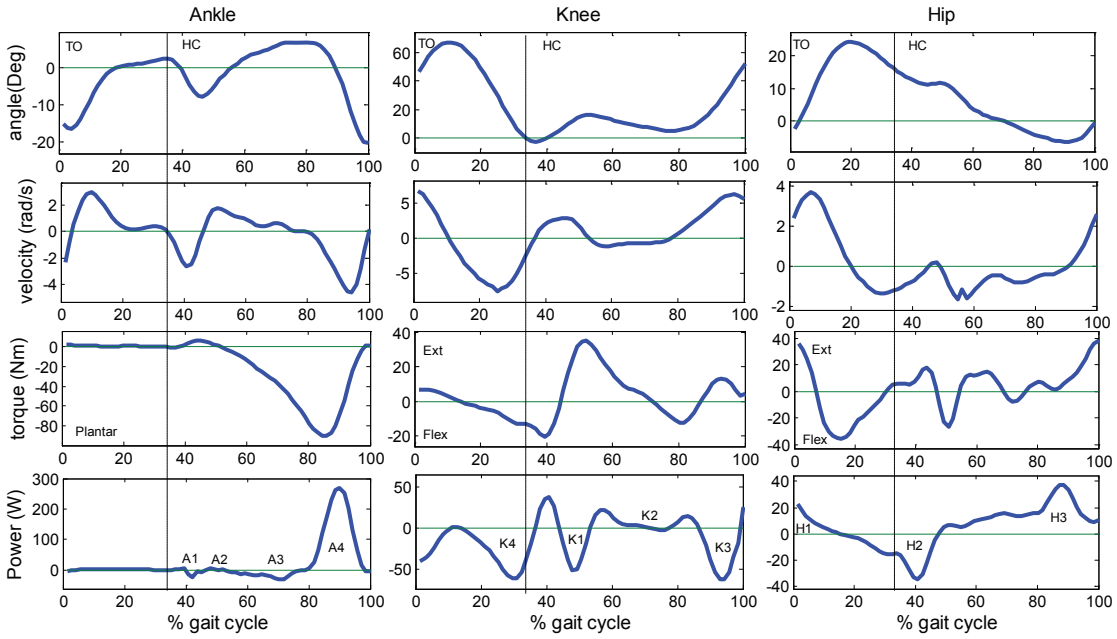


Figure 1.2: Angular motion, velocity, torque, and power in each segment in typical human walking. Modified based on [1] under Creative Commons Attribution License and with open access.

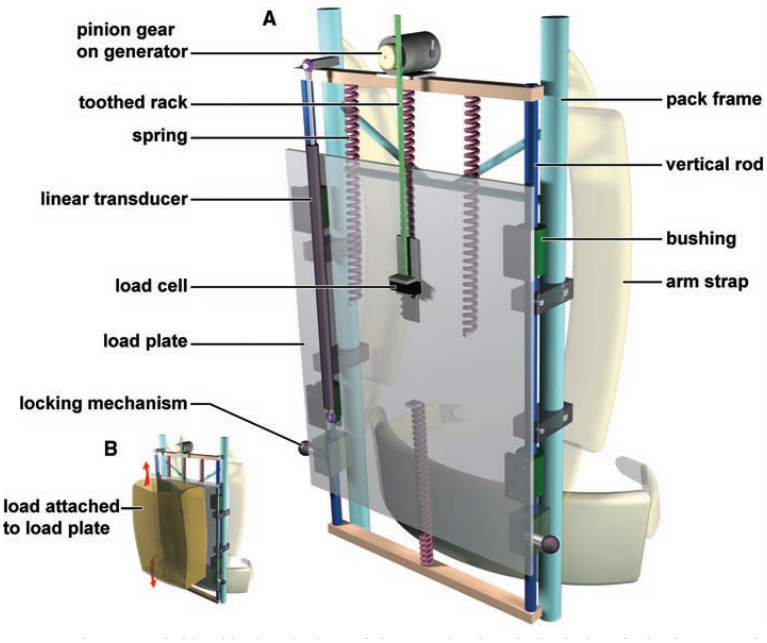


Figure 1.3: Energy harvesting backpack by Rome *et al.* [4]

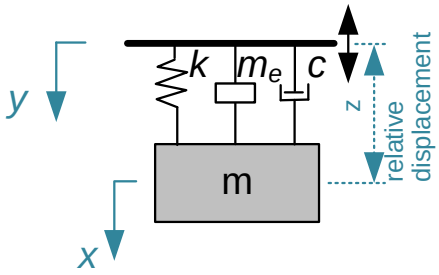


Figure 1.4: Energy harvesting backpack model

The equation of motion is

$$(m + m_e)\ddot{z} + (c_m + c_e)\dot{z} + kz = -m\ddot{y} \tag{1.1}$$

where m is the backpack mass, m_e is the equivalent mass of the generator rotor, c_m and c_e are mechanical damping and electrical damping respectively. k is the spring which hang the backpack mass. y is the torso movement in vertical direction, and z is the relative displacement between the backpack and the human body. Power output can be calculated from the equation of motion.

$$P = \frac{m^2\omega^6 Y^2}{2} \frac{c_e}{[k - (m + m_e)\omega^2]^2 + (c_m + c_e)^2\omega^2} \tag{1.2}$$

Through frequency matching and impedance matching [21], the maximum power can be obtained as

$$P = \frac{m^2\omega^6 Y^2}{16\xi_m} \tag{1.3}$$

where ξ_m is the mechanical damping ratio, and $\xi_m = \frac{c_m}{2m\omega_0}$. ω_0 is the primary frequency of human walking and equals to 2 Hz. The power performance is limited by this 1DOF system. Much work is done in *Chapter. 2*, *Chapter. 3*, *Chapter. 4* to improve the performance of the backpack.

From *Figure 1.2*, negative muscle work is done in phase A1, A2, A3, K1, K3, K4, and H2. Knee energy harvester [3] was invented to harvest the negative muscle work in K4, as illustrated in *Figure 1.5*. K1 and K3 are the knee power while landing and toe-off. There is negative muscle work in the hip in H2 but mounting harvester on the hip is challenging, considering the trunk shape and the small angular motion in the hip. The power in phase A1, A2 are too small to be collected.

At the same time, the center of mass (COM) moves up and down as the shift between single stance and double stance phase. The COM potential energy is proportional to the vertical position, i.e. height. The muscles are consuming metabolic energy to not only move the COM up but also move it down. Not only the positive work period but also the negative work period add metabolic cost to the human body. It would be beneficial if part of the negative work can be replaced with an energy harvesting device. In this way, power will be harvested while the metabolic rate is reduced. During the A3 phase, the COM moves down and the calf muscle does negative muscle work. Collins *et al.* [2] introduced a spring in parallel with the calf muscle to assist the calf muscle to do the negative work. The energy stored in the spring helps the calf muscle to do positive work in the toe-off phase. A 7.2%

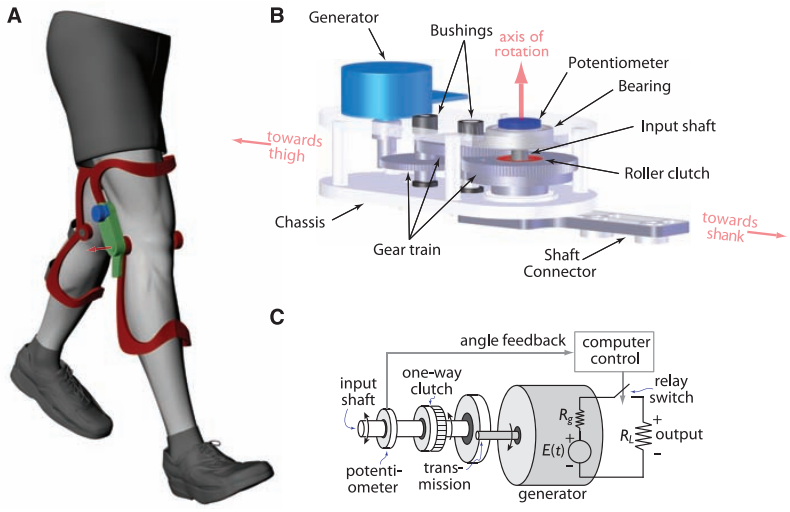


Figure 1.5: Knee energy harvester that harvests energy uses minimum effort by Donelan *et al.* [3]

decrease in metabolic rate is experienced compared with the normal human walking. In energy point of view, they harvested some energy in the form of spring potential energy. The energy is used right away in the toe-off phase. In *Chapter 5*, a negative muscle work device that only harvest negative calf muscle work is described in detail.

Different from harvesting negative muscle work, another way is to harvest impact energy. The most promising is the foot fall energy. Energy can be harvested by taking advantage of the relative displacement in the shoe, or in the paver. If the relative deflection is small enough, the influence on the human body is negligible. As the foot step force is large, substantial power can be harvested. In *Chapter 6*, an energy harvesting tile is described in detail.

1.2 Objective and contribution of this dissertation

The objective and contribution of this dissertation is as follows.

Objectives

1. Improve the performance of the current energy harvesting backpack in terms of power output, frequency bandwidth, stroke control. Figure out scientifically how

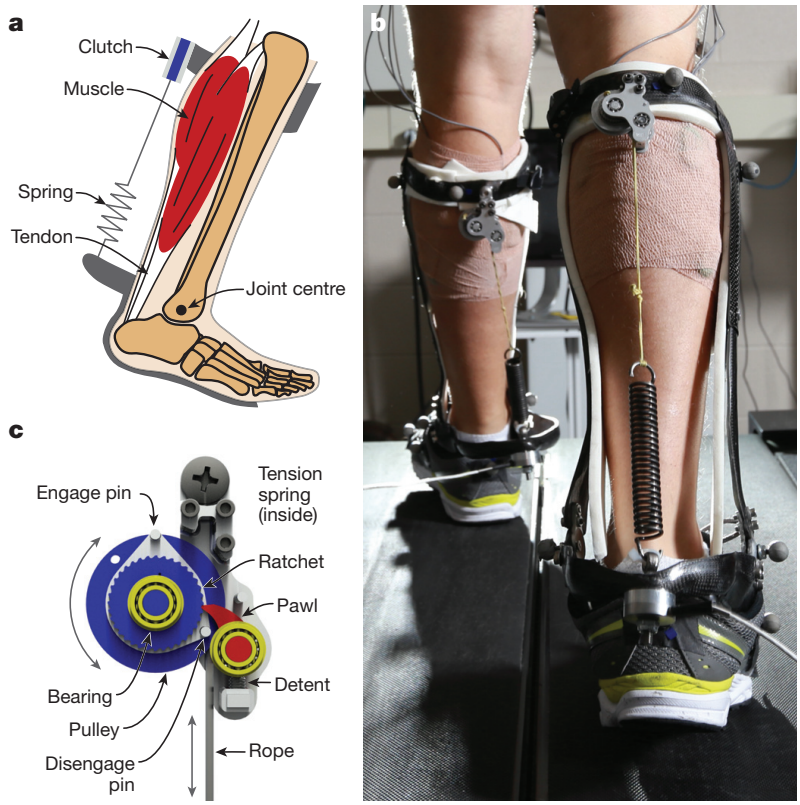


Figure 1.6: Passive device that reduce metabolic cost of human walking Sawicki *et al.* [2]

and why those methods can improve the performance.

2. Build an energy harvester that can harvest negative muscle work from human body. Come up with a clear model to guide the harvester design. Come up with a evaluation matrix for the harvester design. Explain the design concerns, and explain the mechanism behind the harvester design.

3. Build an energy harvester that can harvest impact energy from human walking. Come up with a clear model to guide the design. Explain the parameter choice and dig into the scientific contribution of the modeling.

Contributions

1. The inertia term m_e introduced by the electromagnetic generator makes the frequency bandwidth of the energy harvesting system narrow, as it sits in the denominator term of the power output (i.e. $P = (\frac{m^2\omega^6 Y^2)}{2}\frac{c_e}{([k-(m+m_e)\omega^2]^2+(c_m+c_e)^2\omega^2}$, m_e decreases P). The use of Mechanical Motion Rectifier (MMR) makes the generator rotates in one direction instead of rotating back-and-forth, thus decrease the inertia term and increase the frequency bandwidth.

2. Although the bandwidth is increased, the power optimization hit a limit since the parameter space is limited (as it is SDOF system and only has one-degree-of-freedom and one resonance). One more spring is added and by taking advantage of the inerter in the generator, a large equivalent mass can be achieved by using a small physical mass. In this way, one more degree of freedom is obtained, and thus having two resonance frequencies instead of one. Large power can be obtained by tuning the two resonance frequencies around the target frequency. This leads to more power output and thus the benefits of the 2DOF system are obtained without adding a large physical mass.

3. Although large power can be obtained by adding a spring, the peak stroke in the frequency domain is also relatively large. Large stroke is not good for energy harvesting backpack. By analyzing the parameters, we find out that the decrease of m_e will result in a much flat stroke response in the frequency domain. By adding MMR to the 2DOF system, the effect of m_e is decreased and the stroke response is frequency domain is much more flat. This result in a small peak stroke.

4. A harvester is designed to harvest negative work from human walking while does not impede normal human gait. This is the first harvester designed on the ankle to harvest negative work with experiment validation. Pilot experiments (with the hu-

man participant as the first author himself) show that the device harvests $0.3\pm0.05W$ of power and works at the muscle negative work phase, and is trying to assist the muscle. A model of the harvester is built to guide the harvester design.

5. Designed an energy harvesting tile/paver that can harvest the impact energy in human walking. The system harvests the most power while the effect on normal human walking is controlled. The modeling of the human foot and the harvester is built. The modeling points out how and why more power can be harvested by parameter tuning. The modeling is validated by experiment.

1.3 Dissertation organization

This dissertation is organized as follows. In *Chapter 2*, MMR based energy harvesting backpack is described in detail. Broader bandwidth is obtained compared with the system without MMR. In *Chapter 3*, a spring is added between the harvester and the base of the energy harvesting backpack. By taking advantage of the generator rotor inerter, two-degree-of-freedom system is constructed without adding any physical mass. After optimization, more power is harvested at a broader bandwidth. In *Chapter 4*, MMR is added to the 2DOF backpack such that enhanced performance is obtained. Peak stroke in the working frequency range is reduced compared with the inerter-based-2DOF system. The overall performance is much better than the SDOF backpack while the peak stroke is increased by a small percent. In *Chapter 5*, an energy harvester that only harvests negative muscle work from the human body is presented in detail. In *Chapter 6*, an energy harvesting tile/paver was introduced in detail. A flywheel is added to the generator to harvest more power. Modeling and optimization were done to take full advantage of the flywheel.

Chapter 2

Mechanical Motion Rectify based Energy Harvesting Backpack

2.1 Chapter introduction

Energy harvesting technologies have a wide range of applications, including powering distributed wireless sensors, recharging batteries, and powering embedded devices [10]. The energy sources can be light, heat, vibration, radiation, etc. Vibration energy is ubiquitous and can be found in both small and large scale. Therefore, vibration energy becomes a good source for energy harvesting [17]. Typical vibration energy-harvesting models can be found in [21] [22]. From analyzing the model, the optimal power output is obtained by the resonance frequency tuning and load matching method, where the undamped natural frequency and equivalent electrical damping of the system are tuned identical to the excitation frequency and mechanical damping respectively [21]. As most of the excitation in real applications have time-varying frequency, broad frequency bandwidth feature is important for energy harvesting systems [23] [24]. Take the energy harvesting backpack [4] as an example. The energy harvesting backpack is tuned to have optimal power output at a certain walking frequency or frequency range. However, human walking and running frequencies vary from $1.7Hz$ to $4.2Hz$ [25]. That means the walking and running frequencies can easily shift back and forth by 50% when the resonance frequency of the backpack is tuned at $2.8Hz$. The energy harvesting performance will suffer as the excitation frequency deviates from the resonance frequency [24]. Significant progress has been made in broadening frequency bandwidth by resonance frequency tuning

[26], mono-stable nonlinear systems [27] [28], bi-stable nonlinear systems [29], passive resonance frequency self-tuning [30], energy harvesting with piecewise linear spring [31], and energy harvesting arrays [32] [33]. The electromagnetic generator can be linear [34] and rotational [35] [36]. Compared with the rotational generator, linear generator has a low specific power, which makes it large in both size and weight to achieve desired specific power [34]. On the other hand, with the help of gearbox, the rotational generator can achieve high specific power with a relatively small size [37]. However, the gearbox will not only increase the specific power, but also the rotational inertia of the generator rotor. In this regard, the generator rotor is considered as an inerter and its equivalent mass is proportional to the square of the gear ratio [38], which is also known as inertance. An inerter is a two-terminal device in which the forces applied at the terminals are equal, opposite, and proportional to a relative acceleration between the nodes [38]. As a result, the inerter cannot be neglected in many large-scale energy-harvesting systems [39] [40] [41] [42]. With all the efforts the researchers have done to increase the frequency bandwidth, however, we found out that the frequency bandwidth becomes narrow as the inertance increases. In this way, the use of gearbox causes a trade-off between power density and bandwidth. In many situations, the gearbox has to be used due to design considerations, such as size limitation and power output requirement [43]. It is critical to find a way to increase the bandwidth of the rotational electromagnetic generator based energy harvesting system. In striving for increasing bandwidth of energy harvesting system, most researchers consider only spring nonlinearity [29] [26] [27] [28] [30] [31] [32] [33]. Few researchers consider the nonlinearity of mass, and the influence of mass nonlinearity on energy harvesting performance is unclear. In the literature, a type of mass nonlinearity can be achieved by means of Mechanical Motion Rectification (MMR). MMR is a mechanical transmission concept proposed for energy harvesting systems by Zuo *et al.* [44] and Pourghodrat [45]. By using two sets of opposing one-way clutches embedded bearings, MMR can transmit bidirectional oscillations into unidirectional rotation of the generator. Furthermore, due to engagement and disengagement between the shaft and one-way bearings, the inertia of the system alternatively becomes large and small, resulting in piecewise linear inertia. With the inertia nonlinearity, MMR based systems can have broadband energy harvesting performance [41] [46]. With MMR integrated into an energy-harvesting pendulum, for example, the bandwidth is larger than that of the counterpart without MMR, and the output power at high frequencies is much higher [41]. In ocean wave energy harvesting, MMR based systems harvest more power compared with systems without MMR under the same excitation [46]. In addition to broad bandwidth, MMR is able to improve both the ride comfort and road handling in vehicle shock absorber

designs [47]. With the potential to increase the bandwidth of energy harvesting systems, however, the role of MMR in vibration energy harvesting systems has not been systematically investigated. To find out the influence of the inerter on energy harvesting performance, a single-degree-freedom base excited model is considered. The influence of the inerter on energy harvesting is analyzed. MMR is considered in this paper to increase the bandwidth of rotational electromagnetic generator based energy harvesting systems. An MMR based energy harvesting system model is built. The influence of MMR on energy performance is simulated and compared with the counterpart without MMR (referred to as non-MMR system hereinafter. It is the conventional linear energy harvesting system.). Broad bandwidth of the MMR based energy harvester is presented with simulation and verified with experiments. It turns out that by adding MMR to the energy harvesting system, the influence of the inerter on bandwidth is reduced. In the MMR based system, the frequency response bandwidth of the system is much broader than the counterpart without MMR. For the same base excitation, MMR based system and non-MMR based system can obtain the same optimal power output at a primary excitation frequency. However, in the MMR based system, the force transmitted from the harvester is decreased compared to the non-MMR based system. For the MMR system with constant force amplitude, the bandwidth is much broader compared with the counterpart without MMR. The rest of this paper is organized as follows. In Sec. 2, the rotational electromagnetic generator-based energy harvesting system model will be built. Base excitation with constant displacement amplitude will be considered first. The influence of rotational inertia on energy harvesting performance will be discussed. The working principle, design, and modeling of the MMR based energy harvesting system will be described in Sec 3. To facilitate simulation, the system will be converted into the electrical domain by the analog of components and will be subsequently modeled using equivalent electric circuits. In Sec. 4, the simulation will be conducted based on the equivalent circuit model. The broadband feature of the MMR based energy harvester will be discussed. In Sec. 5, the experimental setup will be described and the experiment test results will be presented. The broadband feature will be validated. The simulation results will also show that the force transmitted to the base decreases after MMR is added. The simulation results will be verified by experiments. Force excitation with constant force amplitude will be discussed and a comparison will be made between the MMR and non-MMR system in Sec. 6. Finally, this work will be concluded in Sec. 7.

2.2 Influence of inerter on energy harvesting performance

Rotational electromagnetic generators are widely used in large-scale energy harvesting systems [17]. In this paper, the electromagnetic generator is modeled as a damping term in conventional vibration energy-harvesting systems [21] [22]. The generator rotor is considered as an inerter which is a two-node device that generates a resistant force proportional to the relative acceleration between the nodes and the proportionality is known as inertance. The inerter cannot be neglected in many occasions [36]. The modeling of the generator is introduced in the following part. A typical rotational electromagnetic generator based harvester assembly is shown in *Figure 2.1*, where linear motion is transmitted to rotational motion (by rack-pinion, ball screw, etc.). This motion is then magnified by a gearbox and transmitted to the generator. The generator is typically mounted on the base and rack is connected to a suspended mass. As there is rotational inertia torque and electromagnetic torque from the generator, the force F_g on the harvester consists of both inertia force and electromagnetic force.

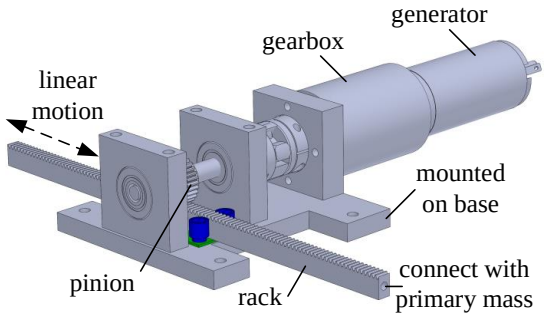


Figure 2.1: Typical rotational electromagnetic generator assemble.

The rotational inertia torque τ_i produced by the generator is

$$\tau_i = J_g \Omega \tag{2.1}$$

where J_g is the rotational inertia of the generator rotor; Ω is the angular rotational velocity of the generator and $\dot{\Omega}$ is the angular rotational acceleration. The rotational torque is amplified by the gearbox and then transferred to linear force by rack-and-pinion. Considering the pinion gear radius r and gearbox gear ratio n, the inertia

force F_i transmitted to the rack is

$$F_i = \frac{n}{r\tau_i} = \frac{n^2}{r^2 J_g z} \tag{2.2}$$

where z is the linear displacement of the rack, and $\dot{z} = \frac{n}{r}\omega$. The equivalent linear mechanical inertia m_e of the inerter is

$$m_e = \frac{n^2}{r^2 J_g} \tag{2.3}$$

On the electrical side, the direct current (DC) generator can be modeled as a voltage source with internal and external resistance. The lumped model is shown in *Figure 2.2.*

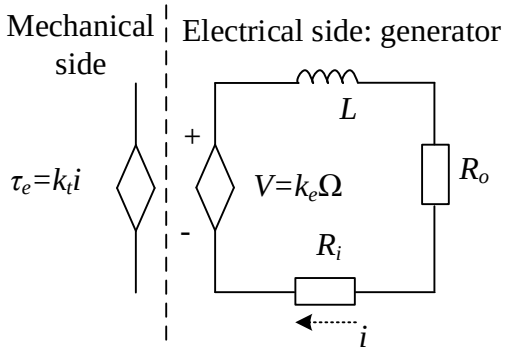


Figure 2.2: Electrical modeling of the generator.

Voltage V produced by the generator is

$$V = k_e \Omega \tag{2.4}$$

where k_e is the speed constant of the generator. Usually, the inductance of the generator is small and can be neglected. According to Kirchhoff's voltage law,

$$i = \frac{k_e \Omega}{R_i + R_L} \tag{2.5}$$

where R_i,R_L are internal electrical resistance and external electrical resistance respectively. The electromagnetic torque τ_e produced by the generator is then related to the rotational speed as

$$\tau_e = k_t i = \frac{k_t k_e}{(R_i + R_L)\omega} \tag{2.6}$$

where k_t is the torque constant of the generator. After transmission by the gearbox, the electromagnetic force F_e produced by the generator, and transmitted to the rack is

$$F_e = \frac{\tau_g n}{r} = \frac{k_t k_e n^2}{(R_i + R_L)r^2} z \tag{2.7}$$

In this way, the force produced by the generator is proportional to the velocity of the rack. The generator can be modeled as a viscous damping term with damping coefficient defined as

$$c_e = \frac{k_t k_e n^2}{(R_i + R_L)r^2} \tag{2.8}$$

Considering both inertia force and electromagnetic force of the generator, all the force produced by the generator F_g is

$$F_g = F_i + F_e = m_e \ddot{z} + c_e \dot{z} \tag{2.9}$$

This part of force is transmitted from the generator to the suspended mass via the rack. Rotational electromagnetic generator-based energy harvesting system under excitation with constant displacement amplitude Vibration excitation from the environments can be in many forms. In this section, base excitation with constant displacement amplitude is considered. The lumped model is shown in *Figure 2.3*.

The system equation of motion is derived by Newton's 2nd law and shown as follows

$$(m + m_e)\ddot{z} + (c_m + c_e)\dot{z} + kz = -my \tag{2.10}$$

where m and m_e are the suspended mass and equivalent mass of the inerter respectively. z is the relative displacement between the base and the suspended mass. c_m is the mechanical damping. c_e is the equivalent electrical damping. k is the stiffness of the spring. Base excitation input is defined as $y = Y sin(\omega t)$, where Y is the

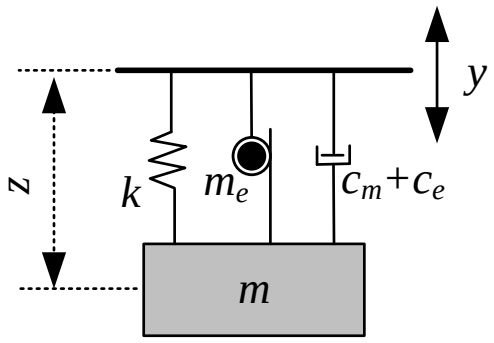


Figure 2.3: Modeling of rotational electromagnetic generator based energy-harvesting system under a base excitation with constant displacement amplitude.

amplitude and considered as constant. ω is the angular frequency of the excitation. The solution of *Eq. 2.10* leads to the relative displacement as

$$z = \frac{m\omega^2}{k - (m + m_e)\omega^2 + j\omega(c_m + c_e)} y \tag{2.11}$$

The average electrical power output is then found as

$$P = \frac{1}{2} c_e \dot{z}^2 = \frac{1}{2} c_e \frac{m^2\omega^6 Y^2}{[k - (m + m_e)\omega^2]^2 + (c_m + c_e)^2\omega^2} \tag{2.12}$$

In many energy situations, the excitation has a primary frequency, such as human walking [48] and car vibration [49]. In order to harvest a maximum energy, the resonance frequency of the vibration system should be tuned to match the primary frequency. The primary frequency of excitation is denoted as ω_0. The nondimensionalized form of the electrical power output is

$$P = \frac{P}{m\omega_0^3 Y^2} = \frac{\xi_e \gamma^6}{(1 + \mu)^2(\alpha^2 - \gamma^2)^2 + 4(\xi_m + \xi_e)^2\gamma^2} \tag{2.13}$$

where ω_n is the undamped natural frequency and $\omega_n = \sqrt{\frac{k}{m+m_e}}$, $\xi = \frac{c}{2m\omega_0}$, ω_0 is the primary frequency of the excitation, ω is excitation frequency, excitation frequency ratio $\gamma = \frac{\omega}{\omega_0}$, spring ratio $\alpha = \frac{\omega_n}{\omega_0}$, and $\mu = \frac{m_e}{m}$ is mass ratio. Intuitively speaking,

the system should be tuned to perform best at the primary frequency, i.e. $\gamma = \frac{\omega}{\omega_0} = 1$. The power output is

$$P(\gamma = 1) = \frac{\xi_e}{((1+\mu)^2(1-\alpha^2)^2 + 4(\xi_m + \xi_e)^2} \tag{2.14}$$

Optimal power output is obtained by varying the frequency ratio α and equivalent electrical damping ratio ξ_e. Mathematically speaking, the necessary condition for a local extremum of *Eq. 2.14* is

$$\frac{\partial P_{\gamma=1}}{\partial \alpha} = \frac{\partial P_{\gamma=1}}{\partial \xi_e} = 0 \tag{2.15}$$

The solution of *Eq. 2.15* leads to the optimal parameters α^{opt} and ξ_e^{opt}

$$\begin{cases} \alpha^{opt} = 1 \\ \xi_e^{opt} = \xi_m \end{cases} \tag{2.16}$$

After plugging α^{opt} and ξ_e^{opt} into *Eq. 2.14*, the optimal average power output at primary frequency is obtained as

$$P^{opt}(\gamma = 1) = \frac{1}{16\xi_m} \tag{2.17}$$

From *Eq. 2.17*, the optimal power output at the primary frequency has nothing to do with the quantity of inerter mass m_e. With the optimal power parameters α^{opt} and ξ_e^{opt} plugged into *Eq. 2.13*, the frequency response of power output is

$$P^{opt}(\gamma) = \frac{\xi_m \gamma^6}{(1+\mu)^2(1-\gamma^2)^2 + 16\xi_m^2\gamma^2} \tag{2.18}$$

Eq. 2.18 indicates that when the excitation frequency is equal to the undamped natural frequency, i.e. $\gamma = 1$, the power output has nothing to do with the mass ratio μ. However, as the excitation frequency ratio increases or decreases, the power output changes. Let us define

$$q(\mu) = (1+\mu)^2(1-\gamma^2)^2 \tag{2.19}$$

After taking the partial derivative of *Eq. 2.19* with respect to μ, it can be shown as

$$\frac{\partial q(\mu)}{\partial \mu} = 2(1+\mu)(1-\gamma^2)^2 > 0 \tag{2.20}$$

At the undamped natural frequency $\gamma = 1$, $q(\mu) = 0$. However, at any point $\gamma > 1$ or $\gamma < 1$, $q(\mu)$ will increase as the increase of μ, indicated by *Eq. 2.20*. This indicates that as μ increases, the power output *Eq. 2.18* at $\gamma > 1$ and $\gamma < 1$ will decrease because *Eq. 2.19* is at the denominator. This leads to a decrease of bandwidth. In conclusion, the increase of the equivalent rotational mass m_e will result in a narrow bandwidth. The mass ratio in literature [41] was found to be 0.82. The energy harvesting backpack prototype built (shown in *Figure 2.5*) has a mass ratio of 1.6. By adding a flywheel, the mass ratio becomes 3.6. Frequency response can be obtained by plotting $\bar{P}^{opt}(\gamma)$ in Eq. (13) over frequency ratio γ. Here all three mass ratio cases ($\mu = 0.82, 1.6, 3.6$) are considered. A reasonable damping ratio of 0.25 is considered. The power frequency response is shown in *Figure 2.4*.

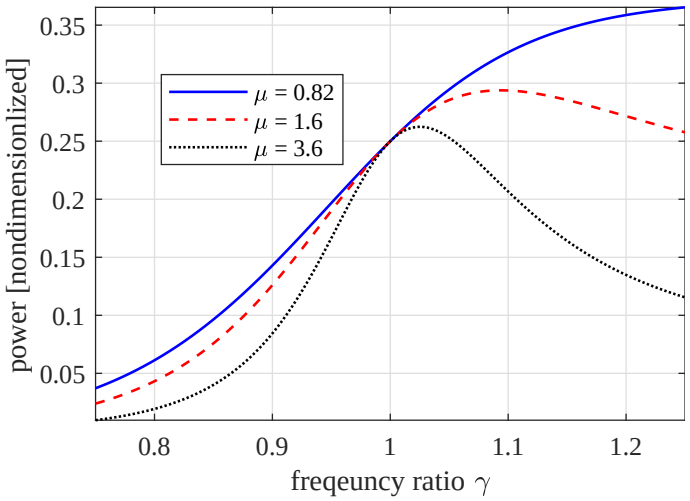


Figure 2.4: The frequency response of rotational electromagnetic generator based energy-harvesting system with different mass ratio μ. Mechanical damping ratio is 0.25.

Typically, the bandwidth of interest is defined as the frequency difference between the two half-power points [50]. However, using the half-power bandwidth as a criterion to measure harvester performance can be misleading [51]. The power output in base-excited system with a large damping will not drop below the half-power as the

driving frequency increases when $\xi_{combined} > 0.147$, where $\xi_{combined} = \xi_m + \xi_e$. The proof can be found in the Appendix. This phenomenon is illustrated by the $\mu = 0.82$ case in *Figure 2.4*. There is no half-power bandwidth in such case. To describe the bandwidth in such situation, we look into the average power within an arbitrary frequency range of interest $(1-\alpha, 1+\alpha)$.

$$P(\mu, \xi_m) = \int_{1-\alpha}^{1+\alpha} \frac{\overline{P}(\gamma)}{2\alpha} d\gamma \tag{2.21}$$

where α is the frequency range of interest, which can be defined by the intended frequency range the harvester is aimed for. In our case, $\alpha = 0.25$ is selected, to consider frequency range of [0.75,1.25]. From this definition, $\bar{P}$ of three different mass ratio cases shown in *Figure 2.4*, i.e. μ=0.82, 1.6, 3.6, are 0.23, 0.2, and 0.14 respectively. In this sense, the bandwidth decreases as the increase of μ. As shown in *Figure 2.4*, with the same damping ratio ξ_m, the system with different inerter mass has the same optimal power output at the undamped natural frequency (when $\gamma = 1$). However, the bandwidth decreases as the increase of inerter mass m_e. Generator research and industry have tried the best to increase the power density and decrease the inerter [43]. However, due to material and manufacture limit, the generator rotational inertia cannot be eliminated. In other words, the analysis presented in this section is important when designing the generator.

2.3 Concept, design, and modeling of MMR based energy harvester

2.3.1 Concept and design

To increase the bandwidth of the rotational electromagnetic generator-based system, MMR is considered. The MMR based energy harvester can be applied in many different application scenarios. Here we take the energy harvesting backpack as an example. Human walking results in a 4∼7 cm vertical center of mass motion [52]. In the traditional backpack design, energy is wasted by making the backpack oscillating up-and-down with the human body. To harvest this kinetic energy from human walking, Rome *et al.* proposed the first suspended load energy harvesting backpack [4]. The backpack is hanged on a frame, and the frame is attached to the human torso. The motion of the backpack is guided by two linear guides on the

frame, so its movement is strictly up and down motion relative to the frame. A rack-pinion mechanism transforms the up and down motion to rotational motion. The pinion gear is fixed to the frame while the rack is fixed to the backpack load. The relative movement between the backpack and the frame drives the pinion gear to rotate. The rotational motion drives the generator, and the energy is harvested. To facilitate energy harvesting performance, MMR is introduced to transmit the relative motion between the human body and backpack to unidirectional motion to the generator. The detailed working principle of MMR can be found in [46]. The MMR based energy harvester design is shown in *Figure 2.5*.

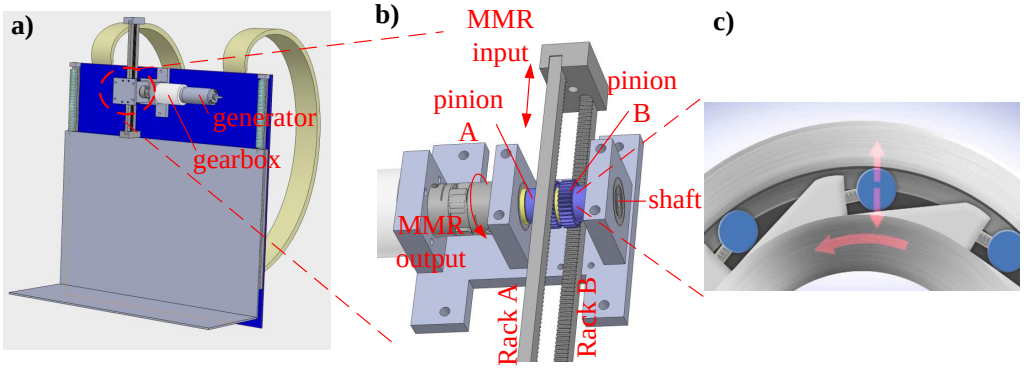


Figure 2.5: Design and working principle of the MMR based energy harvesting backpack. (a) 3D view of backpack overall design; (b) detailed view of MMR based transmission system; c) one-way bearing mechanism.

As shown in *Figure 2.5 (b)*, there is a one-way bearing between the pinion gear and the shaft. When the rotational velocity of the outer ring of the one-way bearing in *Figure 2.5(c)* cannot catch up with the velocity of the inner ring, the one-way bearing will engage the shaft. The one-way bearings in the two pinion gears are designed to have engagement in opposite directions: gear A will engage the shaft in a counter-clockwise rotation, and gear B will engage the shaft in a clockwise rotation. When the rack moves down relative to the harvester, pinion gear A engages the shaft, and pinion gear B does not, thus driving the shaft to rotate counter-clockwise. When the rack moves up relative to the harvest, pinion gear B will engage and pinion gear A will not engage. In this way, the racks drive the shaft to rotate counter-clockwise too. Moreover, when the generator rotation velocity is high, both pinions gears will disengage. In this way, the up-and-down motion decouples with the rotational

motion. Therefore, with this design, no matter the backpack oscillates up or down, the generator will always rotate in one direction. When the rack movement cannot follow the rotation of the generator, both gears will disengage, and the generator will continue to rotate due to the remaining kinetic energy. As the generator is a DC generator, power is continuously harvested and the voltage is always positive. To improve the power density, a gearbox is added to transfer and magnify the velocity of rotation motion.

2.3.2 System modeling

Human walking results in a 4 7 cm vertical center of human body motion [52] and can be treated as a base excitation to the energy harvesting backpack. The energy harvesting backpack is modeled as a spring-mass-damper system. When the MMR disengages, the generator rotor is not coupled with the backpack vibration. The backpack vibration system is referred to as the primary system and the decoupled generator is referred to as a secondary system. As the system switches from engaged and disengaged state, the system damping is more complicated than the non-MMR based system. To model the system with high fidelity, the friction of the backpack frame F_r, damping of the engaged system c_m, damping of the frame c_f, damping of the disengaged generator c_g, and electrical damping c_e are modeled and identified respectively. Frame friction is always in the primary system. When the system engages, frame damping c_f, engaged mechanical damping c_m, electric damping c_e and rotational equivalent inertia m_e are in the oscillation system (as shown in *Figure 2.6 (a)*). c_m comes from the rack-pinion, gearbox, and the generator. When the system disengages, the generator is not in the primary vibration system anymore. This leaves the primary system only with backpack load m, spring k, frame friction F_r and frame damping c_f. The generator rotational equivalent mass m_e is then disengaged. In the generator, rotational inertia equivalent mass m_e forms a first-order system together with mechanical damping from generator c_g and electrical damping c_e. The overall lumped backpack system modeling is shown in *Figure 2.6*.

The equation of motion is derived by Newton's 2nd law and shown as follows.

$$\begin{cases} (m+m_e)\ddot{z} + (c_m + c_e + c_f)\dot{z} + kz + F_r sgn(\dot{z}) = -m\ddot{y} & engaged \\ m\ddot{z} + c_f\dot{z} + kz + F_r sgn(\dot{z}) = -m\ddot{y} & disengaged \end{cases} \tag{2.22}$$

where the base is the human body and its position is denoted as y. When the MMR

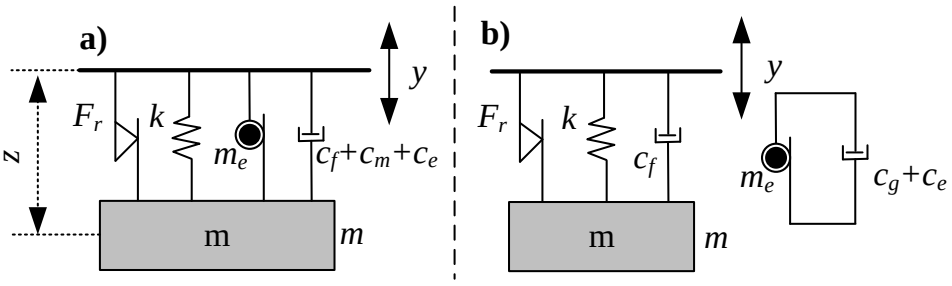


Figure 2.6: MMR based energy harvesting system modeling (a) engaged (b) disengaged. Note that as the system engages and disengages, it becomes a nonlinear system.

engages, the rotational velocity of the generator ω is proportional to the relative velocity between the frame and the human body $\dot{z}$. The engagement and disengagement make the system nonlinear. The system described in *Eq. 2.22* is denoted the full model. When the MMR disengages, there is only equivalent inertia mass m_e, mechanical damping from generator c_g, and electrical damping c_e in the generator. In this way, the generator follows an exponential decay until its velocity is small enough to be caught by the relative velocity of between the base and suspended mass again. The equation of motion of the generator during the disengaged state is

$$m_e\dot{\omega} = (c_g + c_e)\omega \tag{2.23}$$

In conclusion, the rotational velocity of the generator rotor is

$$\begin{cases} \Omega = \frac{n\dot{z}}{r} & engaged \\ \Omega = \Omega_0 e^{-\frac{t-t_0}{\tau}} & disengaged \end{cases} \tag{2.24}$$

Ω_0 and t_0 are the rotational velocity and time when the MMR system disengages. τ is the time constant of the generator motor exponential decay rate, which is defined as

$$\tau = \frac{m_e}{c_g + c_e} \tag{2.25}$$

The threshold for engagement and disengagement is

$$\begin{cases} engagement: & \dot{z} > \frac{\omega_0 r}{n} e^{-\frac{t-t_0}{\tau}} \\ disengagement: & \dot{z} < \frac{\omega_0 r}{n} e^{-\frac{t-t_0}{\tau}} \end{cases} \tag{2.26}$$

2.3.3 Equivalent Electrical Model

Since the MMR based energy harvesting system is nonlinear, closed-form solutions cannot be obtained. Numerical simulation is needed to find out the response to excitation. To facilitate simulation, the system is converted into the electrical domain and modeled by using equivalent electric circuits. The one-way bearing can be modeled as a diodes so that engagement and disengagement can subsequently be modeled as on and off state of the diodes, respectively. The equivalent electrical model can be found in [40] [37]. In their models, velocity in the mechanical domain corresponds to current in the electrical domain. Engage and disengage threshold of the one-way bearing is determined by velocity in the mechanical domain, so on and off state of the diode is determined by the current in the electrical domain. However, in the physical electrical system, on and off states of the diode is determined by voltage. The electric models in [40] [37] cannot match the mechanical model perfectly. The engage and disengage process cannot be explained. The problem emerges because Kirchhoff's voltage law is used to model the electrical system. In this paper, Kirchhoff's current law is used to match the mechanical domain to the electrical domain. With Kirchhoff's current law, all the components and engage-disengage states in the mechanical domain can match the electrical domain correspondingly. The equivalent terms and equation of motion in the engaged state are shown as follow.

$$\begin{cases} (m+m_e)\dot{v} + (c_m + c_e)v + k\int v = -m\ddot{y} & mechanical \\ (C+C_e)\dot{V} + \frac{V}{R+R_e} + \frac{1}{L}\int V = i & electrical \end{cases} \tag{2.27}$$

where C and C_e are capacitance, analogous to m and m_e respectively. R_m and R_e are electrical resistance, analogous to c_m and c_e respectively. L is inductance, alaog to spring stiffness k. V is voltage, analogous to relative velocity v between the base and the suspended mass. i is current, analogous to force. The equivalent terms match are shown in Table 4.1.

The input in the mechanical domain is force $-m\ddot{y}$, so the equivalent electrical component is current source i. As force in the mechanical domain corresponds to current

electrical domain		mechanical domain	
C,C_e	Capacitor	Mass	m,m_e
$\frac{1}{R+R_e}$	Resistance	Damping	$c_m + c_e$
$\frac{1}{L}$	Inductor	Spring	k
V	Voltage	Velocity	v
i	Current	Force	F

Table 2.1: Equivalent terms of electrical and mechanical domain

in the electrical domain, friction in mechanical domain can be modeled by a current source that is controlled by voltage (which corresponds to velocity in the mechanical domain). The equivalent circuit for the MMR based dynamic system corresponding to *Figure 2.6* is shown in *Figure 2.7 (a)*.

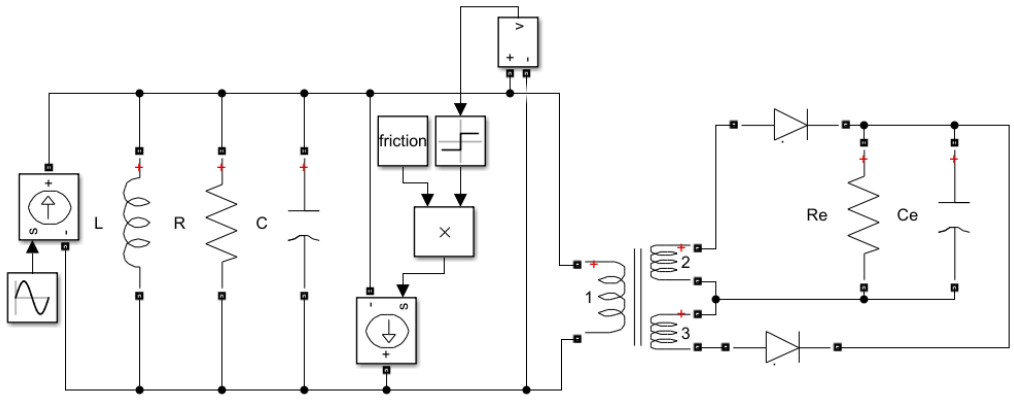


Figure 2.7: Equivalent electrical circuit for MMR based energy harvester.

With the equivalent electrical model, the performance of MMR based energy harvester can be simulated with commercially available software, such as Simulink.

2.4 Simulation the influence of MMR on energy harvesting

Numerical simulation is based on the model shown in *Figure 2.6*. The full model is complicated because it considers a specific system. To gain insight into the MMR

based system, the model is simplified in this section. Friction is not considered, and the engaged damping is $c_m + c_e$. When the system disengages, damping on the primary system is c_m, and damping on the generator is c_e. This model is referred to as the simplified model. As introduced in *Eq. 2.15*, the optimal spring stiffness k and electrical damping coefficient c_e in the non-MMR system can be obtained in closed-form. To find out the optimal parameters of the MMR based system, simulation is done by varying spring stiffness k. The optimal power is obtained and the corresponding parameters are obtained in this way. It turns out that with base excitation $y = Ysin(\omega_0 t)$ of fixed displacement amplitude, the optimal power obtained by the MMR based system is the same as the non-MMR based system. To characterize the performance of the MMR based energy harvesting system, frequency response of the power output of the system with and without MMR was computed by numerical simulation. The result is shown in *Figure 2.8*.

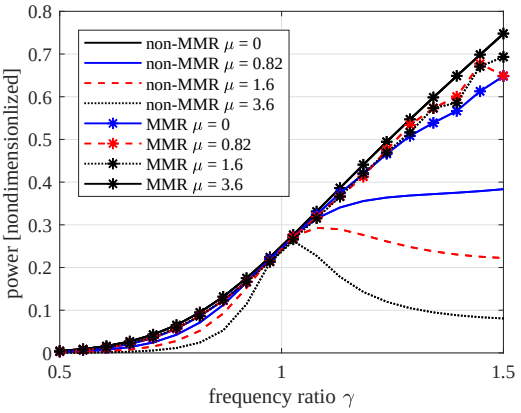


Figure 2.8: The frequency response of electric power output: non-MMR system vs. MMR system. All three cases have the same mechanical damping ratio 0.25.

As shown in *Figure 2.8*, at the primary frequency $\gamma = 1$, the MMR system has the same power output compared with the non-MMR based system. However, at all the other excitation frequencies (when $\gamma \neq 1$) the power output of MMR system is more than that of the non-MMR system. Especially at high frequency range, the benefit of the MMR system is obvious compared with the non-MMR system. By the definition of *Eq. 2.21*, the MMR based energy harvester has a P value of 0.28, 0.28, 0.28 for μ=0.82, 1.6, 3.6 respectively. The $\bar{P}$ value comparison is shown in Table 2.

From Table 2, the MMR based system has the same P value and it is larger than the non-MMR system. The MMR based system has broader bandwidth compared

Configuration \ Mass ratio	0.82	1.6	3.6
MMR	0.28	0.28	0.28
non-MMR	0.23	0.20	0.14

Table 2.2: Comparison of Pvalue

with the non-MMR based system. In the non-MMR based system, the bandwidth of frequency response narrows as mass ratio μ increases. However, in the MMR based system, the frequency response almost stays the same as the change of mass ratio μ.

2.5 Experiment verification of MMR based energy harvesting

2.5.1 Experiment set up and parameter identification

A suspension system consisting of one proof mass constrained to move vertically by two linear motion guides and suspended by two linear springs is built to verify the simulation results; see *Figure 2.9*. The MMR harvester is mounted on the frame while its racks are fixed to the suspended mass to convert the oscillation motion into electricity.

An Instron 3520 hydraulic power unit provides sinusoidal base excitation, and the frame is clamped to the moving part of the power unit. The proof mass is guided by two linear guides on the frame. The harvester is mounted on the frame and rack fixed on the proof mass. The relative displacement between the proof mass and the frame drives the pinion gear to rotate, and energy is harvested by the generator. The generator is electrically shunted by a 15 Ω resistor and the energy is dissipated by heat. Voltage output and force from the harvester to the base are measured and collected by a data acquisition system Spider-80. To characterize the system performance and compare the performance of the MMR and non-MMR based system, the system parameters were identified. The non-MMR system is the same with the MMR system except that it uses one set of rack and pinion, and there is no one-way bearing between the pinion gear and the shaft. The physical domain parameters are shown in Table 3. The parameters are obtained or derived from commercially available datasheets.

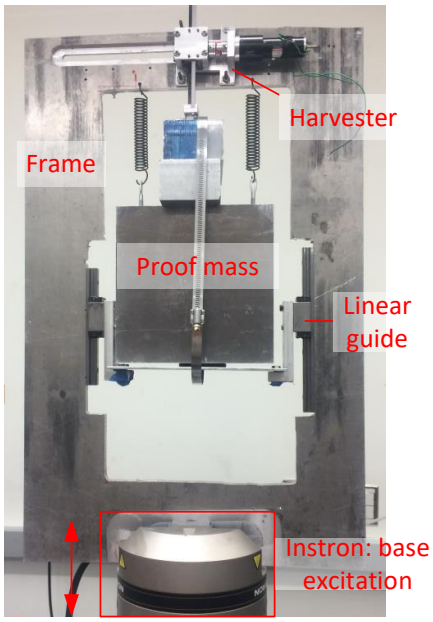


Figure 2.9: Base excitation experiment setup.

Symbol	Quantity	Parameter explanation
m	$13.6kg(30lb.)$	backpack suspended mass
m_e	$20.9kg$	generator rotor, gearbox rotation equivalent mass
k	MMR: $3750\frac{N}{m}$, non-MMR: $(m+m_e)\omega^2$	spring stiffness
c_e	$74.6Vs/m(R_L = 15\Omega)$	electrical damping
n	33	gear ratio
r	$7.9mm$	radius of pinion gear
R_i	0.2Ω	internal resistance
k_e	$1200rpm/V$	speed constant
k_t	$7.99 \times 10^{-3}Nm/A$	torque constant

Table 2.3: System parameters

All the system parameters can be obtained from commercially available datasheets except the system damping and friction, which is subject to prototyping precision, properties of component material, design, and environmental conditions. Those pa-

rameters are obtained by fitting numerical simulation results to experimental results. The damping of the frame c_f is calculated by free vibration test of the system with only spring and suspended mass (which is referred to as the method of logarithmic decremental; note that the harvester is not mounted in the system). Damping of the generator c_g can be fitted from the exponential decaying rate during the disengaged state, as described in *Eq. 2.24*. The fitting result is shown in *Figure 2.10(a)*. The engaged system mechanical damping c_m and friction F_r were obtained by a fitting process. By varying engaged mechanical damping c_m and friction values F_r, the least root mean square error between experimentally measured and simulated power responses under sweep sine excitation was obtained. The result is shown in *Figure 2.10(b)* and those two parameters are obtained.

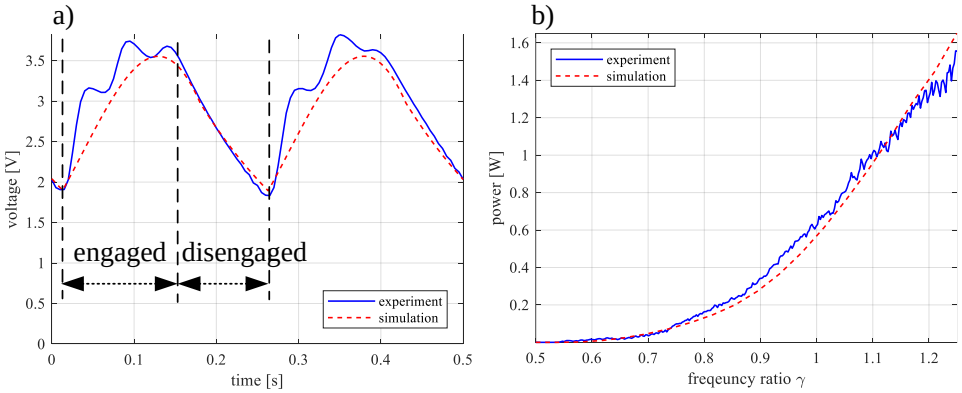


Figure 2.10: (a) Time-domain fitting to obtain generator damping c_g. (b) Fitting in the frequency domain to obtain engaged mechanical damping c_m and friction F_r. Excitation is $180s$, $1.0 \sim 2.5Hz$ sweep sine, 15 mm base excitation. Frequency is normalized to $2Hz$.

In this way, engaged mechanical damping c_m was characterized as $79\frac{Ns}{m}$, c_g as $40\frac{Ns}{m}$ and friction was $9N$. With the system modeling and parameters characterized, a simulation was done to compare with the experiment results.

The corresponding optimal spring stiffness for the MMR based system was 3450, 3800, and 3950 $\frac{N}{m}$ at =1.6, 3.6, and 5.3 respectively. However, due to the limitation in the choice of springs in the market, all the experiments were carried out with spring stiffness $3750\frac{N}{m}$. The error compared with the optimal spring stiffness was 5.1%, 1.3%, and -8.4%. This small error was considered ignorable.

Symbol	Quantity	Parameter explanation
c_f	$9\frac{Ns}{m}$	frame mechanical damping
c_m	$79\frac{Ns}{m}$	mechanical damping of engaged system
c_g	$40\frac{Ns}{m}$	mechanical damping of disengaged gearbox
F_r	$9N$	friction

Table 2.4: System damping and friction identified by curve fitting experimental data.

2.5.2 Experiment validation

The time domain signal of voltage output and power output were compared and shown in *Figure 2.11*.

As shown in *Figure 2.11*, the voltage output of the non-MMR based system has sinusoidal waveforms with zero average due to the up-and-down motion of the backpack. On the other hand, the voltage output of the MMR based system is always positive due to the engage and disengage of the two counter-direction one-way bearings in MMR. When the MMR input velocity cannot follow the generator rotation velocity, the driving pinion gear disengages. The generator rotational velocity subject an exponential decay described in Eq. (24). To find out the frequency response of both systems, a sweep sine test was done to both the MMR based system and non-MMR based system. The swept sine started at $1Hz$ and ends at $2.5Hz$. The frequency increase rate was constant, i.e., the sweep frequency increases linearly. The whole sweep sine period lasted for $180s$. The frequency increase rate was $0.008\frac{Hz}{s}$ and can be ignored in one cycle. In this way, the frequency in each cycle was considered constant. The base excitation amplitude was $15mm$, and the external resistor was 15Ω. The result is shown in *Figure 2.12*.

As shown in *Figure 2.12*, with damping and friction parameter estimation, the simulation result agrees well with the experiment. By the definition of *Eq. 2.21*, the $\bar{P}$ value for MMR and non-MMR are shown

It can be observed that for all three cases with different values, the MMR based system has much broader bandwidths compared with the non-MMR system. For the non-MMR system, the bandwidth decreases as the size of flywheel increases. However, for the MMR system, the bandwidth remains almost the same for all

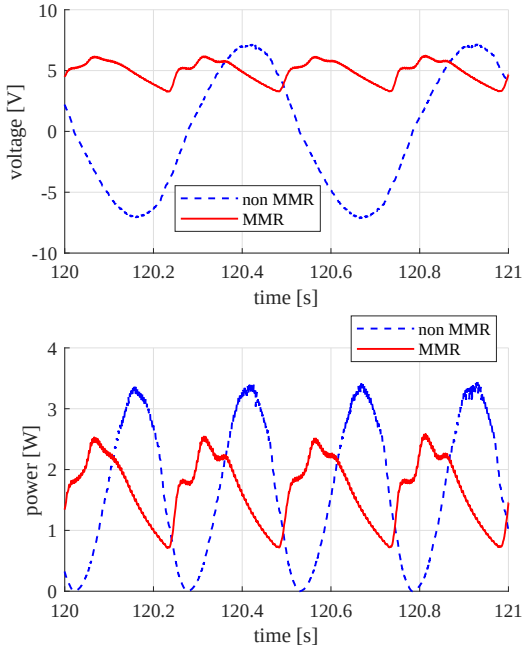


Figure 2.11: Time domain of voltage output and power output comparison: MMR vs. non-MMR. The amplitude of base excitation is $20mm$. The frequency is $2Hz$ and it is the resonance frequency of the non-MMR system. The external resistor is 15 Ω. The average power output for the MMR based system is $1.64W$. For non-MMR, it is $1.69W$. The power output at primary frequency is approximately the same.

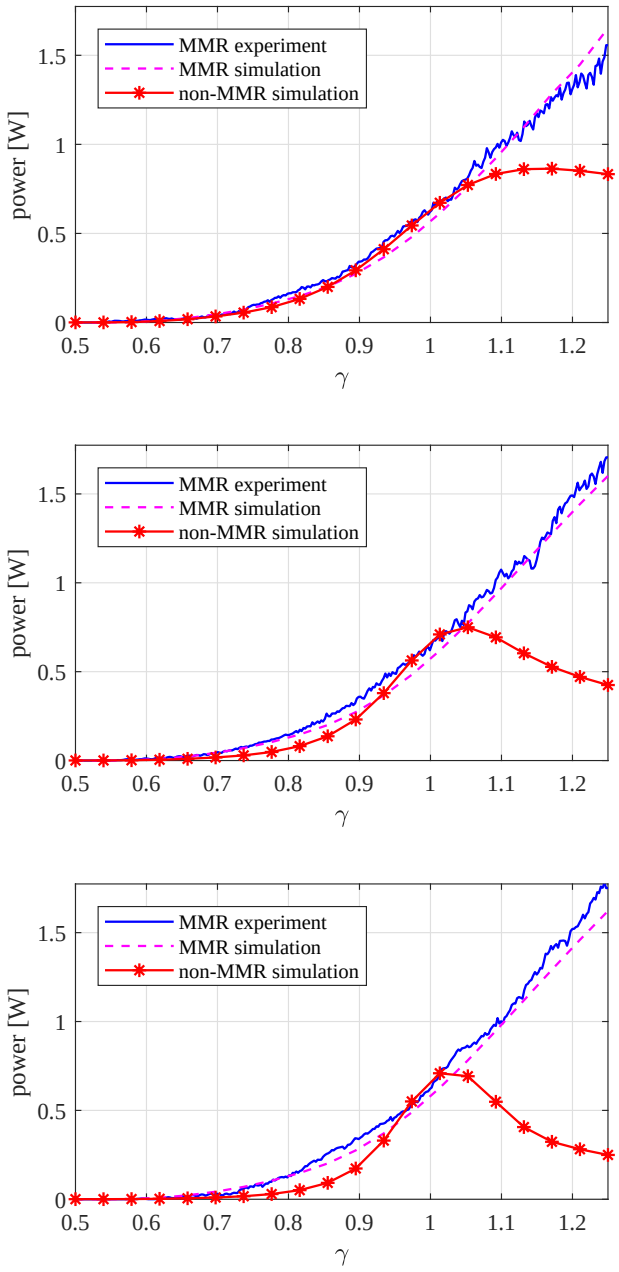


Figure 2.12: Power output frequency response: experiment vs. simulation. a) without flywheel, =1.6; b) with a small flywheel, =3.6; c) with a large flywheel, =5.3. Frequency is normalized to 2 Hz. Since non-MMR is a linear system and all the system parameters are known, the power output is simulated instead of experimentally measured.

Configuration \ mass ratio	1.6	3.6	5.3
MMR	0.11	0.12	0.12
non-MMR	0.09	0.07	0.05

Table 2.5: Comparison of P value

three different flywheel sizes. The difference might come from friction and damping changes due to the increase of flywheel size. The difference is small and can be ignorable. From experiments, we found out that the modeling is good and matches the experiment results. It is obvious that with the same mechanical damping, for the system with or without flywheel, both MMR and non-MMR have the same power output at optimized frequency 2 Hz. However, the increase of rotational inertia makes the frequency response narrow. With the help of MMR, the frequency response is much broader. Even the inerter equivalent mass changes, the frequency response of the MMR based system remains the same. This enhances the performance of the energy harvesting system. By comparing the system performance over the frequency range, it is found out that the MMR based system can have the same power with the non-MMR system at the primary frequency. MMR has better performance over all the rest frequencies other than the tuned frequency. The advantage is more obvious in high frequencies. This can explain why in the speed bump energy-harvesting system design, MMR was shown to harvest large impulses like energy more efficiently [53]. As the impulse consists of high-frequency components, the overall energy harvested in MMR based systems are much more than that of the non-MMR counterpart. The simulation results of the simplified model (which does not consider friction and only considers simplified damping conditions, introduced in Section 5.1) is also presented as the dark dotted line. From *Figure 2.12*, it can be observed that the experiment results match well with the full model simulation result. The experiment results do not match the simplified model very well. The reason for this might be the different friction and damping situations. However, MMR was shown to be broadband for both the full model and the simplified model. This further validates the conclusion that MMR makes the energy harvesting broadband.

2.5.3 Influence of MMR on force profile

As MMR was added into the energy harvesting system, the generator rotor will not change rotation direction as the system vibrates. Instead, the rotor will always

rotate in one direction. As the generator always rotates in one direction, the force profile due to inertia changes. Since the force F_g transmitted from the harvester to the base consists of inertia force and electromagnetic force, the profile of F_g changes due to MMR. As shown in *Figure 2.13*, with the same base excitation and both

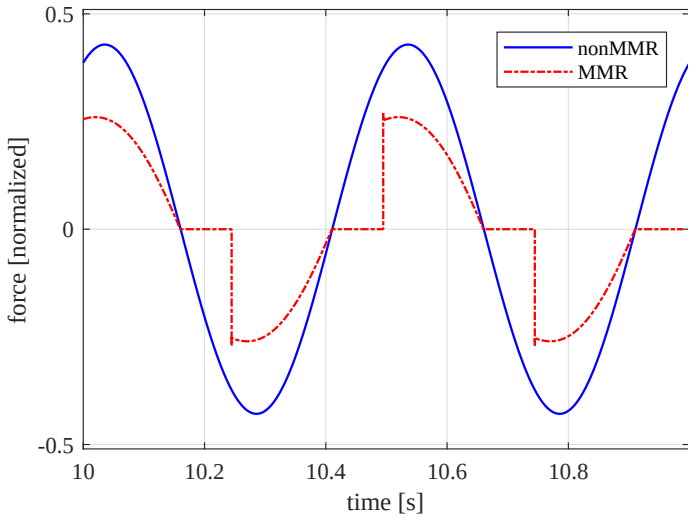


Figure 2.13: The force from harvester to base: MMR vs. non-MMR. The force is normalized to rotational inertia equivalent gravitational force m_e g. MMR and non-MMR system have the same base excitation $Y = 0.025\sin(4\pi t)$. Both are tuned to optimal condition and have the same optimal power output.

system tuned at optimal performance, the MMR harvester transmits a much smaller force to the base. Especially, when the system disengages, the force is zero. This decreased force on the base is another advantage that brought by the MMR. This reduced force profile can explain why MMR based shock absorber can have better ride comfort and road handling simultaneously [47]. The force from the harvester to the base is measured and compared with simulation. The result is shown as follows.

From *Figure 2.14*, we can see that the experiment result matches with the simulation result, except the impulse force at the engaging point, as shown by the dotted line at $10.24s$. When the rack movement velocity catches up with the rotation velocity of the generator rotor, there is a force spike due to the engagement collision. Other than that, the force from the MMR harvester to the base is much small compared with the non-MMR counterpart.

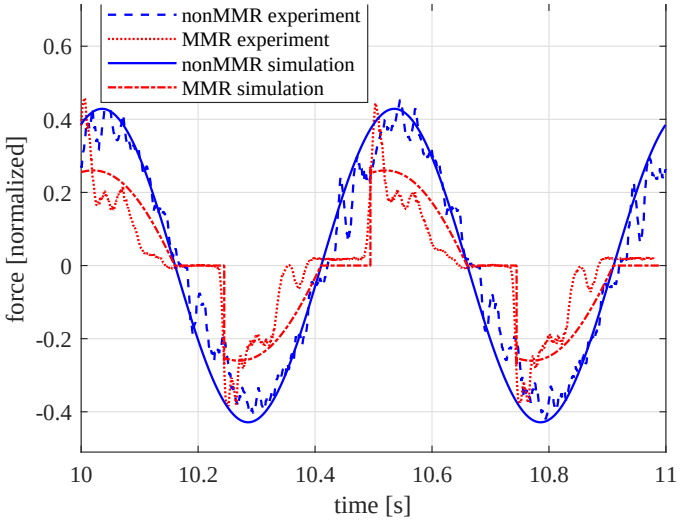


Figure 2.14: The force from harvester to the base. Excitation is $2Hz$, $20mm$ sinusoidal base excitation. $\mu = 1.6$ and external resistance is 15Ω. The force is normalized to $m_e g$.

2.6 Difference between experiment and modeling

The experiments do not match the modeling perfectly. I tried to use damping + friction model to address this issue. The experiment and simulation can match at some fixed excitation frequency. One of the examples is shown in *Figure 2.15*. There are some differences in the shape of the voltage output, which might be due to the rigidity of the connection. The connection (between the rack and the proof mass) is characterized as infinite stiffness spring; however, the stiffness is some large value instead of infinite. This can explain why we observe the ripples in voltage in the following figure (Experiment line in blue). The ripple is a high-frequency oscillation and can be explained by a spring with large stiffness. Except for those details, the simulation matches well with the experiment.

This is the method we obtain the mechanical damping. However, in the frequency response characterizing experiment, we observe something different.

As shown by *Figure 2.16*, the simulation result matches with the experiment result well when the frequency ratio is equal to 1. However, the experiment result is small at low frequencies, and larger at high frequencies compared with the modeling result, as illustrated by the blue dash line. This can be explained by the damping modeling.

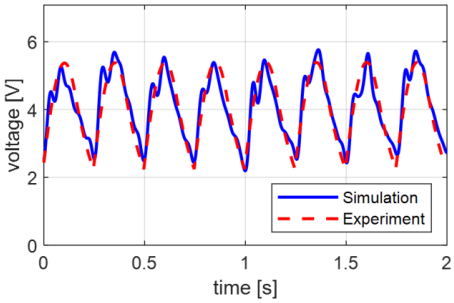


Figure 2.15: Time domain comparison of experiment result and modeling results. The experiment result matches well with the modeling result with acceptable error.

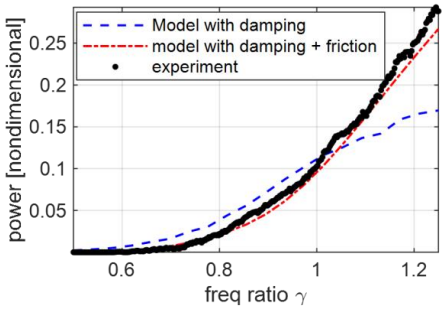


Figure 2.16: Frequency domain comparison of experiment result and modeling results.

The damping is modeled as a Columbus damping; however, the real situation can be more complicated. If we move a step further and model the system to have a damping + friction term, we can get closer simulation result, as shown by the red dash line in *Figure 2.16*.

At lower frequencies, the experiment result is smaller because frictions effect is larger when the excitation is smaller. As the force provided by damping is $c_e\dot{x} = c_e\omega x$, and will increase as the increase of amplitude or frequency. However, the friction is modeled as a constant force and will be constant no matter how the excitation changes. At lower excitation frequencies, frictions effect will be larger than the damping. While at high frequencies, the dampings effect will be larger than the friction. As a result, the experiment result is larger at high frequencies and small at low frequencies if only the damping model is used. With friction + damping, the experiment result fits with the modeling result much better.

2.7 Backpack energy harvester experiment with human subjects

In order to compare the performance of the MMR based backpack and the non-MMR based backpack. Experiment is done with the primary author himself and one labmate walking on a treadmill. Power output data is collected and analyzed as follows. Each experiment trial lasts 5 min, with power data collected in the last 2 min of the 5 min. There is a 3 min time rest between each trial. Conclusions are given: the result matches with the modeling result in trend. However, the experiment results and the modeling results do not match one by one in detail. The difference might be explained by the unmodeled human backpack interaction, the difference in individuals.

As observed in *Figure 2.17*, the power of non-MMR (linear) system will reach zero due to the back-and-forth motion of the generator. On the other hand, due to the MMR, the generator will keep rotating in one direction and the instant power never reaches zero. The average power output at different walking speed (different excitation frequency) is shown in *Figure 2.18*. The experiment is repeated three times for each of the two subjects. The mean value and standard deviation is plotted in *Figure 2.18*.

As illustrated in *Figure 2.18*, the power output at 2 Hz is around 3W, which is consistent with the modeling and simulation result for subject B. However, in subject

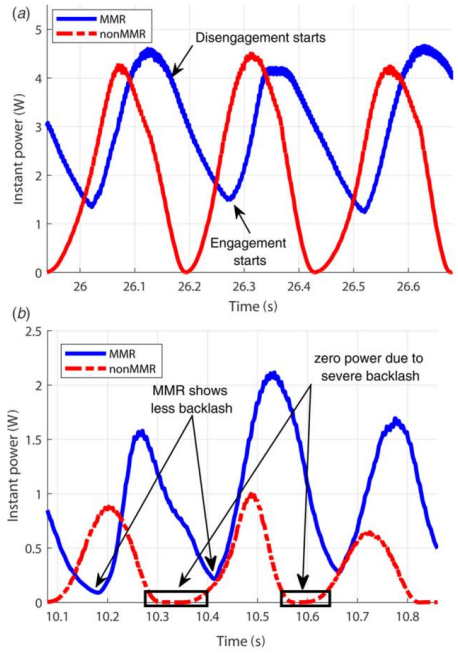


Figure 2.17: Instant power of MMR and non-MMR backpack for each subject: (a) subject A and (b) subject B. Walking speed: 4.8 km/h

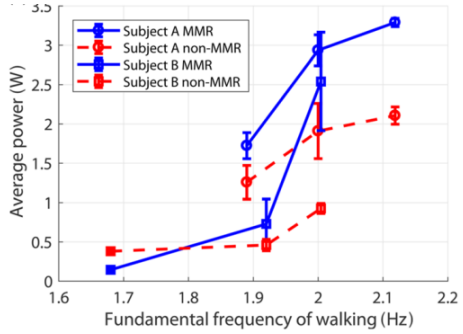


Figure 2.18: Treadmill based human walking backpack-energy-harvesting result on frequency domain.

A we observes less power output in all frequencies. More experiments with a larger number of subjects is required before any conclusion can be drawn. It is noted that the experiment is done only for the MMR based SDOF energy harvesting backpack. I have done more work on the inerter-based 2DOF system, MMR based 2DOF system, but none of those is validated by the backpack experiment with human participants. Instead, an easily controlled based excitation experiment is done to validate the modeling and simulation. In order to find out more about the human backpack performance, more human participant based experiment should be done and that is very interesting future work.

2.8 Why MMR can increase the energy harvesting frequency bandwidth

For the linear SDOF energy harvesting, as the equivalent mass of the generator rotor m_e is in the denominator of the power output function, i.e.

$$P = \frac{1}{2}c_e\ddot{z}^2 = \frac{1}{2}c_e\frac{m^2\omega^6Y^2}{[k-(m+m_e)\omega^2]^2+(c_m+c_e)^2\omega^2} \tag{2.28}$$

The power output at resonance frequency will not affected, because $k-(m+m_e)\omega^2 = 0$. However, when $k-(m+m_e)\omega^2 \neq 0$, the power will decrease as the increase of m_e, as $\frac{\partial P}{\partial m_e} < 0$. As a result, the increase of m_e will cause a decrease of power. This causes the narrow frequency bandwidth effect. Now let us discuss the case with MMR. The SDOF linear energy harvesting (*Figure 2.19* (a)) can be transformed to an analogous electric circuit (c). Similarly, the MMR based energy harvesting (b) can be transformed to analogous electric circuit (d). The analogous circuit transform is possible because the structure of the Equation of Motion (EOM) in the mechanical domain corresponds to the electrical domain and shown as follows.

$$\begin{cases} (m+m_e)\dot{v}+(c_m+c_e)v+k\int v = -m\ddot{y} & \textit{mechanical} \\ (C+C_e)\dot{V}+\frac{V}{R+R_e}+\frac{1}{L}\int V = i & \textit{electrical} \end{cases} \tag{2.29}$$

From the analysis of (d), it is obvious that the capacitor (c_e) becomes a voltage smoothing capacitor and is not in the LC circuit any more (as in the (c) case). This explains why the MMR can make the system broadband. The MMR can be treated as a damping term R and a smoothing capacitor c_e and illustrated in *Figure. 2.20.*

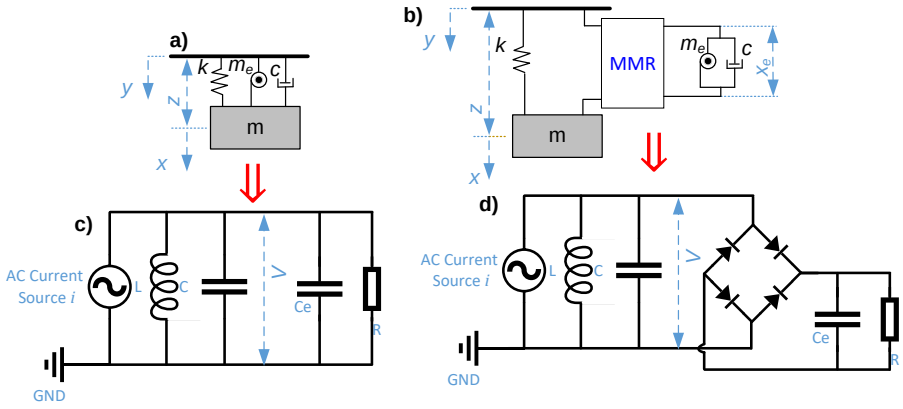


Figure 2.19: Linear (non-MMR) / MMR energy harvesting system and their electric equivalent. a) Linear energy harvesting system; b) MMR based energy harvesting system; c) equivalent electric circuit for the linear (non-MMR) energy harvesting system; d) equivalent electric circuit for the MMR based energy harvesting system.

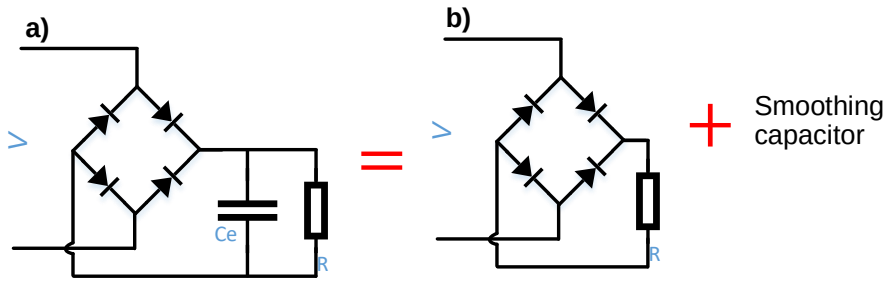


Figure 2.20: The equivalent electrical model of the MMR. Instead of being the capacitor in the LC circuit, the capacitor becomes a smoothing capacitor.

The voltage profile on the resistor R is described in *Figure. 2.21.*

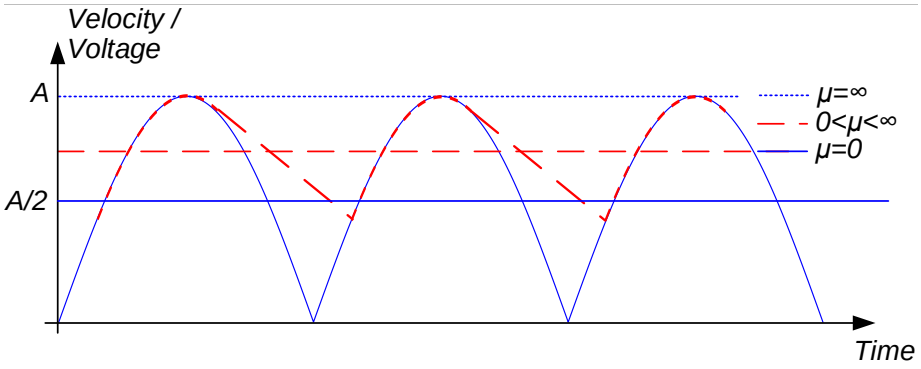


Figure 2.21: Velocity / Voltage profile for the resistor R for three cases $\mu = 0$,$0 < \mu < \infty$, and $= \infty$.

From *Figure. 2.21*, the voltage output profile is absolute of sinusoidal when $\mu = 0$, and for this case the power output is the same as the linear case. As the output shape is absolute of sinusoidal, the RMS value is half of the amplitude A. When $\mu = \infty$, the voltage output profile is equal to A and is a constant. As a result, the RMS value is A, and doubles the linear (non-MMR) case. As the resistor R does not change through those cases, the effective resistor changed from R to $2R$ because of the increased effective voltage profile. When the mass ratio $0 < \mu < \infty$, the RMS value is between $\frac{A}{2}$ and A. As a result, the resistance / damping increases from R to $2R$ (damping increase from c to $2c$. Resistance in electrical domain corresponding to damping in mechanical domain. When $c_e' = c_m$,

$$P = \frac{1}{2} c_m \frac{m^2\omega^4 Y^2}{(c_m + c_m)^2} = \frac{m^2\omega^4 Y^2}{8c_m} \tag{2.30}$$

When $c_e' = 2c_m$,

$$P = c_m \frac{m^2\omega^4 Y^2}{(2c_m + 2c_m)^2} = \frac{m^2\omega^4 Y^2}{16c_m} \tag{2.31}$$

which indicates that the power will decrease to half. With a quick simulation, we can obtain the power output for different μ value, and find out that the average power decrease from P at $\mu = 0$ to close to $\frac{P}{2}$ at $\mu = \infty$.

As observed from *Figure 2.22*, the power output becomes smooth as the increase of mass ratio μ increases. The mean power decreases as the increase of the mass ratio μ, which can be illustrated more obvious in *Figure 2.23.*

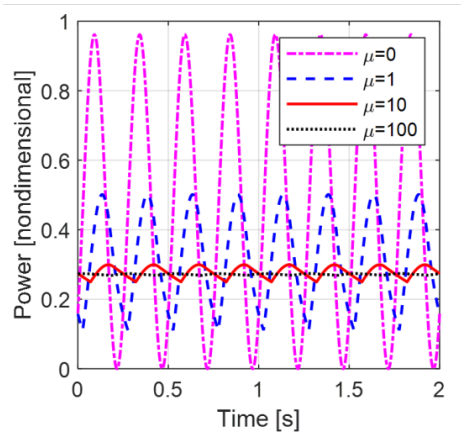


Figure 2.22: MMR based energy harvesting system power output for different μ values.

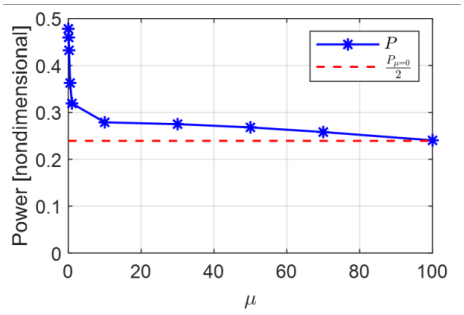


Figure 2.23: Average power output vs. mass ratio for MMR based energy harvesting system.

As observed from *Figure 2.23*, the power output decrease to $\frac{P_{\mu=0}}{2}$ when $\mu = \infty$. This matches with the analytical result exactly.

In this way, I think I have explained why MMR makes the system broad bandwidth. The key is that MMR turns the capacitor in LC circuit into a smoothing capacitor (that is analogous to turn the equivalent mass from the inerter in the spring-mass oscillation loop into a (velocity) smoothing mass). Assume the power harvested is $P_{\mu=0}$ at $\mu = 0$. For the linear system (non-MMR based), the increase of μ will decrease the power and eventually to 0 when $\mu = \infty$. The MMR will make the effective output voltage double and the equivalent resistance double, and hence the equivalent damping double. This will decrease the power to $\frac{P_{\mu=0}}{2}$ when $\mu = \infty$. This is much larger than the 0 power from the linear system (non-MMR) base, and hence the frequency bandwidth is improved.

2.9 Performance of MMR in systems under excitation with constant force amplitude

In this section, the performance of the non-MMR and MMR based system under excitation with constant force amplitude will be compared. The same as base excitation case, the optimal performance of the non-MMR system is obtained first.

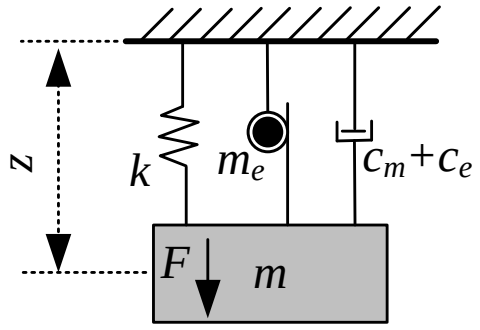


Figure 2.24: Modeling of rotational electromagnetic generator based vibration energy harvesting system with force excitation.

The equation of motion for the force excited non-MMR system is

$$(m + m_e)\ddot{x} + (c_m + c_e)\dot{x} + kx = F \tag{2.32}$$

Average electrical power output and its nondimensionalized form can be obtained as

$$P = \frac{1}{2}c_e\dot{x}^2 = \frac{1}{2}c_e\frac{\omega^2 F^2}{[k - (m + m_e)\omega^2]^2 + (c_m + c_e)^2\omega^2} \tag{2.33}$$

Nondimensionalization leads to

$$P = \frac{P}{F^2/m\omega_0} = \frac{\xi_e\gamma^2}{(1+\mu)^2(\alpha^2 - \gamma^2)^2 + 4\gamma^2(\xi_m + \xi_e)^2} \tag{2.34}$$

When the excitation frequency is the same with the primary excitation, i.e. $\gamma = \frac{\omega}{\omega_0} = 1$, the power output is

$$P(\gamma = 1) = \frac{\xi_e}{(1+\mu)^2(1 - \alpha^2)^2 + 4(\xi_m + \xi_e)^2} \tag{2.35}$$

The same optimal power can also be obtained, the same way as in the base excitation case. Mathematically speaking, the necessary condition for a local extremum of *Eq. 2.35* is

$$\frac{\partial P}{\partial \alpha} = \frac{\partial P}{\partial \xi_e} = 0 \tag{2.36}$$

Solve for optimal α^{opt} and ξ_e^{opt}, respectively, lead to

$$\begin{cases} \alpha^{opt} = 1 \\ \xi_e^{opt} = \xi_m \end{cases} \tag{2.37}$$

After applying the optimal spring ratio α^{opt} and optimal electric damping ratio ξ_e^{opt} to *Eq. 2.34*, power frequency response can be obtained as

$$P^{opt}(\gamma) = \frac{\xi_m\gamma^2}{(1+\mu)^2(1 - \gamma^2)^2 + 16\gamma^2\xi_m^2} \tag{2.38}$$

As the same with the base excitation case, MMR can also be integrated and modeled as *Figure 2.25*.

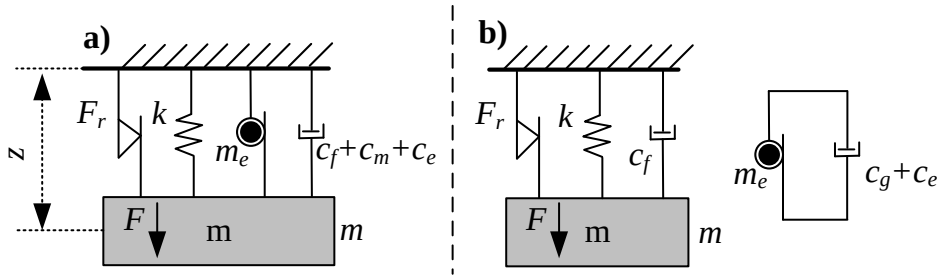


Figure 2.25: Modeling of MMR based vibration energy harvesting system under force excitation.

The MMR system and non-MMR system performance under the same excitation were compared and the result is shown in *Figure 2.26*.

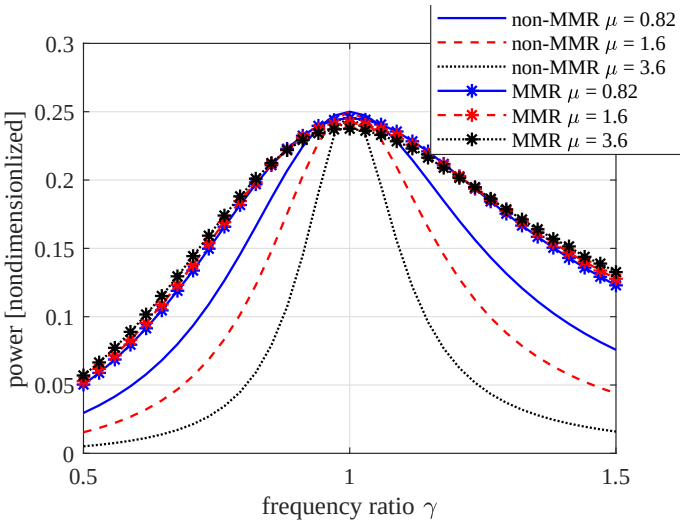


Figure 2.26: Power output from force excitation comparison, damping ratio is $\xi_m = 0.25$.

As we can see from *Figure 2.26*, MMR can increase the bandwidth for all different

cases of μ. On the other hand, the non-MMR system has narrower bandwidths as the inerter mass m_e increases. In other words, the adverse influence of inerter mass m_e on energy harvesting is reduced by MMR also when force excitation is considered.

Chapter conclusions

The influences of inerter on energy harvesting are studied in this paper. When base excitation is considered, the bandwidth decreases due to the increase of rotational inertia. To solve this problem, a type of inertia nonlinearity was introduced by using mechanical motion rectifier (MMR). Frequency responses of the power output of the MMR system were simulated and compared with the counterpart without MMR. The power output of the MMR based system at primary frequency is the same as that of the non-MMR system. However, at all other frequencies, the MMR based system has more power output. The broad bandwidth feature of the MMR based energy harvesting system was validated by experiments. It turns out that by adding MMR to the energy harvesting system, the influence of the inerter on reducing power output in frequency responses was reduced. Simulation and experiments also show that after adding MMR, the force from the harvester to the base was reduced. For harmonic excitation with constant force amplitude, the MMR based system also had much broader bandwidths compared with the counterpart without MMR.

Appendix

By Newton's 2nd law, the equation of motion for base excitation in *Figure 2.3* is

$$m\ddot{z} + c\dot{z} + kz = -m\ddot{y} \tag{2.39}$$

where rotational inertia is not considered and $c = c_m + c_e$. All the energy dissipated in the system is

$$P(\gamma) = \frac{1}{2}c\dot{z}^2 = m\omega_n^3 Y^2 \frac{\xi_{combined}\gamma^6}{(1-\gamma^2)^2 + 4\gamma^2\xi_{combined}^2} \tag{2.40}$$

where $\omega_n = \sqrt{\frac{k}{m}}$, $\xi_{combined} = \frac{c}{2\sqrt{mk}}$, $\gamma = \frac{\omega}{\omega_n}$, and ω is the excitation frequency. Mathematically speaking, the necessary condition for a local extremum of *Eq. 2.40* is

$$\frac{\partial P}{\partial \gamma} = 0 \tag{2.41}$$

Solve for γ lead to

$$\begin{cases} \gamma_1 = \sqrt{(2 - 4\xi_{combined}^2 - \sqrt{1 - 16\xi_{combined}^2 + 16\xi_{combined}^4}} \\ \gamma_2 = \sqrt{2 - 4\xi_{combined}^2 + \sqrt{1 - 16\xi_{combined}^2 + 16\xi_{combined}^4}} \end{cases} \tag{2.42}$$

γ_1 corresponding to the maximum power and γ_2 corresponding to the minimum power point. Substitution of *Eq. 2.42* into *Eq. 2.40* and solving the following inequality

$$\frac{1}{2}P(\gamma_1) > P(\gamma_2) \tag{2.43}$$

lead to

$$\xi_{combined} < 0.147 \tag{2.44}$$

This indicates when $\xi_{combined} < 0.147$ there is no half-power bandwidth. Otherwise, the power output will never decrease to be lower than half of the maximum power output when the driving frequency increases.

Chapter 3

Two-degree-of-freedom based Energy Harvesting Backpack

3.1 Chapter introduction

With the ever-rising popularity of electronics such as sensors, wearable , and portable devices, many energy harvesting technologies have been developed to harness electricity from different sources, such as vibration, thermal, and solar energy. Among them, electromagnetic generator based systems are widely applied in large-scale vibration energy harvesting [17]. Electromagnetic generators can be linear [34] or rotational [41]. Compared with linear generators, rotational generators have a high power density and power output. The advantage is more prominent with the use of gearboxes. Therefore, the rotational generator-based energy harvesting systems require a much smaller size and weight for the same power output [34] [41] [54]. However, the gearbox used in rotational system increases the inertance of the generator rotor [41]. The generator rotor and the mechanism to convert the linear to rotational motion is an inerter in the system. Inerter is defined as a mechanical two-terminal device with the property that the equal and opposite force applied at the terminals is proportional to the relative acceleration between the terminals [38]. Inertance is an equivalent mass term of the inerter and defined as $\frac{F}{\dot{v}_2 - \dot{v}_1}$, where F is the force on the inerter and v_1 and v_2 are the velocity of the two terminals respectively [38]. In modeling, it is equal to $\frac{J}{r^2}$, in which J is the rotational inertial of the inerter and r is the rotation motion to linear motion ratio. The inerter cannot be neglected in many energy harvesting systems [41]. The decrease of bandwidth due to the increase of inertance is discussed

in [7]. The use of gearbox in an energy harvesting system causes a trade-off between power density and frequency bandwidth. In many applications, however, both high power output and broad bandwidth are desired.

Many vibration energy harvesting systems can be modeled as a single-degree-of-freedom (SDOF) spring-mass-damper system, in which the optimal system performance is achieved when the excitation frequency matches its resonance frequency and the electrical impedance is equal to the mechanical impedance [21] under harmonic base excitation with constant amplitude. However, SDOF systems only work efficiently with limited frequency bandwidth near their resonant frequencies. That frequency bandwidth decreases with the decrease of damping ratio [55]. If the excitation frequency slightly shifts from the resonance frequency, the performance of the harvester can dramatically decrease [56]. Unfortunately, the vast majority of practical vibration sources are of broad bandwidth or have time-varying frequencies [57], which inevitably leads to decreased energy harvesting performance. Even at the resonant frequency, the electrical power output is also constrained by the mechanical damping and maximum stroke limit [21] [22].

To overcome the limitations of the SDOF energy harvesting system, researchers seek alternative systems [58]. Among them, two-degrees-of-freedom (2DOF) energy harvesting systems show great potentials [59] [60] [61] [62] [63] [64]. Conventionally, a 2DOF system has either two moving masses with each mass able to move in the same direction or one mass with two moving directions. A 2DOF piezoelectric energy harvesting device that uses both translational and rotational degrees of freedom was proposed [59]. Compared with conventional SDOF energy harvester, the 2DOF system has two different resonance frequencies and the frequency bandwidth is significantly increased. By adding a second mass, Ma *et al.* [60] designed a dynamic piezoelectric vibration energy harvester that can generate power of orders of magnitude larger than that of a conventional beam and the frequency bandwidth was enlarged. Tang *et al.* proposed a dual-mass energy harvesting system by introducing a second oscillator to an SDOF system [61]. Optimal parameters were analyzed and discussed for maximum power output. It was shown that by adding a second oscillator, more power could be obtained for both harmonic excitations with constant acceleration amplitude and constant displacement amplitude. Aldraihem *et al.* [62]and Aladwani *et al.* [63] used one mass as dynamic amplification to increase the amplitude of vibration sources. Their results show that the harvested power can be amplified by a factor of 20 compared to the conventional piezoelectric en-

ergy harvester. The effective bandwidth can be widened to cover sidebands that are about ±25% of the resonant frequency of the conventional harvester. Zhou *et al.* [64] proposed a double-beam harvester which is capable of significantly increasing the bandwidth at all resonances virtually and the amount of energy harvested from the ambient vibrations. The research on multiple degree-of-freedom systems is interesting and meaningful. However, the increased power output is obtained at a large stroke. Few researchers consider the limitation of stroke while striving for large power output. In most energy harvesting applications, space is not limitless. Maximum stroke limit is a concern in many vibration energy harvesting systems [21] [22]. One example of stroke limitation is that large stroke in energy harvesting backpacks makes the backpack motion interfere with the wearer walking and thus makes it uncomfortable to wear.

Another issue in current 2DOF energy harvesters is that considerable extra physical mass has to be added [61] [60] [62] [63] [64]. However, weight is a concern in many energy harvesting applications. For example, it is hard to add extra weight in biomechanical energy harvesting systems because the user may feel burden and experience fatigue due to the extra weight [3] [4]. Therefore, conventional 2DOF energy harvesters do not fit such situations. It is critical to find a way that can take advantage of 2DOF systems while do not add extra weight.

In this paper, we proposed an inerter-based 2DOF energy harvesting system by utilizing the inertance of the electromagnetic generator as a second oscillator. The second oscillator is achieved by adding a spring in series with the inerter to the conventional SDOF system. Very small weight (weight of a spring) is added compared with the counterpart SDOF system. Improved performance, such as larger power output and wider bandwidth, is obtained. The analytical results are validated by experiments. Both analytical and experimental results show that the inerter-based 2DOF system can achieve better performance over a larger excitation frequency range compared with counterpart SDOF system.

The rest of this paper is organized as follows. The performance limitations of the SDOF system will be presented in *Section 3.2*. In *Section 3.3*, the design and modeling of the proposed inerter-based 2DOF energy harvesting system under harmonic excitation will be presented. Parameter optimization and optimization result will be presented in *Section 3.4*. The system performance is compared with the counterpart SDOF system under the same stroke limitation. In *Section 3.5*, experiment valida-

tion will be presented. Discussion will be in *Section 3.6*. Finally, conclusions will be given in Section 7.

3.2 Performance limitations of SDOF harvesters

When harvesting the energy from a vibration source, such as bridges [65], buildings [66], vehicles [57], humans [4], etc., a single-degree-of-freedom (SDOF) system that consists of a mass, a spring, and a damper are often used. The mathematical model is shown in *Figure 3.1*. Suspended mass m is connected with the base by a spring with stiffness k and a damper with damping coefficient c. The damping coefficient c my include the mechanical damping coefficient c_m and the electrical damping coefficient c_e, which is an equivalent damping coefficient provided by the generator. For rack-pinion based electromagnetic energy harvester, the c_e is determined by generator speed constant k_e, generator torque constant k_t, generator load, pinion radius r, and gear ratio n [7], as follows

$$c_e = \frac{n^2 k_t k_e}{(R_i + R_L) r^2} \tag{3.1}$$

where R_i and R_L are the internal and external resistance of the generator. In many electromagnetic energy harvesting systems, the rotational inertia of the generator rotor cannot be neglected [41]. The equivalent mass for the generator rotor is $m_e = J_e * n^2/r^2$, where J_e is the generator rotational inertia, n is gear ratio, and r linear-to-rotation motion ratio, for example, pinion radius [7]. In this regard, the generator is modeled as a damper and an inerter in the linear vibration system, which has equivalent damping $c = c_m + c_e$ and inerter m_e. It is noted that a large equivalent inerter m_e can be obtained from a small physical mass with large gear ratio n and small pinion radius r. As illustrated in the experiment part, an equivalent mass of $20.9kg$ can be obtained from $0.5kg$ of physical mass (the generator).

The governing equation of motion of the system is

$$(m + m_e)\ddot{z} + c\dot{z} + kz = -m\ddot{y} \tag{3.2}$$

where the excitation is modeled as a displacement input with $y = Ye^{j\omega t}$, where Y is the displacement amplitude, and ω is the angular frequency of the excitation. z is the relative displacement between the base and the suspension mass, i.e. $z = x - y$. The response can be defined as $z = Ze^{j\omega t}$. Nondimensionalization can be done by the

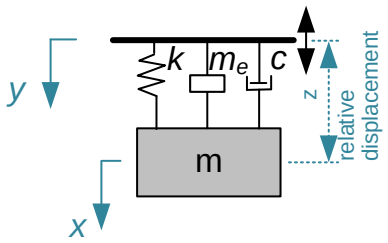


Figure 3.1: Typical SDOF base excitation energy harvesting system

following definitions: mass ratio $\mu = \frac{m_e}{m}$, damping ratio $\xi = \frac{c}{2m\omega_0}$, $\xi = \xi_m + \xi_e$, natural frequency $\omega_n = \sqrt{\frac{k}{m+m_e}}$, and tuning ratio $\alpha = \frac{\omega_n}{\omega_0}$. For many energy harvesting scenarios, the excitation frequency is dominated by one or several frequencies, and is called primary frequency [57] [67] [48]. In this paper, the energy harvesting system is tuned to perform the best at the primary excitation frequency and thus the primary excitation frequency is called "target frequency". The target frequency is denoted as ω_0 and is assumed to be constant. Excitation frequency ratio is $\gamma = \frac{\omega}{\omega_0}$. Then the nondimensionalized equation of motion is

$$(1+\mu)(\alpha^2 - \gamma^2)Z + j2(\xi_m + \xi_e)\gamma Z = \gamma^2 Y \tag{3.3}$$

The system should be tuned to have optimal performance at the target frequency. Through some derivation (the interested readers can refer to [7] for the detailed derivation), one can show that the nondimensionalized optimal power output at the target frequency, i.e. $\gamma = 1$ is

$$\bar{P}^{opt}_{\gamma=1}(\xi_m) = \frac{P^{opt}_{\gamma=1}(\xi_m)}{m\omega_0^3 Y^2} = \frac{1}{16\xi_m} \tag{3.4}$$

where $P^{opt}_{\gamma=1}(\xi_m)$ is the optimal physical power output. The optimal power is plotted as a function of damping ratio in *Figure 3.2 a)* as blue line. In other words, the power from a SDOF system is bounded by the blue line (green shaded area). Based on *Equation 3.4*, the maximum power of the SDOF system is limited by the mechanical damping ratio.

In many applications, having a large stroke is less than ideal for energy harvesting systems. One example is the energy harvesting backpack. Large strokes will interfere with the wearer walking, thus making the user uncomfortable. Furthermore, in many applications, the harvester is confined in a limited physical space and the stroke

cannot exceed that limitation[68] [69]. As a result, the optimal power output is limited by the stroke. Suppose that an energy harvesting system has a limited stroke A, the optimal electrical damping at the target excitation frequency is obtained by solving

$$Z(\gamma=1)=\frac{Y}{\sqrt{[(1+\mu)^2(1-\alpha^2)^2+4(\xi_m+\xi_e)^2}}\leq\frac{A}{2} \tag{3.5}$$

where Z is the relative displacement of the moving mass. The electrical damping is found as

$$\xi_e\geq\frac{\sqrt{\frac{4Y^2}{A^2}-(1+\mu)^2(1-\alpha^2)^2}}{2}-\xi_m \tag{3.6}$$

The nondimensionalized optimal power output is

$$\bar{P}^{opt}_{\gamma=1}(\kappa,\alpha)=\frac{P^{opt}_A}{m\omega_0^3Y^2}=\frac{\frac{1}{2}c_e\dot{z}^2}{m\omega_0^3Y^2}=\frac{1}{4}\kappa^2(\frac{1}{2}\sqrt{\frac{4}{\kappa^2}-(1+\mu)^2(1-\alpha^2)^2}-\xi_m) \tag{3.7}$$

where $\kappa=\frac{A}{Y}$ is defined as the stroke limit ratio.

Taking derivative of $\bar{P}^{opt}_{\gamma=1}(\kappa,\alpha)$ over α, $\frac{\partial\bar{P}^{opt}_{\gamma=1}(\kappa,\alpha)}{\partial\alpha}=\frac{1}{2}(1+\mu)^2(1-\alpha^2)\alpha\kappa^2[\frac{4}{\kappa^2}-(1+\mu)^2(1-\alpha^2)^2]^{-\frac{1}{2}}$ can be obtained. One can find that $\frac{\partial\bar{P}^{opt}_{\gamma=1}(\kappa,\alpha)}{\partial\alpha}>0$ when $\alpha<1$, and $\frac{\partial\bar{P}^{opt}_{\gamma=1}(\kappa,\alpha)}{\partial\alpha}<0$ when $\alpha>1$. Therefore the maximum power point happens at $\alpha=1$ when there is a stroke limit. This indicates that α should be set to be 1 in order to obtain the maximum power. Apply $\alpha=1$, the optimal power is

$$\bar{P}^{opt}_{\gamma=1}(\kappa)=\frac{P^{opt}_A}{m\omega_0^3Y^2}=\frac{\frac{1}{2}c_e\dot{z}^2}{m\omega_0^3Y^2}=\frac{1}{4}\kappa(1-\kappa\xi_m) \tag{3.8}$$

The stroke limit ratio will not be a constraint if it is larger than the stroke ratio of the optimized system at ξ_m. It can be calculated from *Eq. 11* in [7] that when the system is tuned optimum, the nondimensionalized stroke ratio is $\frac{1}{2\xi_m}$. As a result, the optimal power is

$$\bar{P}^{opt}_{\gamma=1}(\kappa)=\begin{cases}\frac{1}{4}\kappa(1-\kappa\xi_m) & \kappa<\frac{1}{2\xi_m}\\ \frac{1}{16\xi_m} & \kappa\geq\frac{1}{2\xi_m}\end{cases} \tag{3.9}$$

The optimal power output in *Equation 3.9* is plotted over κ and shown in*Figure 3.2 (b)*. Any performance beyond the optimal performance line is impossible for SDOF system. It is noted that the power limitation in *Figure 3.2 (b)* is flat when $\kappa>5$. This is because when $\kappa>5$, the stroke is not a limitation any more. The

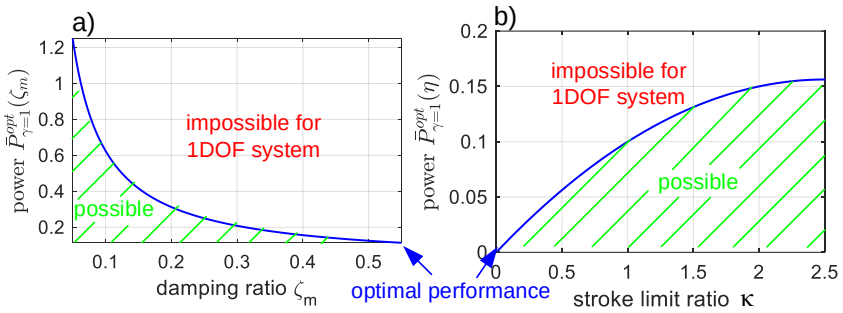


Figure 3.2: (a) Power output vs. mechanical damping, where $\mu = 1$. (b) Power output vs. stroke limit, where $\kappa = A/Y$, $\mu = 1$, and $\xi_m = 0.1$.

optimal power output is only limited by the mechanical damping. To characterize the performance of an energy harvesting system, three performance indices, i.e. power, stroke, and power-to-stroke ratio are proposed. To demonstrate how the inertance influences the performance indices, the frequency response function of each index is plotted with three different mass ratios, as shown in *Figure 3.3*.

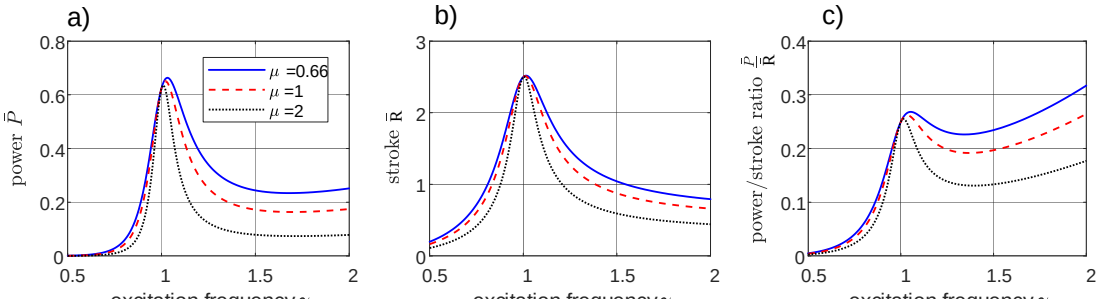


Figure 3.3: Constant amplitude base excitation energy harvesting frequency response. a) power; b) stroke; c) power-to-stroke ratio. The result is plot with $\xi_m = 0.1$.

As shown in *Figure 3.3*, all the systems are tuned to have optimal power at the primary excitation frequency. Therefore, the power, stroke, and power to stroke ratio are the same when $\gamma = 1$. All three cases with different mass ratios μ have limited half-power bandwidth. As μ increases, the bandwidth decreases. For the rest of this paper, the optimal performance shown in *Figure 3.3* will be referred to as the performance limit of the SDOF system. To overcome the performance limits of the SDOF system, an inerter-based 2DOF system is proposed and discussed in the following sections.

3.3 Design and Modeling of inerter-based 2DOF energy harvesting system

Inerter-based 2DOF system is achieved by adding one spring (k_2) in series with the inerter in the SDOF energy harvesting system. The lumped model is shown in *Figure 3.4* and used as a benchmark model. z is the stroke and x_e is the equivalent linear displacement of the generator rotation motion. Before adding the spring, x_e is the same as the stroke z. After adding spring k_2, one more degree of freedom is added to the system.

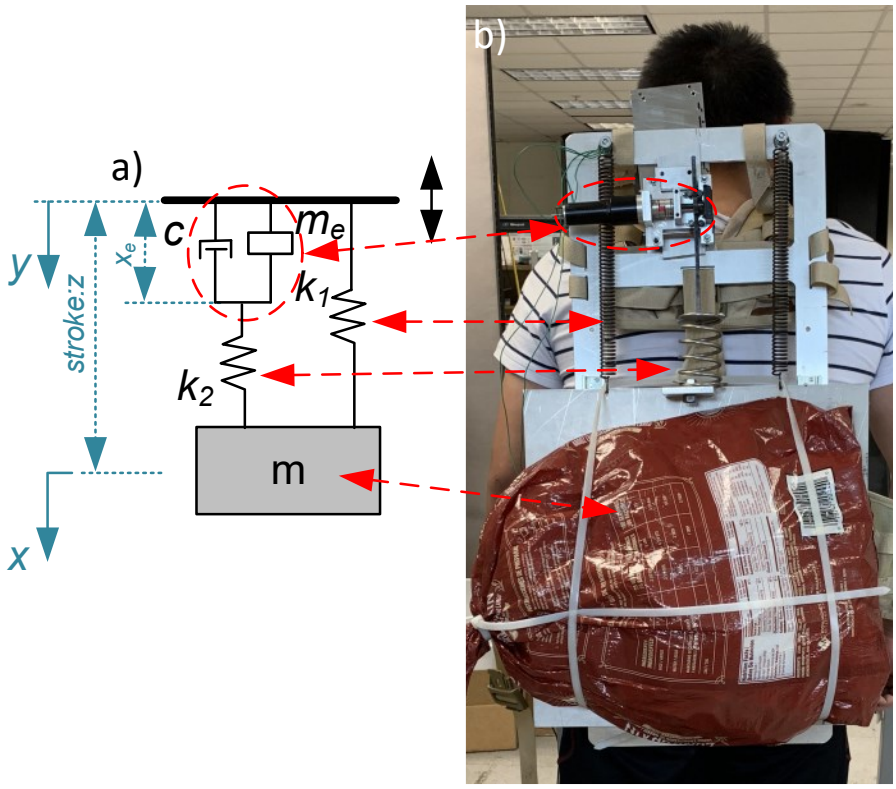


Figure 3.4: System configuration of inerter-based 2DOF energy harvesting. Spring k_2 is in series with the inerter and damping.

To illustrate how this 2DOF system can be implemented in real applications, a backpack energy harvester based on the inerter-based 2DOF system is designed and prototyped, as shown in *Figure 3.5*.

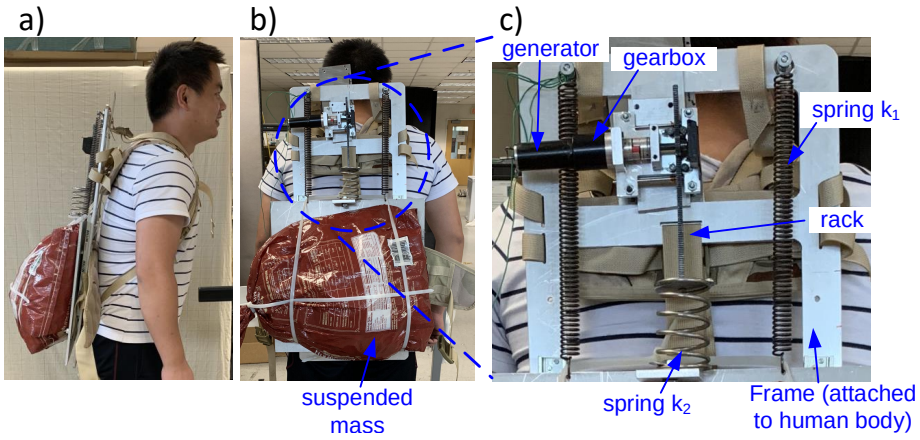


Figure 3.5: Example application of inerter-based 2DOF energy harvesting backpack. a) side view; b) back view; c) detail design.

The equations of motion are

$$\begin{cases} m\ddot{z} + k_1 z + k_2(z - x_e) = -m\ddot{y} \\ m_e\ddot{x}_e + c\dot{x}_e + k_2(x_e - z) = 0 \end{cases} \tag{3.10}$$

where $y = Ye^{j\omega t}$ is the excitation. The response can be defined as $z = Ze^{j\omega t}$ and $x_e = X_e e^{j\omega t}$. The equations in dimensionless form are

$$\begin{cases} -\gamma^2 Z + \alpha^2 Z + \beta\alpha^2 Z - \beta\alpha^2 X_e = \gamma^2 Y \\ -\mu\gamma^2 X_e + j2\xi\gamma X_e + \beta\alpha^2 X_e - \beta\alpha^2 Z = 0 \end{cases} \tag{3.11}$$

where the natural frequency of the primary system is $\omega_1 = \sqrt{\frac{k_1}{m}}$, $\beta = \frac{k_2}{k_1}$ is the spring ratio, $\mu = \frac{m_e}{m}$ is the mass ratio. The normalized excitation frequency, normalized tuning frequency, and damping ratio are $\gamma = \frac{\omega}{\omega_0}$, $\alpha = \frac{\omega_1}{\omega_0}$, $\xi = \frac{c}{2m\omega_0}$ respectively. $c = c_m + c_e$, $\xi = \xi_m + \xi_e$. The steady-state response is

$$\begin{cases} Z = \frac{\gamma^2(\alpha^2\beta - \mu\gamma^2 + j2\gamma\xi)}{(\alpha^2\beta - \mu\gamma^2 + j2\gamma\xi)(\alpha^2 + \alpha^2\beta - \gamma^2) - \alpha^4\beta^2} Y \\ X_e = \frac{\beta\alpha^2\gamma^2}{(\alpha^2\beta - \mu\gamma^2 + j2\gamma\xi)(\alpha^2 + \alpha^2\beta - \gamma^2) - \alpha^4\beta^2} Y \end{cases} \tag{3.12}$$

The nondimensionalized average electrical power output and relative displacement is

$$\begin{cases} \bar{P}_e = \frac{P_e}{m\omega_0^3 Y^2} = \frac{1}{2}\frac{c_e \dot{X}_e^{\,2}}{m\omega_0^3 Y^2} = \frac{\xi_e \beta^2 \alpha^4 \gamma^6}{[(\beta+\mu+\mu\beta)\alpha^2\gamma^2 - \mu\gamma^4 - \beta\alpha^4]^2 + 4\xi^2\gamma^2(\beta\alpha^2 + \alpha^2 - \gamma^2)^2} \\ |\bar{Z}| = \frac{|Z|}{|Y|} = \frac{\gamma^2((\alpha^2\beta - \mu\gamma^2)^2 + 4\gamma^2\xi^2)}{\sqrt{[(\beta+\mu+\mu\beta)\alpha^2\gamma^2 - \mu\gamma^4 - \beta\alpha^4]^2 + 4\xi^2\gamma^2(\beta\alpha^2 + \alpha^2 - \gamma^2)^2}} \end{cases} \tag{3.13}$$

Therefore, the system can be characterized by four independent parameters: tuning frequency ratio γ, spring ratio β, mass ratio μ, and damping ξ. At the target frequency $\gamma = 1$, the electric power output and displacement amplitude are

$$\begin{cases} \bar{P}_e(\gamma=1) = \frac{\xi_e \beta^2 \alpha^4}{[(\beta+\mu+\mu\beta)\alpha^2-\mu-\beta\alpha^4]^2+4\xi^2(\beta\alpha^2+\alpha^2-1)^2} \\ |\bar{Z}|(\gamma=1) = \frac{(\alpha^2\beta-\mu)^2+4\xi^2}{\sqrt{[(\beta+\mu+\mu\beta)\alpha^2-\mu-\beta\alpha^4]^2+4\xi^2(\beta\alpha^2+\alpha^2-1)^2}} \end{cases} \tag{3.14}$$

3.4 Analysis and optimization

The details for analysis and optimization of the four independent parameters, tuning frequency ratio γ, spring ratio β, mass ratio μ, and damping ξ_e, can be found in [6]. To obtain maximum power at stroke equals to $1/2\xi_m$, which is the same as the optimal SDOF system, the parameters are identified as α=0.62, and β=2.42. According to *Equation 15* in [6], the electrical damping ratio is 1.44. At this point, 1.3 times of power output can be obtained with the same mass oscillation stroke compared with the optimal SDOF system.

Having a broad bandwidth is also important for the energy harvesting system. The inerter-based 2DOF can have a broader bandwidth compared with the SDOF system, because there are two resonance frequencies instead of one. The frequency response of the inerter-based 2DOF system with the targeted parameters is shown in *Figure 3.6*.

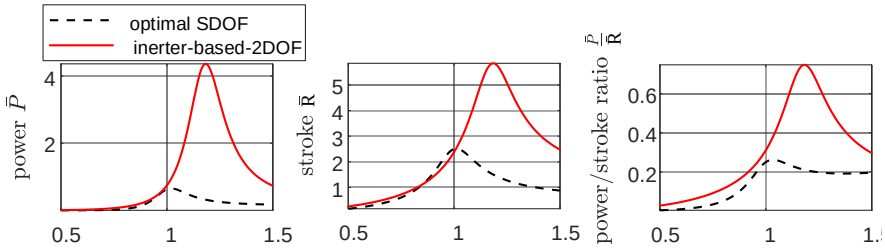


Figure 3.6: Frequency response of (a) power, (b) stroke and (c) power-to-stroke ratio. The frequency response is plotted at $\alpha = 0.62$, $\beta = 2.42$. The mass ratio $\mu = 1$ and mechanical damping ratio $\xi_m = 0.1$. SDOF system has the same mechanical damping coefficient with inerter-based 2DOF system.

As shown in *Figure 3.6*, the inerter-based 2DOF system has a larger power than, the same stroke with, and hence larger power-to-stroke ratio performance compared

with the optimal SDOF system which is tuned to have the maximum power at the target excitation frequency (see *Equation 3.4*). At the frequencies other than the target frequency, the power is also larger compared with the optimal SDOF system, as shown in *Figure 3.6(a)*. The stroke can be large or small compared with the SDOF system. However, as shown in *Figure 3.6 (c)*, the power-to-stroke ratio is much larger than the SDOF system over the entire frequency range. The two nondimensionalized natural frequencies of the 2DOF system are 0.46 and 1.58 respectively. The target excitation frequency is 1, which is between the two natural frequencies. As a result, the bandwidth of the inerter-based 2DOF system is much larger than the SDOF system. From *Figure 3.6 (a)*, it is shown that the power output of the inerter-based 2DOF in the frequency range [0.5,1.5] is much larger than that of the SDOF system.

3.5 Experiment validation

In order to validate the proposed performance of inerter-based 2DOF system, an experiment setup is designed corresponding to the model in *Figure 3.4* and is shown in *Figure 3.7*. The system parameters are shown in *Table 3.1*. The system's mechanical damping coefficient is identified by a sweep sine test, and estimated as $140Ns/m$. It is noted that two racks are shown in *Figure 3.7*. However, only one rack is connected with pinion gear and the other rack is not connected to any gear. The rack and pinion transmit linear motion to rotation motion.

A swept-sine test is done to the experiment setup. The sweep excitation starts at $0.5Hz$ and frequency increases linearly, until ends by $2.5Hz$. The target frequency ω_0 is $4\pi rad/s$, i.e. 2 Hz. The excitation amplitude is constant. The whole process lasts for a time duration of $180s$. The two resonances frequencies of the 2DOF system are $1.0Hz$ and $3.2Hz$ respectively. Although the sweep range $(0.5 - 2.5Hz)$ only covers one resonance frequency, it covers the target excitation frequency and a fair comparison can be made. The experiment does not cover higher frequency due to the limitation of the experiment setup. The large force at high frequency might damage the harvester. The experimental result is shown in *Figure 3.8* and compared with SDOF result.

As shown in *Figure 3.8*, the inerter-based 2DOF system experiment result matches pretty well with the closed-form solution. The comparison between the inerter-based 2DOF and its corresponding optimal SDOF shows that at the target frequency ($2Hz$ and $\gamma = 1$), the power and stroke is slightly larger. At the same time, the power and power-to-stroke performance of 2DOF system is better than the SDOF system over

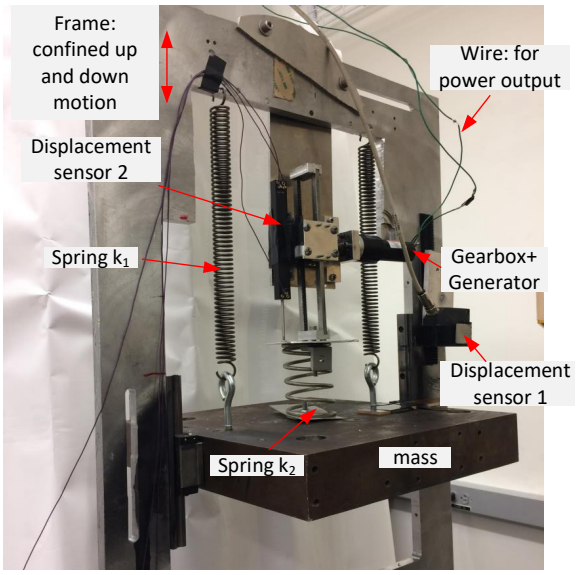


Figure 3.7: Experiment setup to validate the performance of inerter-based 2DOF system.

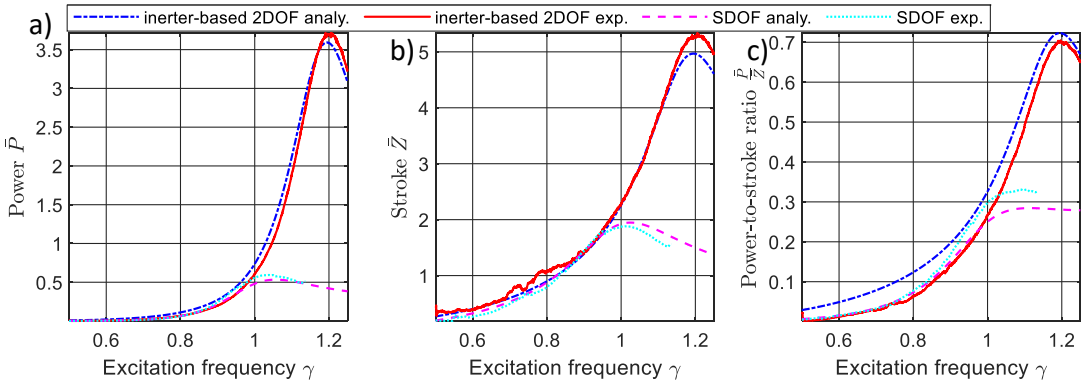


Figure 3.8: Experiment validation of inerter-based 2DOF system performance: a) power, b) stroke, c) power to stroke ratio. Details of the parameters are shown in *Table 3.1*. The SDOF system has the same topology with 2DOF system except for spring k_2. The mechanical damping coefficient of the SDOF system is the same as the 2DOF system.

Symbol	Parameter definition	Quantity
m	mass m	31.8 kg (75 $lb.$)
m_e	generator rotor, gearbox rotation equivalent mass	20.9 kg (physical mass 0.5 kg)
k_1	spring stiffness k_1	2231 N/m
k_2	spring stiffness k_2	5254 N/m
c_e	electric damping	747 Vs/m (R_L=1Ω)
n	gear ratio	33
r	radius of pinion gear	7.9 mm
R_i	internal resistance	0.4Ω
k_e	speed constant	1200 rpm/V
k_t	torque constant	7.99×10^{-3} Nm/A
α	$\alpha = \omega_1/\omega_0$	0.6665
β	$\beta = k_2/k_1$	2.0
ξ_m	mechanical damping ratio	0.13
ξ_e	electrical damping ratio	1.08

Table 3.1: System parameters of validation experiment.

the entire frequency range. This advantage is especially obvious at higher frequencies. As the inerter-based 2DOF system has the same physical mass as the counterpart SDOF system, the specific power is larger compared with the SDOF system.

3.6 Discussions

3.6.1 Force-displacement profile of inerter-based 2DOF system

The optimized inerter-based 2DOF system shown in *Figure 3.6* has large power output and the same stroke compared with the optimized SDOF system at $\gamma = 1$. Where does the extra power come from when the stroke is the same? In this section, we will plot the force-displacement loop as shown in *Figure 3.9* to show more details. The displacement is the excitation displacement input, i.e. y. The force is the force on the base, which is the sum of spring force, damper force (both the mechanical damping and electrical damping), and inerter force. The displacement is nondimensionalized with respect to the excitation amplitude Y, and the force is

nondimensionalized to body gravitational force mg.

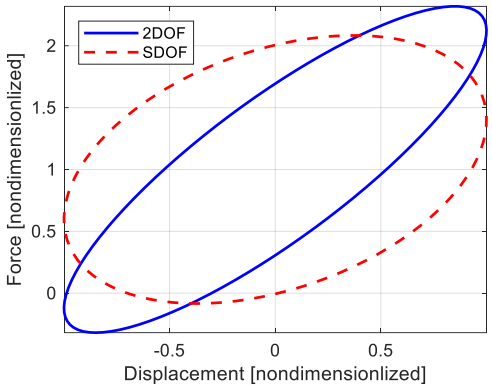


Figure 3.9: Force-displacement loop analysis of the inerter-based 2DOF system vs. the optimized SDOF system. The displacement and force are nondimensionalized to excitation amplitude Y and the human body gravitation force mg respectively. The parameter used for SDOF system and 2DOF system are the same as that used in *Figure 3.2 (b)* and *Figure 3.6* respectively

The enclosed area in the force-displacement loop is the energy input in a cycle. From *Figure 3.9*, it is shown that the inerter-based 2DOF system has a larger peak force compared with the SDOF system. By comparing both enclosed circle areas, it is found that the SDOF system's input power is larger than the inerter-based 2DOF system power. The reason is that for the SDOF system, only half of the enclosed power is converted to electrical power, as the other half is wasted as mechanical damping power. Because electrical damping is equal to mechanical damping, the power dissipated by each is equal. On the other hand, the electrical damping is much larger than the mechanical damping in the 2DOF system. With $\xi_e = 1.44$, and $\xi_m = 0.1$ for the showcase example, much less power is dissipated in mechanical damping. In this way, inerter-based 2DOF system has much better energy conversion efficiency. In systems where conversion efficiency is a concern, the inerter-based 2DOF system has advantage.

3.6.2 Influence of the mechanical damping ξ_m and mass ratio μ at the target frequency with stroke limit

The analysis in *Section 3.4* and *Section 3.5* assume the mechanical damping ratio ξ_m and mass ratio μ to be constant. In different systems, the mechanical damping ratio

ξ_m and mass ratio μ can be different. In this section, the influence of mechanical damping ratio ξ_m and mass ratio μ on energy harvesting will be analyzed. The same process outlined in *Section 3.4* is repeated with different mechanical damping ratios ξ_m and mass ratios μ. The power at the target frequency with the same stroke limit as the optimal SDOF system is shown in *Figure 3.10*.

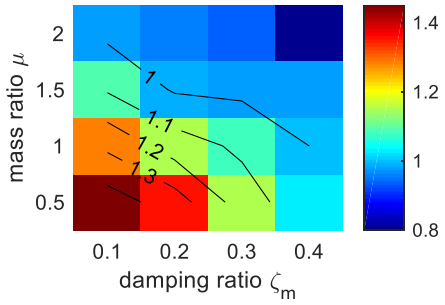


Figure 3.10: Optimal power that can be obtained from the inerter-based 2DOF system at the targeted frequency with different mechanical damping ratios ξ_m and mass ratios μ. The stroke limit is the same as the optimal SDOF system. The power output is normalized to the optimal power of the SDOF system.

When the mechanical damping ratios ξ_m and mass ratios μ are small, e.g., $\xi_m < 0.1$ and $\mu < 1$, it is shown in *Figure 3.10* that a large power can be obtained from the inerter-based 2DOF system with the same stroke limit. However, with the increase of mechanical damping ratio ξ_m and mass ratio μ, the advantage gradually disappears. This indicates that at large mechanical damping and mass ratios (for the system discussed, at $\xi_m > 0.3$,$\mu > 1.5$), the inerter-based 2DOF obtained smaller power output compared with the SDOF system. As a result, the advantage becomes a disadvantage. However, as the target frequency is still between the two resonance frequencies, the broad bandwidth feature remains.

3.6.3 Power output of the inerter-based 2DOF system at target frequency can be large by tuning the springs

From *Section 3.2* , it is found that the mechanical damping ratio ξ_m in the generator limits the maximum power of the SDOF energy harvester to be $\frac{1}{16\xi_m}$ [*Equation 3.4*]. The mechanical damping ratio is subject to the design of the energy harvesting

system, e.g. by the materials used, the mechanical design. In many situations, the mechanical damping ratios can not be reduced and becomes a constraint for the energy harvesting system. For example, the use of gearbox not only increases the power density but also increases the damping and friction in the generator. As a result, there is typically a lower bound for the mechanical damping ratio of the system. Then the power output is limited. However, as one more degree of freedom is introduced in the inerter-based 2DOF system, the larger power can be obtained from a system with the same mechanical damping ratio, by tuning the springs. As observed from Figure 7 in [6], the power ranging from 0 to large than 3 can be obtained by tuning frequency ratio α and spring ratio β. The maximum power that can be obtained at different stroke limitations is shown in *Figure 3.11*.

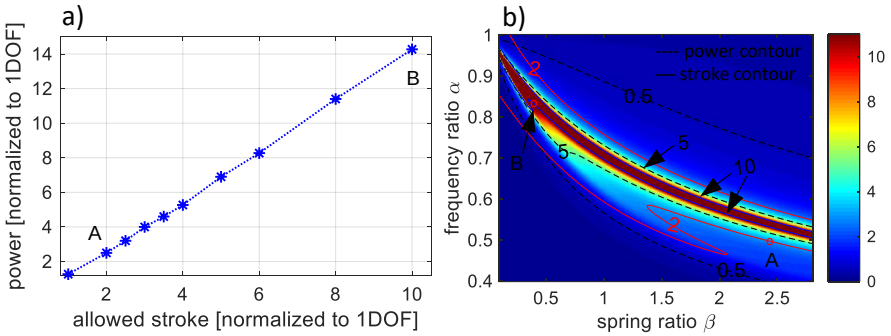


Figure 3.11: a)Power output at the target frequency increases as the allowed stroke limit increases; b) optimal power at limited stroke obtained process. The mass ratio $\mu = 1$ and mechanical damping ratio $\xi_m = 0.1$.

As shown in *Figure 3.11 a)*, the power output will increase as the allowable stroke increases. The process of obtaining optimal power at limited stroke is illustrated in *Figure 3.11 b)*. The power and stroke contour is plotted in the same figure. The maximum power at stroke limit as 2 is obtained by finding the largest power point at stroke = 2 line, and identified as point A. The same process can be done for stroke = 10 case and the point is identified as point B. The results indicate much more power can be harvested if more stroke limit is allowed. As one more degree of freedom is introduced in the inerter-based 2DOF system, the larger power output can be obtained by tuning the springs. This is a significant improvement compared with the SDOF system, where the optimal power output is strictly limited by the mechanical damping ratio in the generator.

3.6.4 Influence of mass ratio μ on bandwidth

The mass ratio is usually considered to be fixed in energy harvesting systems after the design phase. Typically, the inertance of the inerter is designed in prior by choosing different gear ratios and generators (rotational inertial). In this section, the influence of the inertance on bandwidth will be discussed to guide the design of the energy harvesting system. The performance with different inertance is compared in this section. The optimal power with different inertance is obtained in the same process as section *Section 3.4* and shown as follows. It is noted that even the optimization process is the same, the optimal values such as α, β, ξ_e are different because of different mass ratio μ

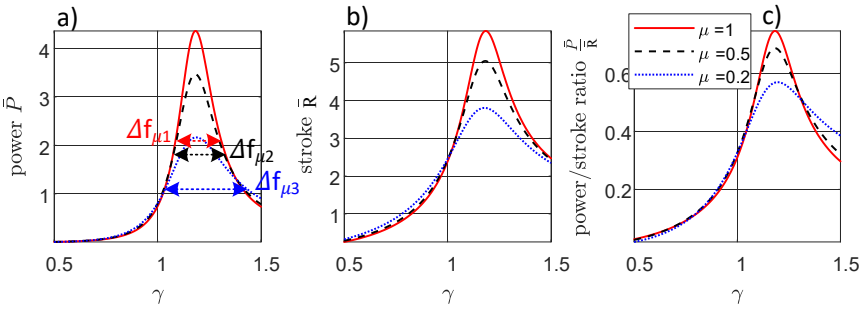


Figure 3.12: Power frequency response of the system with different mass ratios μ.

From *Figure 3.12 (a)*, it is observed that the maximum power output increases as the mass ratio increases. However, at the same time, the maximum stroke also increases, as shown in *Figure 3.12 (b)*. The abrupt change in stroke is often not welcomed in energy harvesting systems, as the physical system has to be designed to accommodate this stroke. As illustrated in *Figure 3.12 (c)*, the power-to-stroke ratio also increases due to the increase of the mass ratio. That is to say, large power is at a cost of large strokes. At the same time, large mass ratios will result in narrower bandwidths although at higher power levels. This is illustrated by the bandwidths $\Delta f_{\mu 1}$, $\Delta f_{\mu 2}$,$\Delta f_{\mu 3}$ in *Figure 3.12 (a)*.

3.6.5 Inerter-based 2DOF system vs. conventional 2DOF energy harvesting system

The inerter-based 2DOF system uses the generator rotor as an inerter to make the SDOF system a 2DOF system. This is a method that gains the benefit of the 2DOF system with neglectable extra mass to the original SDOF system. The question arises: does the inerter-based system have the same performance as the conventional 2DOF system? If not, what are the differences? In this section, the inerter-based 2DOF system will be compared with the conventional system. The modeling of inerter-based 2DOF and conventional 2DOF system is shown in *Figure 3.13*.

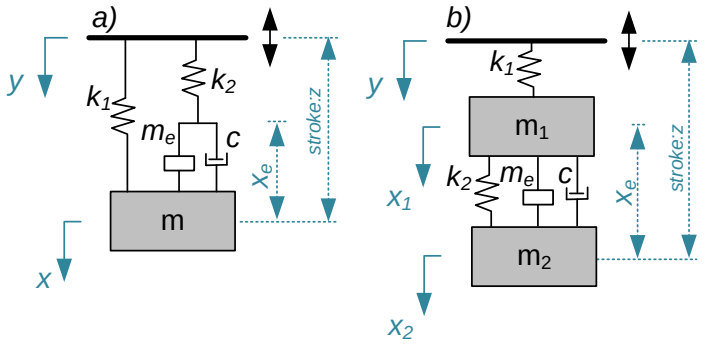


Figure 3.13: (a) Inerter-based 2DOF energy harvesting system; (b) conventional 2DOF energy harvesting system.

The equations of motion of the conventional 2DOF system are

$$\begin{cases} m_1(\ddot{y}+\ddot{z}-\ddot{x_e}) = -k_1(z-x_e)+k_2x_e+c\dot{x_e}+m_e\ddot{x_e} \\ m_2(\ddot{y}+\ddot{z}) = -k_2x_e-c\dot{x_e}-m_e\ddot{x_e} \end{cases} \tag{3.15}$$

As was done in *Section 3.4*, the same process was used to compare the performance of the conventional 2DOF system with the SDOF system, resulting in *Figure 3.14*, which is comparable to *Figure 7* in [6]. All the parameters are chosen to be the same as those used in the inerter-based system. One more mass m_2 was added and the mass ratio $\frac{m_2}{m_1}=1$. As the physical mass is m_1+m_2, the nondimensionalized power is obtained by normalizing to the total mass. The performance of the conventional 2DOF system is shown as follows.

As observed from region A and B in *Figure 3.14*, more power can be obtained at the cost of larger strokes, which is the same as the inerter-based 2DOF system.

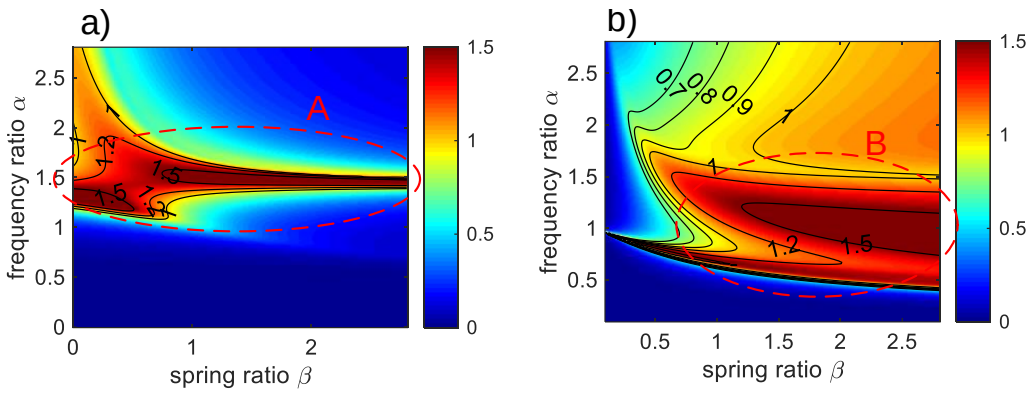


Figure 3.14: The conventional 2DOF System power-to-stroke ratio vs. tuning frequency ratio α and spring ratio β. a) conventional 2DOF system; b) inerter-based 2DOF system. All the parameters are the same as the system shown in *Figure 3.6*.

Power-to-stroke ratio larger than 1 region can also be obtained but the area is much smaller than the inerter-based 2DOF system. This indicates that the performance of the conventional 2DOF system is more sensitive to parameter changes. From the modeling and analysis, the following conclusions can be drawn from the comparison.

1. The inerter-based 2DOF energy harvesting system creates another degree of freedom based on the SDOF system by taking advantage of the inerter. In this way, only neglectable extra mass is added into the system. While in the conventional 2DOF system, a large extra mass m_2 has to be added.

2. From *Figure 3.14*, it can be observed that although the conventional 2DOF system can obtain power-to-stroke ratio larger than 1, the target spot region is relatively small. This indicates that the conventional 2DOF system is more sensitive to parameter changes.

3.6.6 Inerter-based 2DOF system vs. conventional 2DOF system

From literature, we found out that the inerter-based 2DOF system has never be proposed and its characteristics is unclear to the science community. In this section, we are going to explore more of the property of the inerter-based 2DOF system. The inerter-based 2DOF system is shown in *Figure 3.15* a). The conventional 2DOF

system is shown in *Figure 3.15* b).

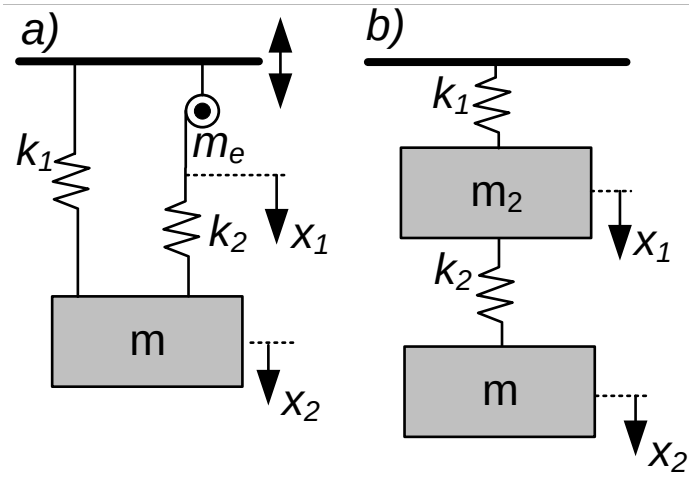


Figure 3.15: Comparison of the inerter-based 2DOF system and the conventional 2DOF system.

The EOM of the inerter-based-2DOF is

$$\begin{cases} m\ddot{x}_2 + k_1 x_2 + k_2(x_2 - x_1) = 0 \\ m_e\ddot{x}_1 - k_2(x_2 - x_1) = 0 \end{cases} \tag{3.16}$$

$$\begin{bmatrix} m & 0 \\ 0 & m_e \end{bmatrix} \begin{bmatrix} \ddot{x}_1 \\ \ddot{x}_2 \end{bmatrix} + \begin{bmatrix} k_2 & -k_2 \\ -k_2 & k_1 + k_2 \end{bmatrix} \begin{bmatrix} x_1 \\ x_2 \end{bmatrix} = \begin{bmatrix} 0 \\ 0 \end{bmatrix}$$

The characteristic equation is

$$det \begin{bmatrix} k_2 - m_e\omega^2 & -k_2 \\ -k_2 & k_1 + k_2 - m\omega^2 \end{bmatrix} = 0$$

$$(k_2 - m_e\omega^2)(k_1 + k_2 - m\omega^2) + k_2^2 = 0 \tag{3.17}$$

$$mm_e\omega^4 - \omega^2(mk_2 + m_e k_1 + m_e k_2) + k_1 k_2 + 2k_2^2 = 0 \tag{3.18}$$

On the other hand, the EOM of the conventional 2DOF is

$$\begin{cases} m\ddot{x}_2 + k_2(x_2 - x_1) = 0 \\ m_e\ddot{x}_1 + k_1 x_1 - k_2(x_2 - x_1) = 0 \end{cases} \tag{3.19}$$

$$\begin{bmatrix} m & 0 \\ 0 & m_e \end{bmatrix} \begin{bmatrix} \ddot{x}_1 \\ \ddot{x}_2 \end{bmatrix} + \begin{bmatrix} k_1 + k_2 & -k_2 \\ -k_2 & k_2 \end{bmatrix} \begin{bmatrix} x_1 \\ x_2 \end{bmatrix} = \begin{bmatrix} 0 \\ 0 \end{bmatrix}$$

In order to make fair comparison, we assume $m_2 = m_e$. The characteristic equation is

$$det \begin{bmatrix} k_1 + k_2 - m_e\omega^2 & -k_2 \\ -k_2 & k_2 - m\omega^2 \end{bmatrix} = 0$$

$$mm_e\omega^4 - \omega^2(mk_2 + mk_1 + m_ek_2) + k_1k_2 + 2k_2^2 = 0 \tag{3.20}$$

Assume those two systems have the same excitation input y. The difference in those two system is illustrated in *Figure 3.16*. The equation in blue is the equation of motion of the conventional 2DOF. The EOM of the inerter-based 2DOF system is using the conventional 2DOF EOM and move k_1 from the up-left corner to the lower-right corner.

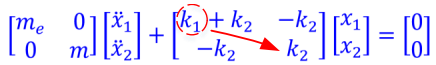


Figure 3.16: Difference comparison of the equation of motion for the conventional 2DOF system and the inerter-based 2DOF system.

The difference of those two systems can be summarized as follows.

1. If $m_e = m$, some interesting characteristic emerges. Compared with the conventional 2DOF system, the inerter-based 2DOF system will have the same set of eigenvalues and at the same time, the eigenvector swapped. That means the eigenvector of the first mass will be equal to the second mass, and the eigenvector of the second mass will be equal to the first mass. This can lead to some interesting phenomenon since a swapped eigenvector means the previous in-phase motion now become out of phase motion.

2. In terms of tuning the two resonance frequencies, there is no significant difference between the conventional 2DOF and inerter-based 2DOF system. As for both system, all parameters including m_1,m_2,k_1, and k_2 can be tuned independently.

3. Both are 2DOF system, that means both have the advantages/disadvantages of 2DOF system;

4. The inerter-based 2DOF system can have the advantage of 2DOF system with a significant less mass. As illustrated by the experiment in this dissertation, the equivalent mass m_e can be obtained with $\frac{1}{40}$ of physical mass.

5. Less space is needed for the same configuration. The inerter-based 2DOF needs base length $\frac{m}{k_1}$, while the conventional 2DOF needs a length of $m/k_1+m_2/k_1+m/k_2$.

Chapter conclusions

In this paper, we proposed an inerter-based 2DOF energy harvesting device by taking advantage of the inerter. The inerter-based 2DOF energy harvesting system was obtained by adding a spring in series with the inerter to a SDOF energy harvesting system and has the following advantages:
1. Neglectable extra mass was added to the SDOF counterpart, while the advantage of 2DOF system is obtained.
2. Larger power can be obtained compared with the SDOF counterpart with the same stroke limit. Note that from the force-displacement loop, it is clear that the large power is obtained at large force.
3. Wider bandwidth can be obtained compared with the SDOF counterpart.
4. The advantage of the inerter-based 2DOF system is more significant at small mechanical damping ratios and mass ratios.
5. Power output of the inerter-based 2DOF system at the target frequency (i.e. $\gamma = 1$) can be large by tuning the springs.
6. Compared with conventional 2DOF systems, the inerter-based 2DOF system's power-to-stroke performance is less sensitive to parameter changes.
7. The increase in mass ratio will decrease the system response bandwidth.

Chapter 4

MMR Based 2DOF Backpack Energy Harvesting System

4.1 Chapter introduction

Energy harvesting can improve system power efficiency, power distributed sensor nodes, recharge batteries, and even enable zero net energy systems [10]. Energy harvesting from the human body can power portable, mobile, and wearable systems and thus has the potential to reduce the dependence on batteries or even eliminate batteries. The energy harvesting methods from the human body [1] can be thermal [14], vibration [4][3], and foot strike [70]. Among them, vibrational energy harvesting backpack has the largest power potential [4].

Ever since the first energy harvesting backpack was introduced [4], multiple endeavors have been done or are ongoing to investigate this topic, using different energy transduction mechanisms, such as piezoelectric straps [15], linear motor [71][72], and rotational electromagnetic generator [73][74]. Among all the methods, the rotational electromagnetic generator based energy harvesting backpack has the largest power potential and highest power density. Successful research has led to commercialization, such as Lighting Pack technology ltd. Further research compared the energy harvesting solution with battery, the existing dominant power solution for electronic devices [1].

The authors introduced a linear inerter-based 2DOF system that can harvest large power at a wide frequency bandwidth [6]. The inerter is a mechanical two-node

(two-terminal), one-port device with the property that the equal and opposite force applied at the nodes is proportional to the relative acceleration between the nodes [38]. The inerter is introduced in [38] in detail. By adding one more degree of freedom to a single degree of freedom (SDOF) system, larger power, broadband width, and a larger power-to-stroke ratio was obtained [6]. However, the 2DOF system's maximum stroke in the typical working frequency range is large [6]. The frequency of the human center of mass (COM) motion is around 2 Hz [48], which is defined as ω_0 and is the target frequency of the energy harvesting backpack. The energy harvesting backpack system is tuned to perform best at the target frequency. The excitation frequency from walking generally varies between 0.5 and 1.5 times of the target frequency [75] and this range is called the working frequency range in this paper. For the case analyzed in [6], the stroke increases by 2.6 times when the excitation frequency is 1.3 times of the target frequency.

In order to address this issue, mechanical motion rectifier (MMR) based inerter nonlinearity is introduced in this paper. The MMR is a unique transduction mechanism that rectifies the bi-directional rotation into a uni-directional rotation. It has been used in many applications, such as vehicle shock absorber [76], ocean wave energy harvesting [46], railway energy harvesting [73], backpack energy harvesting [73], and shown that more power can be harvested in wider frequency bandwidth.

In this paper, we integrate the MMR with the inerter-based 2DOF system to achieve a nonlinear inerter-based 2DOF system for enhanced backpack energy harvesting performance. The nonlinear inerter will decrease the negative effect of the 2DOF harvester in the stroke magnification while keeping its advantage in increasing the power output and frequency bandwidth. The performance of the energy harvesting system is enhanced. Through modeling, simulation, and experiment, it is shown that the nonlinear inerter-based 2DOF system can reduce the maximum stroke in the working frequency range compared with the counterpart system without MMR (hereafter referred to as "linear 2DOF"). Compared with the conventional optimal SDOF system, which is used most commonly in energy harvesting systems, much larger power can be obtained with almost the same maximum stroke in the working frequency range.

The rest of this paper is organized as follows. The motivation of adding MMR to the mechanical system is presented in Section 4.2. The detailed design and modeling of nonlinear inerter-based 2DOF are introduced in Section 4.3. Analogous electrical modeling corresponding to the mechanical system is built-in Section 4.4. Optimization is done in Section 4.5 to obtain maximum power over electrical damping. System parameters are obtained with the same stroke limit as the optimal SDOF system at

the target frequency. The system performance is compared with the optimal SDOF and the linear 2DOF system. The simulation result is validated by experiment in Section 4.6. In Section 4.7, the maximum stroke is further reduced with a small compromise of power output at the target frequency. Finally the conclusions are given in Section 4.7.

4.2 Motivation of adding MMR to the system

The energy harvesting backpack excitation source can be modeled as 2 Hz, 2.5 cm amplitude sinusoidal up-and-down oscillation [77]. The single-degree-of-freedom (SDOF) energy harvesting backpack can be modeled as a conventional spring-mass-damper system. The linear inerter-based-2DOF energy harvesting backpack can be achieved by adding a spring between the transducer rack and the base, thus taking advantage of the rotational inertia of the generator rotor, and using it as a large second mass by using a small physical mass [6]. The overall lumped model is shown in *Figure 4.1*, where the excitation is $y = Y\sin(2\pi ft)$, in which the excitation amplitude $Y = 0.025m$, and the excitation frequency $f = 2Hz$. The backpack mass is m and suspension spring is k_1. The key difference compared with conventional SDOF energy harvesting backpacks is that a spring k_2 is added between the base and the transducer. The energy transducer is modeled as a damping term c in parallel with the equivalent mass of the inerter is m_e. The detailed calculation of damping c and inerter m_e can be found in [7]. As $m_e = \frac{J_e n^2}{r^2}$, large inertance can be achieved by using negligible mass by increasing gear ratio n and decreasing radius of pinion gear r. J_e is the rotational inertia of the generator rotor. Mass ratio is defined as $\mu = \frac{m_e}{m}$. The damping c consists mechanical damping c_m and electrical damping c_e. The detailed configuration is described in [6] and the nonlinear inerter-based SDOF backpack is described in [7].

The optimal performance with same stroke limit as the optimal SDOF system at target frequency is obtained and shown in *Figure 4.2* [6]. As observed from *Figure 4.2*, both the maximum power and maximum stroke in the working frequency decrease as the decrease of mass ratio μ. The reason for this phenomenon is that μ is in the denominator of both the power and stroke. As a result, increasing of μ makes the system bandwidth narrow. As the system is optimized at the same stroke (shown as point A in *Figure 4.2* b)), the narrow bandwidth makes the maximum stroke in the working frequency range large. Decreased maximum stroke is a desired feature in systems where the stroke is a concern, such as the energy harvesting backpack.

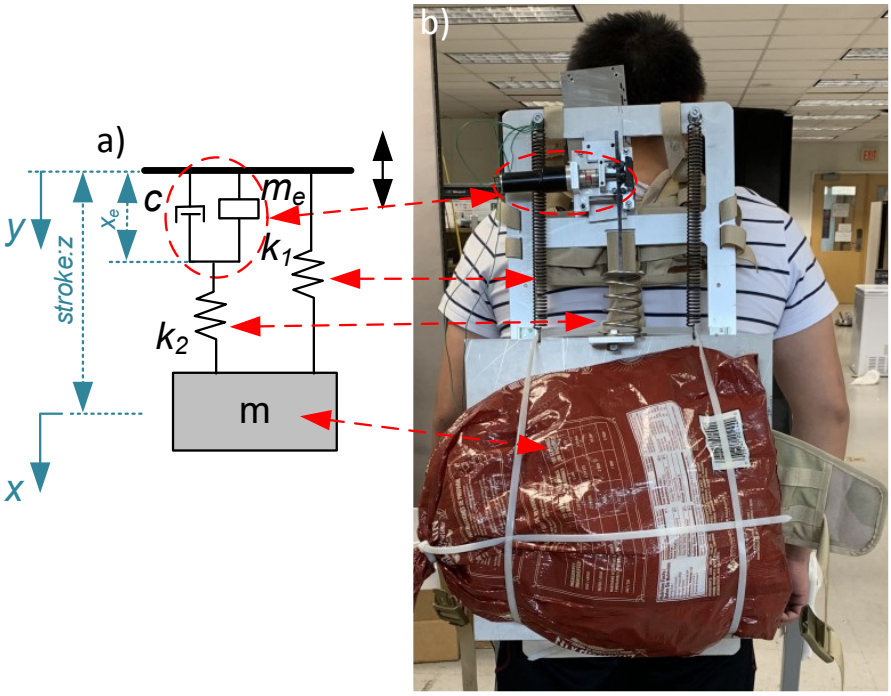


Figure 4.1: a) Inerter-based 2DOF energy harvesting system modeling. Spring k_2 is in series with the transducer [6]. b) The physical inerter-based 2DOF system.

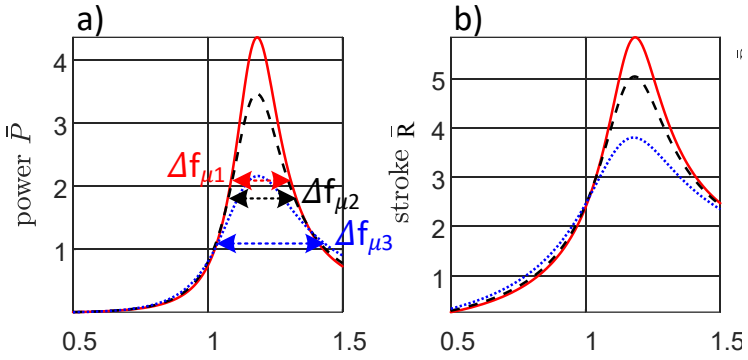


Figure 4.2: a) Power output, b) stroke frequency response of linear inerter-based system with different mass ratios μ. The power and stroke are nondimensionlized. γ is frequency ratio and $\gamma = \frac{\omega}{\omega_0}$, where ω is exciation angular velocity and ω_0 is typical human walking frequency. [6]

The maximum stroke can be reduced by reducing μ. However, gearbox with a large gear ratio has to be used to increase power density. As a result, μ is large in many applications [6].

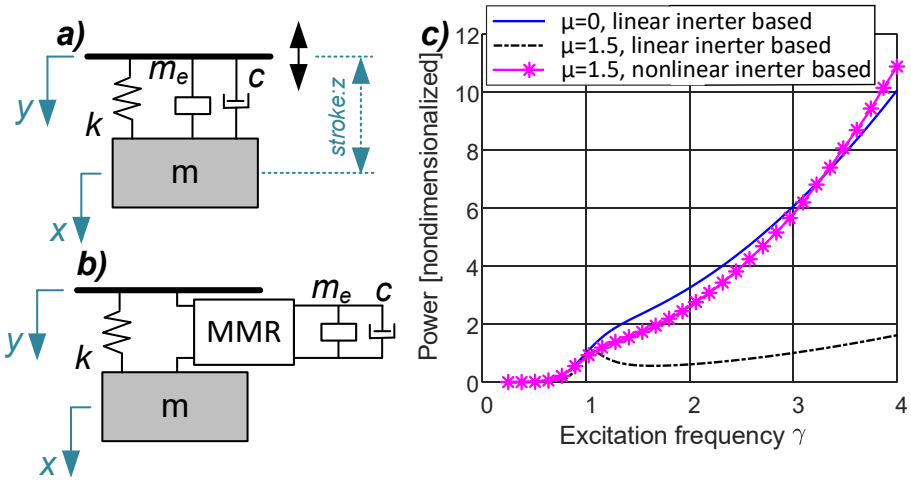


Figure 4.3: a) Linear inerter-based SDOF system b) nonlinear inerter-based SDOF system and c) comparison the power output frequency response of linear and nonlinear inerter-based system. It is observed that nolinear inerter-based system's behavior with $\mu = 1.5$ is pretty close to a system with $\mu = 0$. [7]

From literature [7]. the nonlinear inerter SDOF system performance is similar to the the system with small μ, as shown in *Figure 4.3* c). The motivation of adding MMR to the 2DOF system is to achieve performance similar to system with small mass ratio μ. In this way, the maximum stroke can be reduced.

4.3 MMR based nonlinear inerter system design

The MMR is achieved by using two one-way bearings mounted on the same shaft with engagement direction in the same direction. One design of MMR is shown in *Figure 4.4* (a). There is a one-way-bearing in each of the pinion gears. The one-way-bearing can freely rotate in one direction and lock in the other direction. Both one-way-bearings engage (lock) with the shaft in the clockwise direction and an MMR is achieved from this design. As the rack moves towards the right direction, pinion A rotates in the clockwise direction and pinion B rotates in the counter-clockwise direction. As both pinion gears engage with the shaft in the clockwise direction.

Pinion A is engaged and pinion B is not, the shaft is driven in the clockwise direction. When the rack moves towards the left direction, pinion gear B is driven to rotate in the clockwise direction and pinion gear A is driven to rotate in the counter-clockwise direction. At this time, pinion gear B is engaged and pinion gear A is not engaged. The shaft is driven in the clockwise direction. In this way, no matter how the rack drives, the shaft always rotates in the clockwise direction. The cross-sectional view of the MMR is shown in *Figure 4.4* (b). Compared with regular rack-pinion which only has one rack and one pinion, the MMR system needs two racks and two bearings. The MMR transfers two-way input to one direction rotation. For the vibration system, the difference between regular rack-pinion and MMR is the rotor of the electromagnetic generator does not have to oscillate in two directions. The rotation oscillation of the generator rotor would require more energy and force interaction between the transducer and the vibration system. As the rotor oscillates, energy flows in and out from the transducer for the kinetic energy. The energy flow results in force interactions.

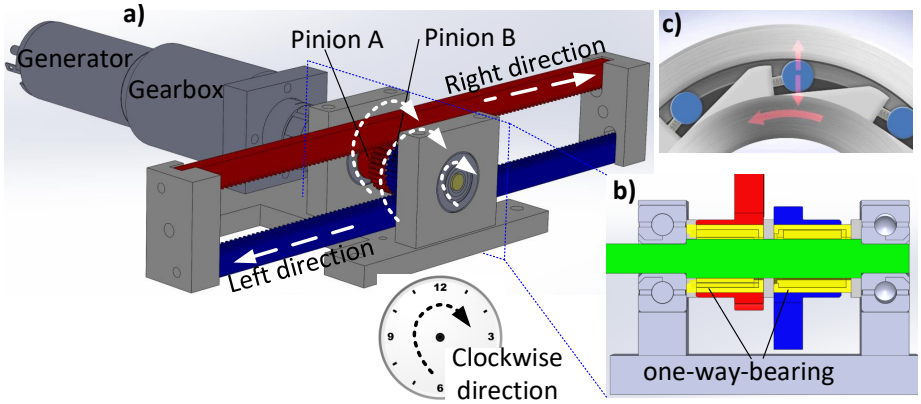


Figure 4.4: MMR design and working principle. a) overall view; b) cross-section view of MMR c) working mechanism of one-way-bearing.

The generator is rotational electromagnetic. The input motion will generate voltage output. Power is harvested by connect a resistor to the voltage output. The generator is modeled as rotational inertia term m_e and damping term c. The generator will not stop rotating due to inertia even if the input suddenly stops. When the shaft rotates with angular velocity Ω and $\Omega r > |v|$, both one-way-bearings disengages. As a result, the MMR disengages. r is the pinion radius, v is the rack velocity. The absolute value of v is used because no matter positive velocity input or negative input, the shaft always rotates in one direction. When the system is disengaged, the generator

rotor will keep rotating with the equation of motion $J_e\dot{\Omega} + c_r\Omega = 0$, where c_r is the rotational damping of the generator and gearbox and J_e is the rotational inertia of the generator rotor. This will lead to an exponential decay of Ω, i.e. $\Omega = \Omega_0 e^{-\frac{t-t_0}{\tau}}$, where Ω_0 and t_0 are the velocity and time instant when the system transits from the engaged state to the disengaged state. τ is the time constant and $\tau = \frac{J_e}{c_r}$. As a result, the overall engagement and disengagement criteria are as follows.

$$\begin{cases} \Omega = \frac{|v|}{r}, |v| \geq \Omega r, (\text{engaged}) \\ \Omega = \Omega_0 e^{-\frac{t-t_0}{\tau}}, |v| < \Omega r, (\text{disengaged}) \end{cases} \tag{4.1}$$

The engage and disengage criteria can be used to model the MMR in the nonlinear inerter-based dynamic system [7]. The lumped model of nonlinear inerter-based 2DOF energy harvesting backpack is shown in *Figure 4.5*, which is the same as inerter-based 2DOF system [6] except the use of MMR.

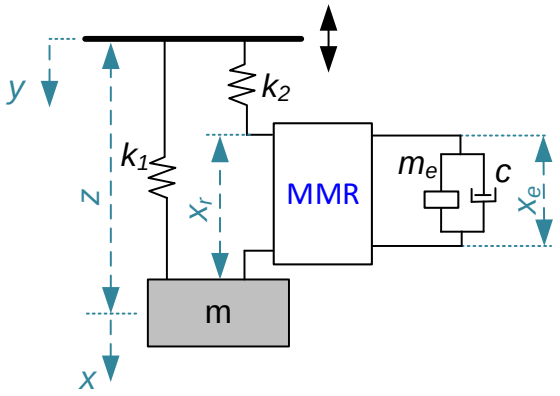


Figure 4.5: Lumped model of the nonlinear inerter-based 2DOF energy harvesting backpack.

4.4 Simulation

The mechanical system modeling is shown in *Figure 4.5*. When the MMR is engaged, the system modeling is the same as literature [6]. When the MMR is disengaged, the system becomes two independent systems. One is primary mass m and spring

k_1 with base excitation y. The other is rotational inertia equivalent mass m_e with damping c. As a result, the equations of motion is

$$\begin{cases} \begin{cases} m\ddot{z} + k_1 z + k_2 z - k_2 x_r = -m\ddot{y} \\ m_e\ddot{x}_r + c\dot{x}_r + k_2 x_r - k_2 z = 0 \quad (\text{engaged}, |\dot{x}_r| \geq \dot{x}_e) \\ \dot{x}_e = \mid \dot{x}_r \mid \end{cases} \\ \begin{cases} m\ddot{z} + k_1 z = -m\ddot{y} \\ \dot{x}_e = \dot{x}_{e0} e^{-\frac{t-t_0}{\tau}} \end{cases} \quad (\text{disengaged}, |\dot{x}_r| < \dot{x}_e) \end{cases} \tag{4.2}$$

where the relative motion of the mass $z = x - y$. The input of MMR is x_r and $\dot{x}_r = v$, where v is the rack velocity in *Eq. 4.1.* l is the natural length of the spring k_1. The equivalent linear motion of the generator rotation motion is x_e and $\dot{x}_e = \Omega r$. There are two sets of equation of motion corresponding to the engage and disengage state of the MMR. When the MMR is engaged, the equation of motion is the same as the system without MMR. Through the transmission of the MMR, output velocity $\dot{x}_e$ will be the absolute value of $\dot{x}_r$. The system's engage and disengage criteria are shown in *Eq. 4.1.* When the system is disengaged, the primary dynamic system, i.e. the mass m and spring k_1 will not interfere with the transducer. In the transducer, the equivalent mass of the generator rotor m_e will interact with the damping c_e. The equation of motion after disengage is $m_e\ddot{x}_e + c_e\dot{x}_e = 0$, which is equivalent to *Eq. 4.1* but in the terms of linear motion.

The analogous between the mechanical domain and the electrical domain with the force-current analogy is employed to analyze the equation of motion. The analogous components in the mechanical domain corresponding to the electrical domain is shown in *Table. 4.1.*

Electrical domain		Mechanical domain	
Capacitor	C,C_e	Mass	m,m_e
Resistor	$\frac{1}{R_m}$, $\frac{1}{R_e}$, $\frac{1}{R}$	Damping	c_m, c_e, c
Inductor	$\frac{1}{L_1}$, $\frac{1}{L_2}$	Spring	k_1, k_2
Voltage	V, V_r, V_e	Velocity	$\dot{z}, \dot{x}_r, \dot{x}_e$
Current	i	Force	F

Table 4.1: Analogous terms in mechanical domain and electrical domain.

With *Table. 4.1*, the mechanical system can be written in electrical domain as

$$\begin{cases} \begin{cases} C\dot{V} + \frac{\int V dt}{L_1} + \frac{\int (V - V_r) dt}{L_2} = I \\ C_e \dot{V}_r + (\frac{1}{R_m} + \frac{1}{R_e}) V_r - \frac{\int (V - V_r) dt}{L_2} = 0 \\ V_e = \mid V_r \mid \end{cases} & (\text{engaged}, |V_r| \geq |V_e|) \\ \begin{cases} C\dot{V} + \frac{\int V dt}{L_1} = I \\ V_e = V_{e0} e^{-\frac{t - t_0}{\tau}} \end{cases} & (\text{disengaged}, |V_r| < |V_e|) \end{cases}$$

In order to derive the analogous electrical domain representation, the current source I is set to be equal to $-mY\omega^2 \sin(\omega t)$. As the electrical system is analogous to mechanical system, the time constant τ can be also defined as $\tau = \frac{m_e}{c_m + c_e} = C_e(R_m + R_e)$. The time constant τ is the same for mechanical system and electrical system. The MMR can be represented by a center tapped full wave rectifier in the electrical domain. The engage and disengage of the MMR is determined by velocity input $\dot{x}_r$ and output $\dot{x}_e$. Correspondingly, the on and off state is determined by the input voltage V_r and output voltage V_e in electrical domain. With the analogous equation of motion, the analogous electrical model can be built, as shown in *Figure 4.6*. With commercial available software such as Simulink, the simulation can be done.

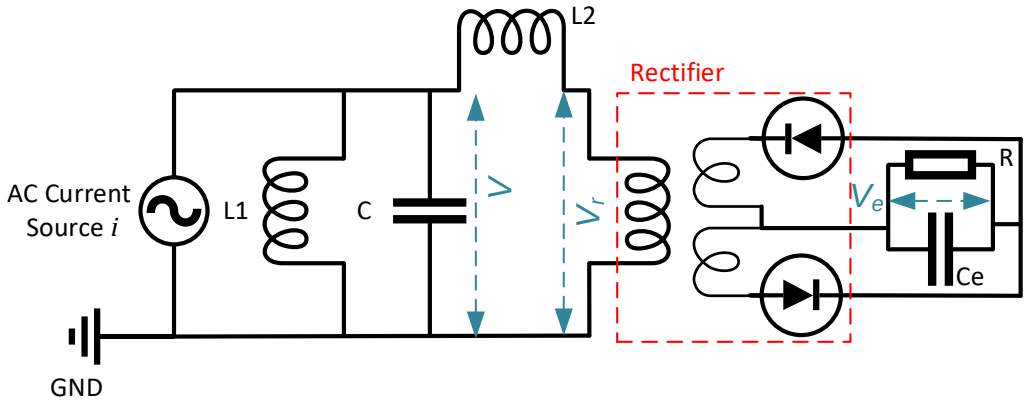


Figure 4.6: Analogous electrical circuit to represent the mechanical modeling.

With excitation input as 2.5 cm, 2 Hz sinusoidal base excitation, the output is shown in *Figure 4.7*. To parameterize the system, nondimensionalization is done. Frequency ratio $\bar{k_1} = \frac{\omega_1}{\omega_0}$, where ω_1 is the natural frequency of the primary system and calculated by $\omega_1 = \sqrt{\frac{k_1}{m_1}}$. ω_0 is the primary excitation angular frequency. For the backpack energy harvester, the primary excitation frequency is the human walking frequency, which is around 2 Hz. Spring ratio $\bar{k_2} = \frac{k_2}{k_1}$. The mechanical and electric

damping ratio are $\xi_m = \frac{c_m}{2m_1\omega_0}$ and $\xi_e = \frac{c_e}{2m_1\omega_0}$. respectively. As the springs are tuned in the optimization part, they will change and thus not an intrinsic property of the system anymore. As a result, the damping ratio is optimized by primary excitation angular frequency, which is constant throughout the analysis. As a result of the center-tapped full wave rectifier, V_e is always positive. According to the analogy between the mechanical domain and the electrical domain, V_r and V_e corresponding to the input and output velocity of the MMR, i.e. $\dot{x}_r$ and $\dot{x}_e$.

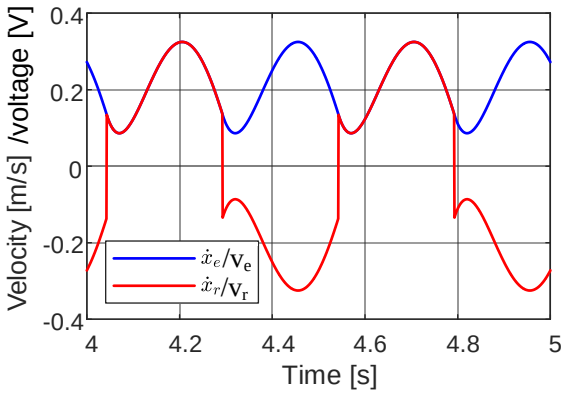


Figure 4.7: Time domain simulation result of input voltage $\dot{x}_r$ and output voltage $\dot{x}_e$ of the rectifier bridge in electric domain. This corresponds to the input velocity and output velocity of the MMR in mechanical domain. Simulation result is obtained with $\bar{k_1} = 0.66$, $\bar{k_2} = 2.3$, $\xi_m = 0.13$, $\xi_e = 0.63$, and $\gamma = 1$.

This is the modeling basis for the optimization and performance analysis in the following sections.

4.5 Optimization

As the nonlinear inerter-based 2DOF system engages and disengages, there is no closed-form solution for optimal electrical damping. A numerical search method, i.e. golden-section search method [78], was introduced to obtain the optimal electrical damping. The power output at both zero electric damping and infinite electric damping are low and from simulations it is found that only one peak exist in the power-electrical damping curve. The golden-section search can be used to find the optimal power output point. The golden-section search method requires relative small computation power to find the optimal point. The process of the golden-section

search is shown in *Figure 4.8*, where points 1∼10 are the points search between damping ratio $\xi_e \in [0, 5]$ range. The search stops when the maximum power is reached at point 10. The criteria for the stop of searching is when the difference between the last point and the second last point is less than 2%.

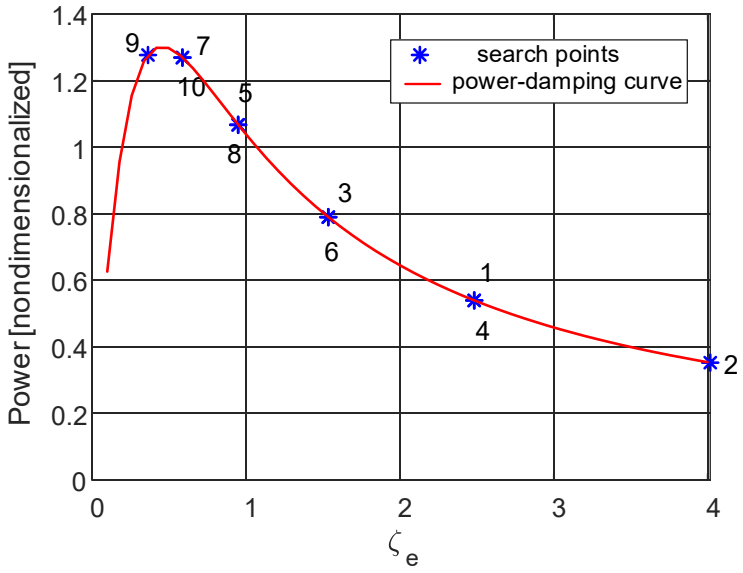


Figure 4.8: Search process of golden-section search method. The results are obtained with $\bar{k_1} = 0.7$, and $\bar{k_2} = 2.5$, $\xi_m = 0.13$, and $\gamma = 1$.

With the optimal electrical damping identified, the power, stroke, power-to-stroke ratio is obtained in the parameter range, i.e. frequency ratio $\bar{k_1}$, and spring ratio $\bar{k_2}$. The result is shown in *Figure 4.9*. The nondimensionalized optimal power output and corresponding stroke for SDOF system is $\frac{1}{16\xi_m}$ and $\frac{1}{4\xi_m}$ by the frequency matching and frequency matching method [6]. The a) power, b) stroke in *Figure 4.9* are normalized to the optimal performance of SDOF system.

It is found that large power can be obtained with large stroke, as illustrated in area A in *Figure 4.9* a) and area B in Figure *Figure 4.9* b). Large power-to-stroke ratio can be identified in area C in *Figure 4.9* c). The result is very similar to the contour result obtained in [6]. With the same stroke as the optimal SDOF system, optimal power point can be identified from the power and stroke contour. With the performance over all the reasonable spring and damping ratios, and with stroke limit to 1, the optimal power output can be identified as the target point in *Figure 4.10*. The stroke equal to 1 means that the stroke is the same as the optimal SDOF

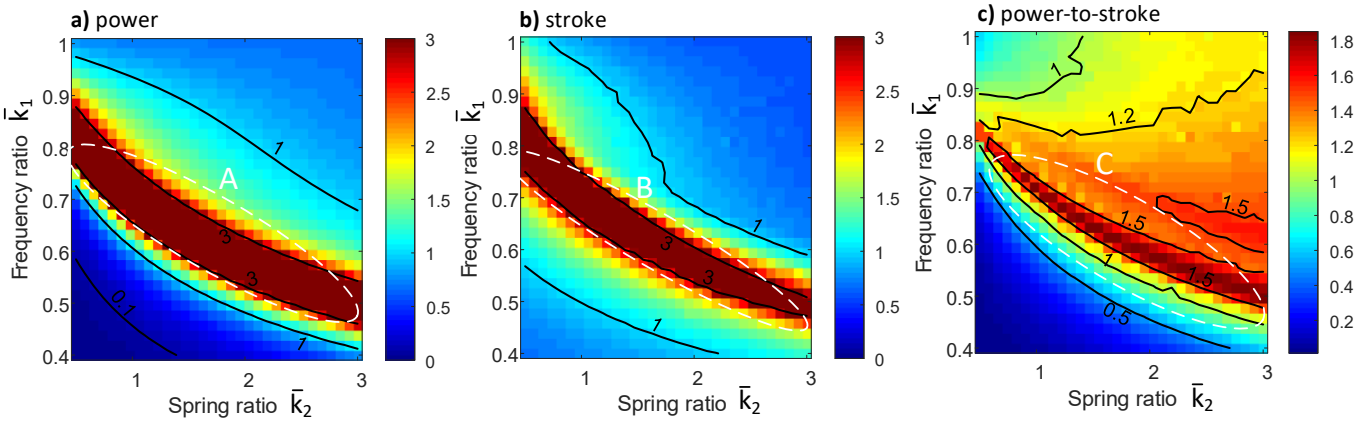


Figure 4.9: a) Power, b) stroke, and c) power-to-stroke ratio over different frequency ratio $\bar{k_1}$ and spring ratio $\bar{k_2}$. All values are normalized to the optimal performance of SDOF system.

system. The spring parameters are identified as $\bar{k_1} = 0.66, \bar{k_2} = 2.3$. It is found that the power output can be 1.5 times the optimal SDOF system with the same stroke limit. It is noted that the stroke contour lines are not smooth due to the numerical simulation issue. A smoother result can be obtained by increasing the contour density but at the expense of computation power. The contour plot here is reasonable with 30×30 point contour grid.

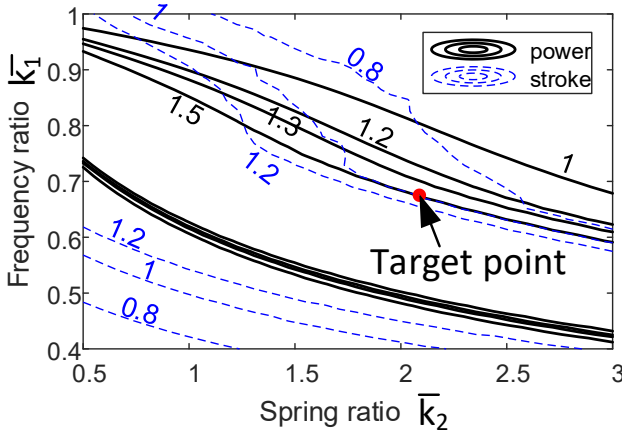


Figure 4.10: Optimal power identification with stroke limit the same as the optimal SDOF system.

After the optimal point is obtained, the frequency response of power and stroke are

plot in *Figure 4.11*. From *Figure 4.11*, it is shown that compared with 2DOF system without MMR, the stroke at high frequency decreases as a result of MMR. The maximum nondimensionalized stroke of the linear 2DOF system in the $\gamma \in [0.5, 1.5]$ frequency range is 4.4. While with MMR, the maximum stroke is 3, which is a 32% decrease compared with the previous. The MMR can help the system reduce maximum stroke in the working frequency range. The nonlinear inerter base system is more practical in real applications compared with the linear inerter-based 2DOF system. It is noted that the power output also decreased as a result of MMR, which is 3.4 for linear inerter-based 2DOF system and 2.2 for nonlinear inerter-based 2DOF system. However, for applications such as energy harvesting backpack, a large stroke makes it almost impossible to walk. It is critical to decrease the stroke.

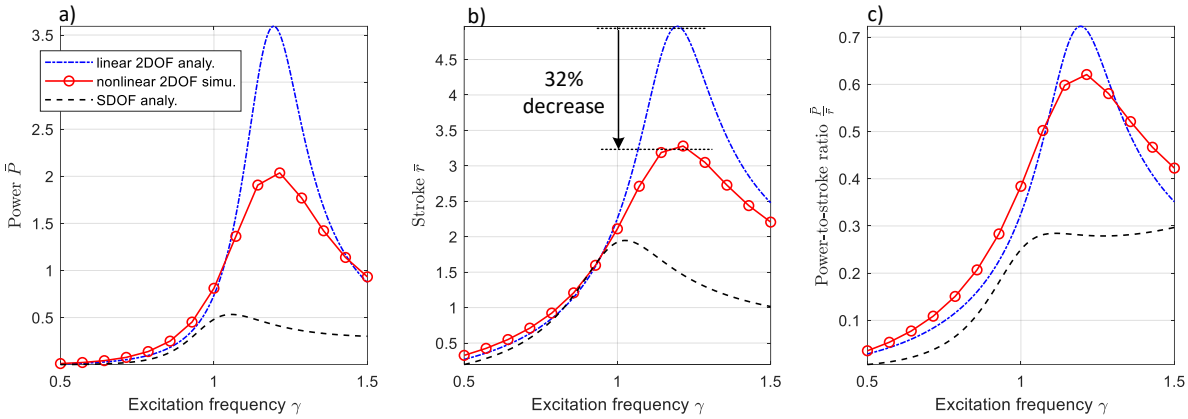


Figure 4.11: a) Power, b) stroke, and c) power-to-stroke ratio frequency response of the nonlinear inerter-based system compared with the linear inerter-based system and the optimal SDOF system. The system parameters are $\bar{k_1} = 0.66, \bar{k_2} = 2.3$ for both nonlinear and linear case. $\xi_e = 0.61$ for nonlinear inerter-based system and $\xi_e = 1.08$ for linear inerter-based system case. Both damping ratios are close to optimal value.

4.6 Experiment validation

In order to validate the simulation result, experiment is done with sinusoidal base excitation. The experiment setup is shown in *Figure 4.12*, which is corresponding to the lumped model shown in *Figure 4.5* and *Eq. 3.10*. Base excitation is provided by Instron 8800.

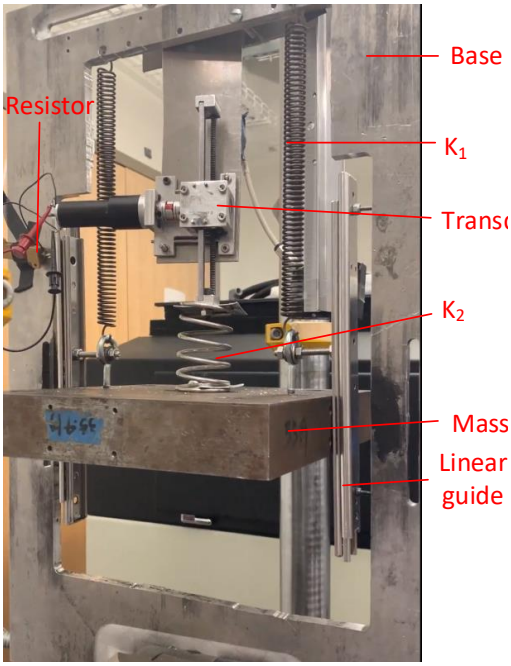


Figure 4.12: Experiment setup.

The experiment parameters are shown in *Table.* 4.2. It is noted that the experiment system parameters do not match 100% with the optimization results, as a result of limitation of the commercial available springs and resistors. However, the largest error is less than 13%.

Parameter	Quantity	Explanation
m	31.6 kg	Mass
m_e	20.9 kg	Equivalent mass of generator
k_1	2217 N/m	Spring k_1
k_2	4433 N/m	Spring k_2
c_m	100 Ns/m	Mechanical damping
c_e	463 Ns/m	Electrical damping
ξ_m	0.13	Mechanical damping ratio
ξ_e	0.58 (0.63)	Electrical damping ratio
$\bar{k_1}$	0.67 (0.66)	Frequency ratio $\bar{k_1} = \frac{\omega_1}{\omega_0}$
$\bar{k_2}$	2 (2.3)	Spring ratio $\bar{k_2} = \frac{k_2}{k_1}$

Table 4.2: Experiment parameters. (The quantity in the bracket is the theoretical optimal value.)

The excitation input from Instron is $y = Y\sin[4\pi(0.5 + \frac{t}{180})t]$, where t is time. t starts at 0 s and ends in 360 s. This makes the base excitation as constant amplitude input with linearly increased frequency starts at 0.5 Hz at 0 s and ends at 2.5 Hz at 360 s. The frequency range is $\gamma = [0.5, 1.25]$ as the target excitation frequency is 2 Hz. The reason for not using higher frequency as input is due to the limitation of the experiment setup, e.g., huge force at high-frequency excitation is out of the limitation of the bearings. The experiment result is shown in *Figure 4.13*.

From *Figure 4.13*, it is shown that the experiment result matches well with the simulation result in general, for both the optimal SDOF system, linear inerter-based 2DOF system (referred as "linear 2DOF"), and nonlinear inerter-based 2DOF system (referred as "nonlinear 2DOF"). The mismatch can be from multiple possible sources. One very likely but to be verified reason is the simplified model for the damping and friction in the gearbox and generator. Only damping is considered, but in reality, the model is more complicated. Nevertheless, the trend of the nonlinear inerter-based system experiment matches well with the simulation. The maximum stroke in the $\gamma = [0.5, 1.25]$ range decreases from 5.3 for the linear inerter-based system to 4 for the nonlinear inerter-based system.

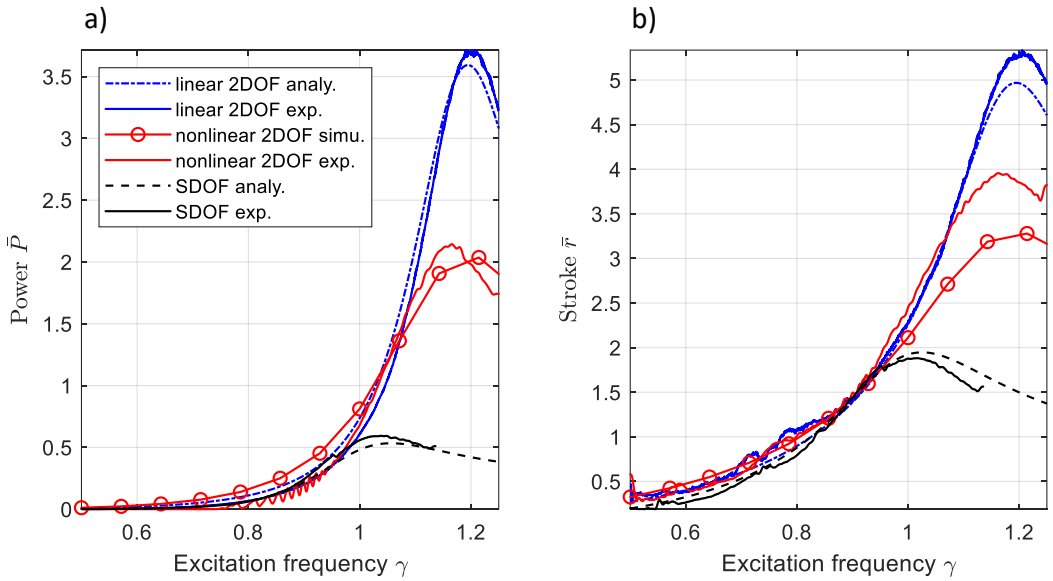


Figure 4.13: Experiment results of the nonlinear and linear inerter-based system vs. simulation results. a) power output; b) stroke.

4.7 Discussion

From *Figure 4.11*, one can find that the MMR reduces the maximum stroke by 32%. The maximum stroke problem is addressed to some extent. However, compared with the SDOF system, the maximum stroke increased by 60%. The question arises: what kind of performance can the nonlinear inerter-based 2DOF have if the stroke limit is the same stroke limitation of the SDOF system over the entire working frequency range? The optimal electrical damping ξ_e is obtained by the golden-section search method. Through simulation, it is found that the power decreases as a decrease or increase of electric damping ξ_e at the target excitation frequency. However, the power is not sensitive to electric damping change around the optimal power point. As illustrated in *Figure 4.14*, 80% of the optimal power can be obtained within [0.5, 2.2] times of the optimal electric damping for linear inerter 2DOF system and [0.33, 2.5] times for nonlinear inerter 2DOF system. In other words, the optimal power at the target frequency is not sensitive to the electric damping ξ_e changes.

Through simulation, it is also found that the maximum stroke in the working frequency range can be reduced as a decrease of electric damping ξ_e. One example to illustrate is shown in *Figure 4.15* and denotes as "nonlinear 2DOF simu sd.".

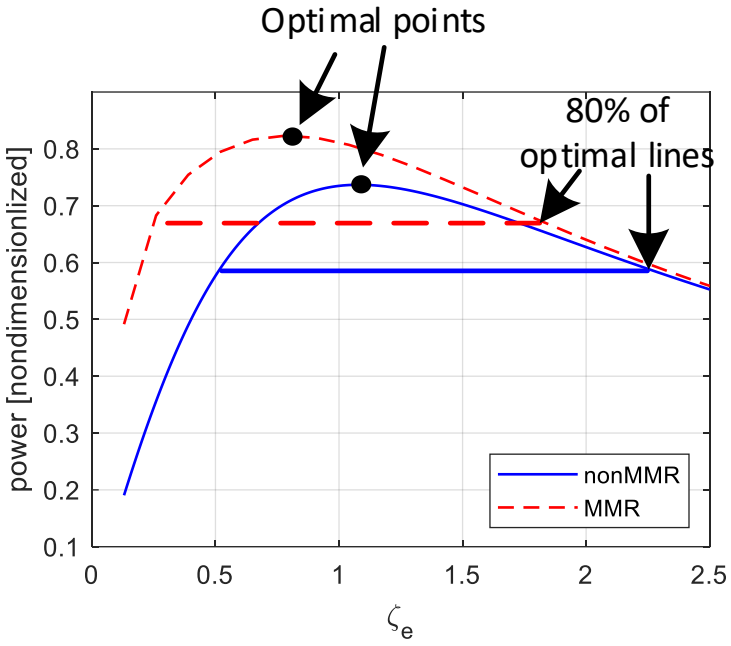


Figure 4.14: Power trend with respect to electric damping ξ_e

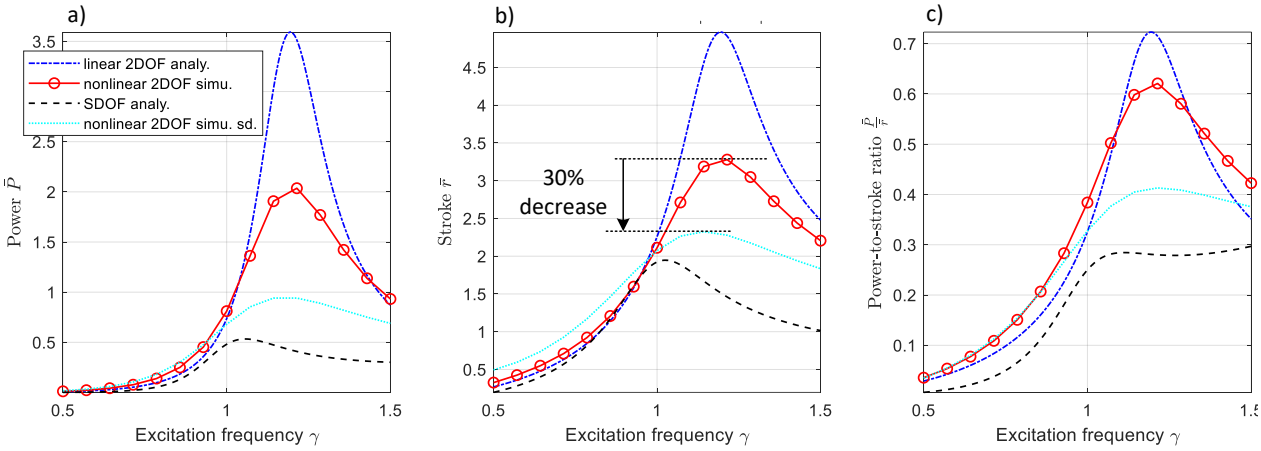


Figure 4.15: Simulation results of nonlinear inerter-based 2DOF system. a) power, b) stroke, c) power-to-stroke ratio frequency response. "sd." denotes small electric damping case. The parameters for small damping nonlinear inerter-based system is $\bar{k_1} = 0.66, \bar{k_2} = 2.3, \xi_e = 0.26$. The nonlinear inerter-based 2DOF system has $\xi_e = 0.58$. The parameters for the other cases can be found in *Figure 4.11*.

From *Figure 4.15* , it is found that the maximum stroke in the working frequency range reduces 30% (from 3.3 to 2.3) compared with the nonlinear inerter-based system obtained in *Figure 4.11*. This is achieved with only 16% power reduction in the target frequency. It is true that the maximum power is reduced as a result of stroke reduction. For the backpack application, the large stroke problem is more urgent. The maximum stroke is reduced to close to the SDOF system (20% difference). Compared with linear inerter-based system and the nonlinear inerter-based large damping case, the small damping case has the largest bandwidth. At the same time, the overall power output performance is much better than the SDOF system (as illustrated in *Figure 4.15* a)). Both the maximum power and the bandwidth increased compared with the SDOF system. The simulation was also validated by experiment and shown in *Figure 4.16* .

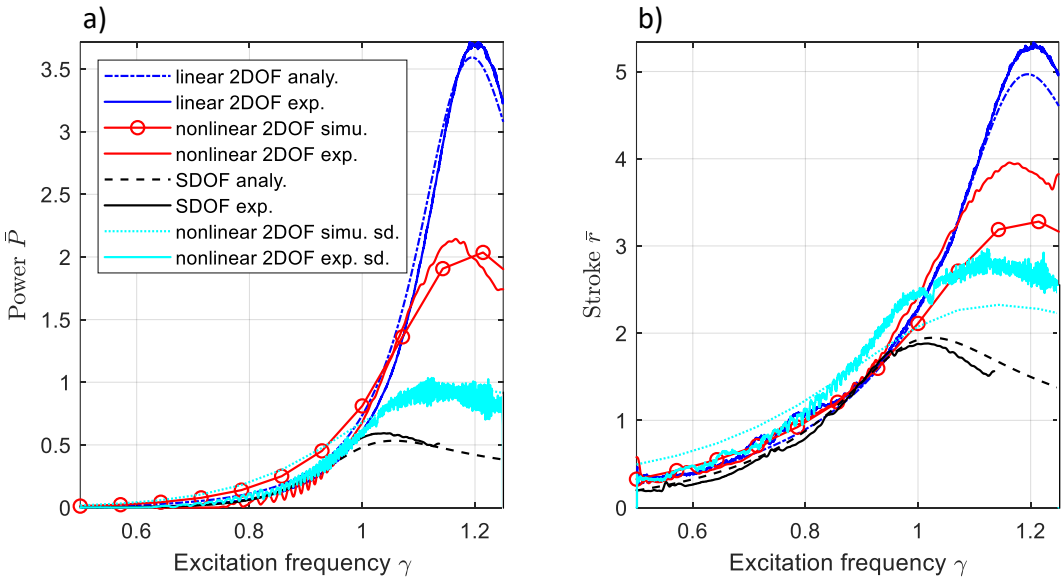


Figure 4.16: Experiment validation for the small stroke case.

Chapter conclusions

Stroke is an issue in many energy harvesting systems. The maximum stroke in linear inerter-based 2DOF system is large due to inerter. In this paper, a nonlinear inerter-based 2DOF energy harvesting system is introduced by using mechanical motion rectifier (MMR). System performance is analyzed after optimization and validated

by experiment. Results show that nonlinear inerter-based 2DOF system can decrease maximum stroke in the working frequency range by 32% compared with the linear inerter-based 2DOF system. The maximum stroke can be further reduced with small electric damping. As the stroke decreases, the bandwidth also increases. Even though the power decreases compared with linear 2DOF system as the decrease of stroke, the nonlinear inerter-based 2DOF system can have larger power over the entire working frequency range compared with the optimal SDOF system.

Chapter 5

Negative Muscle Work Energy Harvester

5.1 Chapter introduction

Wearable and mobile electronic devices such as smartphones, smartwatches, GPS, activity trackers, and computers, are playing an increasingly important role in our daily life. Almost all of these devices are powered by batteries. However, the limited life span of batteries constitutes a critical limitation, especially during long-term expeditions where an electrical power supply cannot be conveniently accessed. Batteries add considerable weight to carry. For example, U.S. soldiers carry 7.3 kg (16 lbs.) of batteries in Afghanistan for a 72-hour mission. While most digital technologies progress at a fast pace, battery technology still lags far behind [79]. Moreover, the current trends show that the limitation of batteries will continue to be an issue in the near future [80]. The human body stores a huge amount of energy. On average, there is 384 MJ of energy in the form of fat in a person, which is equal to a 600-kg lithium-ion battery (with a specific energy 0.6 MJ/kg) [79] [12]. The human metabolic cost in quiet standing is around 128W [79], while daily activities such as walking and running can consume up to several hundred or even thousands of watts [12]. While on the other hand, the power consumption of most mobile electronic devices ranges from milliwatts to a few watts. If only a small fraction of this power could be harvested, it would be enough to power most of the wearable and mobile devices. Energy harvesting from human motion is a promising solution, especially as the power consumption of those devices continues to decrease due to technology

development [81] [11].

The average human consumes 80-360 W of power while walking at 1.8-7.2 km/h (1-4.5 mph) [13]. Most of this energy is dissipated as heat [8] and about of the energy is converted to mechanical energy. When walking on level ground and at a constant speed, the kinetic and potential energy in the human body will not increase between walking cycles, i.e. the potential and kinetic energy will remain the same at the beginning and end of each cycle. Winter [8] defines negative and positive muscle work as follows: Negative work is the work done during an eccentric contraction when the muscle moment acts in the opposite direction to the movement of the joint. On the contrary, positive work is the work done during a concentric contraction when the muscle moment acts in the same direction as the angular velocity of the joint. As the kinetic and potential energy does not change from cycle to cycle, the positive muscle work has to be counteracted by negative muscle work and the power dissipation in the human body. For every watt of positive work done, the muscle does 0.7 watts of negative work, and 0.3 watts of power is dissipated [19]. Both positive work and negative work require positive metabolic energy [20].

To date, various devices have been invented to harvest energy from the human body in the form of mechanical [4] and thermal energy [14]. Review papers on human body energy harvesting can be found in [12] [1] [82]. Among energy sources from the human body, mechanical energy provides the largest amount of power and has the potential to power wearable and mobile devices [20]. Mechanical energy harvesting devices can harvest energy from muscles (such as hand-cranked generator), the motion of joints (such as ankle, knee, hip, arm, and elbow), and motion of the center of gravity (such as backpack energy harvester). Mechanical human body energy harvesting can also use different transducers, such as triboelectric [83], piezoelectric [84], electrostatic [85], and electromagnetic [4]. Among them, the electromagnetic energy harvester has the largest power output and best efficiency [4] [82] and is widely used in human body energy harvesting systems [20] [84].

In terms of positive work and negative work, mechanical energy harvesting devices can be categorized into four subsets: negative work energy harvesters, positive work energy harvesters, harvesters that harvest both positive and negative work, and impact energy harvesters (dissipated energy). Negative work energy harvesting devices harvest energy while the muscle is doing negative work. The energy harvesting process has the potential to reduce the metabolic cost to the wearer by assisting the

muscle in doing negative work. This device category includes the knee energy harvester by Donelan *et al.* [3] and the ankle energy harvester by Collins *et al.* [2]. Harvesting negative work not only generates electricity, but also could potentially decrease muscle work. As a result, the cost of harvesting (defined as additional metabolic power in watts required generating 1 W of electrical power [3]]) using this method is low. Positive energy harvesting devices harvest energy when the muscle outputs positive work. Examples of these devices can be found in many commercially available devices, such as manually cranked electronics, wind-up flashlights, hand-cranked generator, and the self-powered wireless button [86], energy harvesting keyboard [87]. Another category is devices that can harvest both positive and negative work at the same time, which includes the energy harvesting backpack [4]. The last category is energy harvesting from impact. For example, energy is dissipated in the human leg at the heel strike [3]. Multiple devices were invented to harvest this otherwise dissipated energy, such as shoe energy harvesters [83], artificial feet [88], and energy harvesting tiles [54] [89].

Commercially available energy harvesting devices such as hand-crank generators are not an ideal solution for two reasons. First, energy harvesting requires positive muscle work, which means that the energy harvested comes from metabolic power. Rather than harvesting positive muscle work, a better method is to harvest negative work, such as with the knee energy harvester by Donelan *et al.* [3]. Second, the users have to focus their attention on energy harvesting. For example, while cranking the generator, the user cannot conduct other activities, such as text messages or surf the Internet. An ideal method is to harvest energy from everyday activities with little or no interference on the natural functions of the human body, such as with the backpack energy harvesters [4]. The ankle joint has been interest for energy harvesting [**?**][95]. However, they all share one or several of the following problems: cumbersome, limits ankle motion, perturbs gait, heavy.

From literature, it is clear that the calf muscles do negative muscle work during the terminal stance phase. The goal of energy harvester design in this paper is to harvest that negative muscle work, while at the same time, does not influence the normal human gait. Several attempts have been published [**?**][95], however, the performance is still not satisfying in terms of the amount of power harvested, the model of the harvester is not clear, the design criteria is not clear.

Inspired by the positive and negative energy expenditure insight [8] [19], one can hypothesize that if the negative work done by human muscles can be replaced partially

by a regenerative device (similar to regenerative brake in vehicles), energy can be harvested while assisting human motion. To harvest negative work from the human body, an ankle energy harvester is proposed and prototyped in this paper. A rotatory generator is attached alongside the shank without any modification to the shoe or the body, and is driven by ankle motion during walking. The simple design a frame and a generator makes sure only negative work is harvested from human walking while making fabrication and application of this device convenient. The lightweight design (100 g / 0.22 lbs.) aims to have a minimal effect on natural human gait and metabolic cost. Experiment studies show that 0.30.05W of power was harvested during 4.8 km/h walking. The device is shown to harvest energy only during the negative work phase, so it has the potential to not increase the metabolic cost. The torque generated by the energy harvester is in the same direction as the gastrocnemius muscle, thus it is trying to assist the muscle doing negative work. The energy harvesting modeling and the parameter choice criteria are built. The design concerns raised, such as harvest weight, working phase, constraint to the walking gait, are addressed. This energy harvester has huge potential applications in powering wearable and mobile electronic devices. The design process and design considerations can be applied to ankle energy harvesters and other human body energy harvesters alike.

The rest of this paper is organized as follows. Section 2 will present human body dynamics, with a focus on the dynamics of the ankle and the negative work phase of gait. The design of the ankle energy-harvesting device will be presented in Section 3. The design ensures that only negative work is harvested during human walking. System parameters are identified, and system modeling is described in Section 4. Experiment validation during treadmill walking will be presented in Section 5. Discussion and conclusions will be given in Section 6 and Section 7 respectively.

5.2 Negative work in the ankle during human walking

Understanding human walking kinematics and kinetics is a prerequisite for designing a human body energy harvester. Humans walk through a complex orchestration of muscle forces, joint motions, and neural motor commands [90]. Through millions of years of evolution, the walking pattern is optimized such that metabolic cost is minimized [2]. A simplified model of walking can be described as an inverted pendulum

[90]. The power dissipated by friction in joints during walking is negligible compared to the power required for walking [18]. During steady speed walking on level ground, the kinetic and potential energy does not change when comparing the start and end of a cycle. Based on the inverted pendulum model, the positive work done by the muscles is dissipated by negative muscle work and damping in the human body. The negative and positive work from the lower extremity joints in human walking has been previously described in the literature [1] [19].

Typical human walking results in approximately 5 cm of center of mass (COM) vertical motion during each gait cycle [77]. According to the inverted pendulum model [90], human walking is illustrated in *Figure 5.1.* The terminal stance is defined as the time from heel rise until the other limb contacts the floor [91]. In the terminal stance, the COM follows a trajectory of an arc with the pivot at the standing ankle. In the vertical direction, the COM goes down by $\Delta h = 5cm$ during the terminal stance. The gravitational potential energy change during terminal stance can be approximated as

$$W = mg\Delta h \tag{5.1}$$

where m is the mass of the human body and g is the gravitational constant. Assuming an average human weight of 70 kg [92], and the average human walking frequency as 1 Hz, i.e. two steps per second [48], the potential energy change is $35J$, and the power rate of potential energy is $70W$. This potential energy is then transmitted into three parts at the end of the terminal stance phase: COM kinetic energy, muscle negative work, and potential energy stored in the Achilles tendon. As shown in *Figure 5.1*, The COM velocity increases from v_1 to v_2 such that the kinetic energy is increased. The transition in the terminal stance results in the ankle angle α to decrease from 90° to an acute angle.

During terminal stance, calf muscles do negative work to brake the human body [8]. The calf muscle and the tendon can be modeled as an actuator and a spring [93]. The tendon (spring) is stretched such that energy is stored. The positive and negative work from the ankle can be adapted from [1] [8] and are shown in *Figure 5.2.*

During terminal stance, calf muscle do negative work to the human body [8]. The calf muscle and the tendon can be modeled as an actuator and a spring [93]. The tendon (spring) is stretched such that energy is stored. This force acts like brake force for cars. The positive work and negative work from ankle can be adopted from

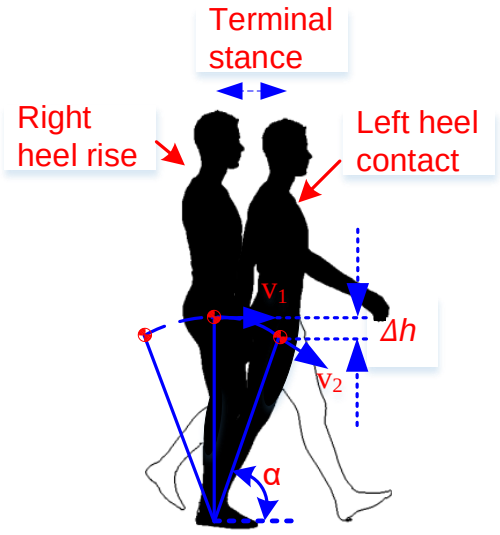


Figure 5.1: Inverted pendulum model of human walking. This figure is processed from video purchased from third party.

[8] [1] and shown in *Figure 5.2*.

From *Figure 5.2*, the positive and negative energy from the ankle can be calculated and is listed in *Table 5.1*. The work in A1 A4 is the integration of power in the corresponding period (red shaded area).

Phase	Energy exchange
A1	-0.6J
A2	0.3J
A3	-9J
A4	23.7J

Table 5.1: Power exchange in the ankle during walking. The negative energy is denoted as negative. [1]

There is -9J of energy in A3, which is the targeted energy source of our device during the terminal stance phase (*Table 5.1*). Any active muscle will consume metabolic energy, whether it is doing positive work, negative work, or no work at all [13]. It is assumed that the negative energy harvester will reduce the negative work the muscle has to do. In this way, the energy harvester will not burden the wearer. It is noted that is a consideration with the device design, the validity of the assumption was not

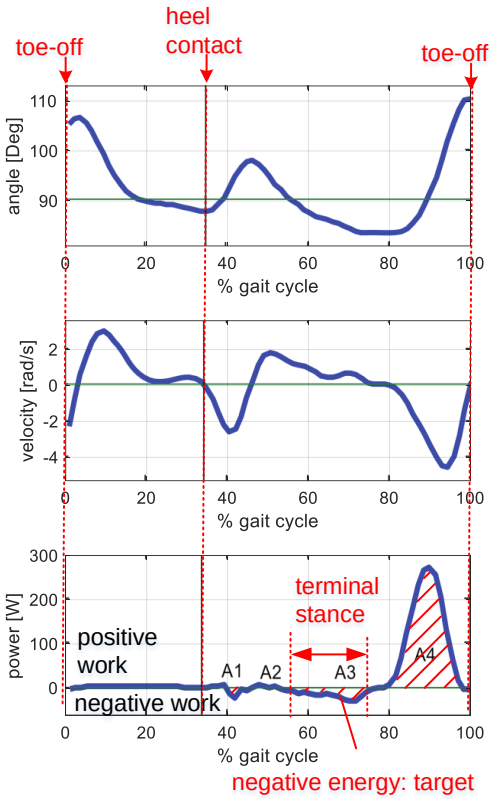


Figure 5.2: The full cycle of ankle angle α, velocity, and power during walking. Ankle angle α is defined as the angle between the shank and the foot. (Modified based on [1][8] under Creative Commons Attribution License and with open access.)

tested.

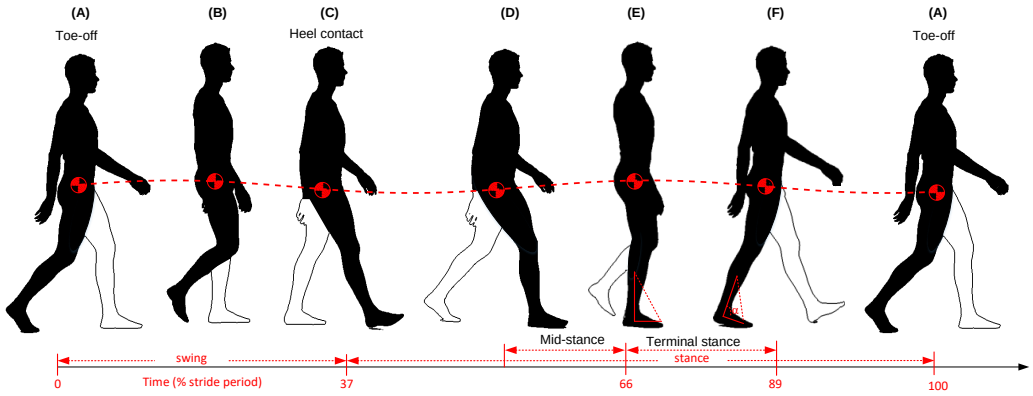


Figure 5.3: The full cycle of human walking. The energy-harvesting phase is in the terminal stance. This figure is processed from video purchased from third party.

It should be noted that the energy harvester cannot harvest all of the -9J of negative work in phase A3 because natural human gait dynamics must be maintained.

5.3 Design of negative work ankle energy harvester

We developed a wearable negative-work-harvester prototype to harvest the negative work done by the ankle joint during the terminal stance. As shown in *Figure 5.5*, during the initiation of the terminal stance, the angle between point M_1 and N_1 with respect to pivot O_1 is $\angle M_1O_1N_1$, which is also referred to as α_1. O_1 is the center of the ankle joint. According to the solution of triangles, the length of MN can be calculated as

$$MN = \sqrt{OM^2 + ON^2 - 2 \times OM \times ON \times cos\alpha} \tag{5.2}$$

This angle will change to $\angle M_2O_2N_2$ (or α_2) as the person approaches the end of the terminal stance. Due to the angular change from α_1 to α_2, the length of M_1N_1 will be decreased to M_2N_2. Taking advantage of this change, a harvester can be attached between point M and point N and harvest energy in the terminal stance.

The negative-work-harvester is shown in *Figure 5.5*. It consists of three parts: an electromagnetic rotatory generator (Maxon, 200142), a round bar, and a hollow rod. The round bar attaches to the shoe at one end and can pivot around the attachment

point. The pivot joint has three degrees of freedom, i.e. x, y, and z axial rotation, minimizing the risk of confining the natural motion of the ankle joint. The hollow rod is held in place against the shank by means of a strap. The round bar is inserted in the hollow rod, allowing relative motion between the two driven by the ankle motion during the terminal stance. A string is fixed to the top end of the round bar, exits out from an opening of the hollow rod, and is fixed to the generator shaft on the other end. The motion of the round bar relative to the hollow rod causes the length of string to change, initiating a winding mechanism on the generator shaft that transmits the linear motion in the string to the rotational motion of the generator. In this way, the relative motion between points M and N is transmitted to the generator, and power is generated. During the power generation phase, the rubber band on the back of the generator is wound and resets the generator to the initial position after the power generation phase ends to prepare for the next cycle.

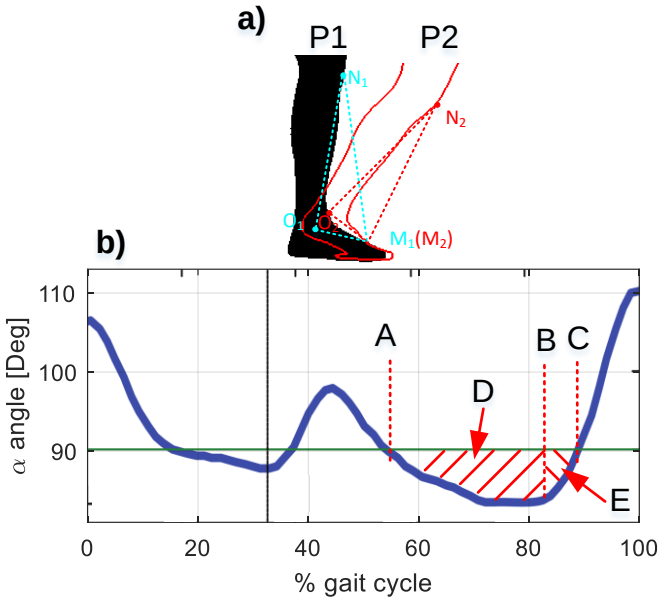


Figure 5.4: The modeling for energy harvesting working mechanism. a) low leg position in the starting (P1) and end (P2) of the terminal stance. b) energy harvesting phase in gait cycle. The energy harvesting phase is between P1 and P2, which is corresponding to (A) and (B) in b) (b) is modified based on [1][8] under Creative Commons Attribution License and with open access.)

The timing of the sequence is shown in *Figure 5.4*. The string will be loose when $\alpha \leq 90^{\circ}$, as illustrated before point A in *Figure 5.4*. The rubber band will hold the

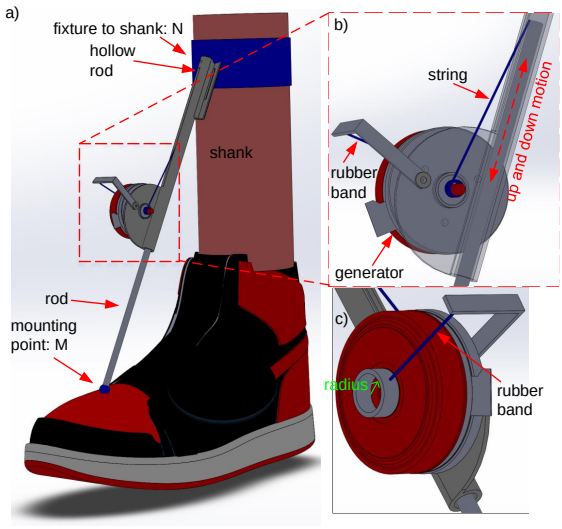


Figure 5.5: CAD model of the ankle energy harvester. a) Overall view; b) zoomed view of the generator c) backside view of the generator. The shoe model is created by Jason Lewis via GrabCad Community

generator in the initial position. When $\alpha \leq 90^\circ$ and decreasing, the string will be tight and will drive the generator to rotate by winding mechanism, as illustrated by the shaded area D in *Figure 5.4*. In this period, the rubber band will wind as the generator rotates and potential energy is stored. When $\alpha \leq 90^\circ$ and increasing, as illustrated by the shaded area E in *Figure 5.4*, the stored energy in the rubber band will drive the generator back to the initial position. The $\alpha \leq 90^\circ$ period at the heel strike is small. Due to the small motion of the ankle in that period, the power that can be produced by the generator in this phase is ignorable. This design ensures that the harvester engages at the right time and all the energy harvested is from phase D, when the calf muscle is doing negative work.

The device prototype is shown in *Figure 5.6*. The generator is of alternating current (AC) and has three phases. The detailed parameters of the generator are shown in *Table 5.2*.

As almost any increased weight carried by the wearer will result in an increase in metabolic cost [13], the system is designed to be lightweight at only 100 g in order to reduce the metabolic cost of using the device. The weight distribution of each component is shown in *Table 5.3*.

The device is mounted on the ankle and shown in *Figure 5.6*.

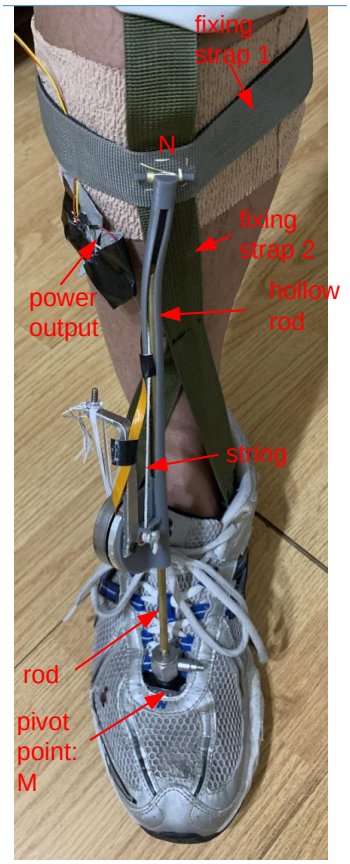


Figure 5.6: a) The negative energy harvester prototype; b) The device worn by a user.

Term	Value
Torque constant k_t	$2.7 \times 10^{-4} Nm/A$
Speed constant k_e	$2.7 \times 10^{-3} V/rpm$
Terminal resistance R_i	1.2Ω
Rotor inertia J_g	$9.3 \times 10^{-6} kg * m^2$
Shaft radius r	$4mm$

Table 5.2: Parameters of generator.

Item	Weight
Generator	75 g
round bar	6 g
hollow bar	18 g
Total	99 g

Table 5.3: Weight constitution of the harvester.

Fixing strap 1 is used to fix the harvester to the shank (*Figure 5.6*). As the skin is not rigidly fixed to the human skeleton, fixing strap 2 circles around the heel and is fixed to the upper end of the hollow rod.

5.4 Modeling

The modeling of the ankle energy harvester is shown in *Figure 5.7*.

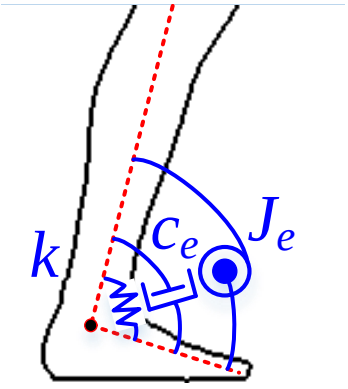


Figure 5.7: Modeling of the ankle energy harvester.

The torque τ provided by the harvester is

$$\tau = J_e\ddot{\alpha} + c_e\dot{\alpha} + k(\alpha - \frac{\pi}{2}) \tag{5.3}$$

where J_e is the equivalent rotational inertia of the generator rotor. c_e is the damping provided by the generator. k is the spring stiffness. The equivalent J_e, c_e, and k can be calculated from the system modeling. From *Eq. 5.2*, take derivative of both sides with respect to time, obtain

$$v_{MN} = \frac{d(MN)}{dt} = \frac{2 \times OM \times ON \sin\alpha}{2\sqrt{OM^2 + ON^2 - 2 \times OM \times ON \cos\alpha)}}\alpha \tag{5.4}$$

Then consider the generator shaft diameter as r, the angular velocity of the generator ω is

$$\omega = \frac{v_{MN}}{r} = \frac{2 \times OM \times ON \sin\alpha}{2r\sqrt{OM^2 + ON^2 - 2OMON \cos\alpha}}\dot{\alpha} \tag{5.5}$$

Therefore the gear ratio from ankle to generator is

$$n = \frac{\omega}{\dot{\alpha}} = \frac{2 \times OM \times ON \sin\alpha}{2r\sqrt{OM^2 + ON^2 - 2OM \times ON \cos\alpha}} \tag{5.6}$$

The rotational inertia of the generator rotor is J_g and the damping term provided by the generator is

$$c_g = \frac{k_t k_e}{R_{internal} + R_{Load}} \tag{5.7}$$

where k_t and k_e are the torque constant and speed constant of the generator respectively. $R_{internal}$ and R_{Load} are the internal resistance and load of the generator respectively. The derivative of this step can be found in [54]. The spring stiffness of the rubber band is measured as k_{rubber}, and consider the winding radius at the back end of the generator is r_{back}, the rotational torque $k_{rotation}$ provided by the rubber band is

$$k_{rotation} = k_{rubber} r_{back}^2 \tag{5.8}$$

Therefore, the equivalent rotational inertia J_e, electrical damping c_e, and spring stiffness k at the ankle are

$$\begin{cases} J_e = n^2 J_g = \frac{OM^2 ON^2 \sin\alpha^2}{(OM^2+ON^2-2\times OM\times ON\cos\alpha)r^2} J_g \\ c_e = n^2 c_g = \frac{OM^2 ON^2 \sin\alpha^2}{(OM^2+ON^2-2\times OM\times ON\cos\alpha)r^2} \frac{k_t k_e}{R_{internal}+R_{Load}} \\ k = n^2 k_{rotation} = \frac{OM^2 ON^2 \sin\alpha^2}{(OM^2+ON^2-2\times OM\times ON\cos\alpha)r^2} k_{rubber} r_{back}^2 \end{cases} \tag{5.9}$$

J_g,k_t,k_e,$R_{internal}$ can be obtained from the generator datasheet. The k_{rubber},r_{back},R_{Load},OM,ON,r can be measured from the system. In this way, the torque on the ankle is obtained and a function of ankle angle α. More energy will be stored as kinetic and potential energy if the rotational inertia J_e and spring k term increase. As the energy stored will be eventually harvested by the generator, those two terms can assist with the energy harvesting process. The question arises: which term should we increase to harvest more energy? Damping, inertia, or spring? Or they are the same? To answer this question, we have to look into the ankle angle profile α and the torque profile of the shank muscle, as illustrated in *Figure 5.8*.

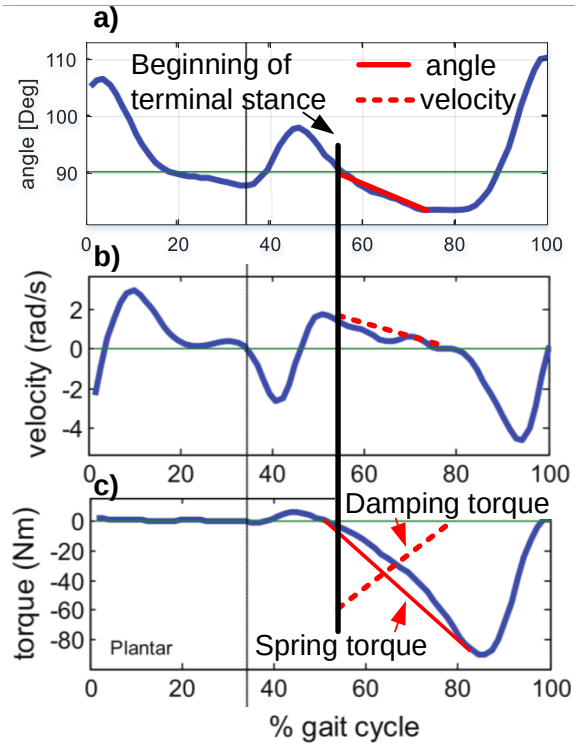


Figure 5.8: Ankle angle and torque profile. (The figure is modified based on [1] [8] under Creative Commons Attribution License and with open access.)

As illustrated in *Figure 5.8*, the energy-harvesting phase is in $50-80\%$ of the gait cycle. In this period, the ankle decrease from 90° to 83°, and the velocity profile decrease from $2\frac{rad}{s}$ to $0\frac{rad}{s}$. This will result in the torque profile illustrated as the solid and dash red line in *Figure 5.8 c)*. As the goal of the energy harvester is to assist

the ankle doing negative work, the spring torque is much better than the damping torque. The spring torque profile is the same as the muscle torque, and therefore is there to assist ankle muscles when needed. The damping torque is large at the beginning of the energy-harvesting phase, and small at the end of the same phase. It can be interpreted that the torque is there when it is not needed and disappear when the ankle needs it. This is the reason why damping torque is not preferred. The generator velocity is zero at the beginning of the energy-harvesting phase. It will suddenly increase to catch with the ankle motion. This will result in a large angular acceleration and hence large inertia torque. A similar force profile will be produced with the damping torque and hence is not welcomed. In conclusion, in order to produce a torque profile similar to the ankle muscles, spring is preferred over damping and inertia term.

5.5 Experiment validation

The performance of the ankle energy harvester was tested by a human participant (M. L., height: 172 cm, weight: 80 kg) walking on a treadmill at a constant velocity of 4.8 km/h (3 mph) while wearing the ankle energy harvester. Three resistors with 1 Ω resistance each were connected to each phase of the generator to dissipate the energy harvested according to *Figure 5.9*. The voltage output of the generator was collected by measuring the voltage on one resistor as shown in *Figure 5.9*. The other two phases are identical to this phase except for a 120° phase difference.

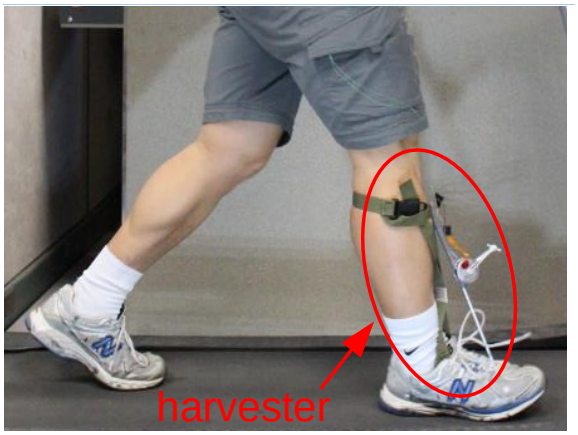


Figure 5.9: Treadmill experiment setup. The volunteer (M. L.) walks at 4.8 km/h with the harvester.

The electrical power output is calculated by

$$P = \frac{V^2}{R_L} \tag{5.10}$$

where V is voltage measured on the output of the generator. The experiment result is shown in *Figure 5.10*.

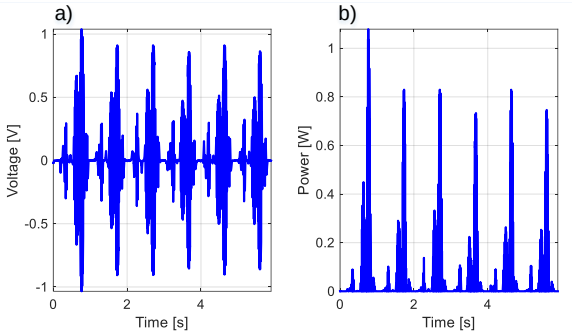


Figure 5.10: Experimental results. a) voltage output; b) power output. Treadmill test with a constant speed at 4.8 km/h (3 mph). The average power for one phase is 0.05 W. There is one generator on each leg and each generator has three phases. Two-legs combined result in total power output $0.3 \pm 0.05W$

From *Figure 5.10*, $0.3 \pm 0.05W$ of average power can be harvested from the ankle energy harvesting device. In order to illustrate the negative work harvested from the ankle motion, the energy-harvesting phase is compared with a full gait cycle and shown in *Figure 5.11*.

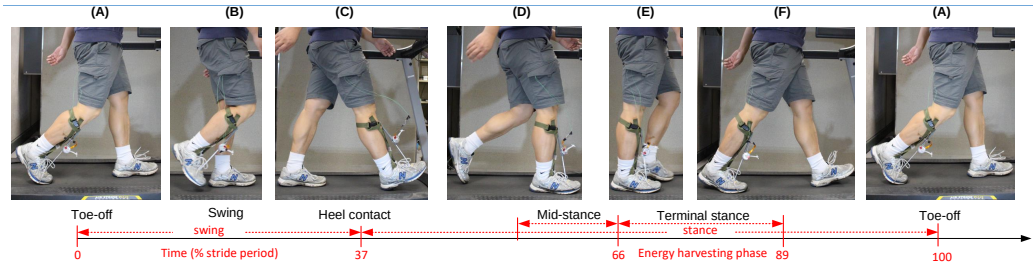


Figure 5.11: Energy harvesting period in a full gait cycle. The photos are from testing with the participant walking on a treadmill at 4.8km/h (3 mph).

The rotational velocity of the generator can be obtained from the voltage by $\omega = \frac{V}{k_e}$, where V is the voltage produced by the generator, and k_e is the generator speed

constant. The motion of MN is measured with a displacement sensor (LMC(R) 13-100 by P3 America). The whole energy harvesting process was videotaped and the keyframes were identified. Heel strike, terminal stance, and swing phase can all be identified from the video and compared with the generator rotation profile *Figure 5.12*.

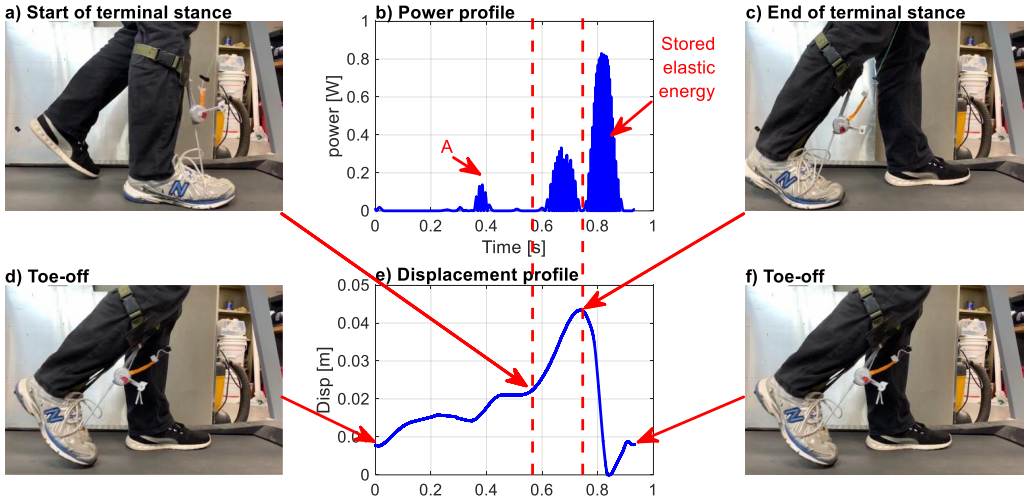


Figure 5.12: Energy harvesting in complete gait cycle.

The energy-harvesting phase is clearer when the power output is plotted and compared with the walking cycle. From *Figure 5.12*, it is clear that the energy-harvesting phase corresponds with stance. It is also noted that 0.003 J energy is harvested before the terminal stance (denoted as A in *Figure 5.12* b)), which is considered negligible compared with 0.05 J of total energy harvested during one gait cycle. Due to the winding of the rubber band, there is still some energy during the push-off phase, which is denoted as "stored elastic energy in *Figure 5.12* b), which comes from the potential energy in the rubber band. It is not driven by the shank. The calf muscle activity is also recorded by recording the EMG signal of the medial and lateral gastrocnemius muscle.

The displacement is the relative motion between the rod and hollow rod and measured by displacement sensor (LMC(R) 13-100 by P3 America). The force is picked up by the force sensor illustrated in *Figure 5.6* (lower end of the rod). The medial and lateral gastrocnemius EMG signal is picked up by Bagnoli EMG system by DELSYS. From *Figure 5.13*, it can be observed that the energy harvesting happens when the gastrocnemius muscle is doing negative work, i.e. in 0.45-0.65 s in the time

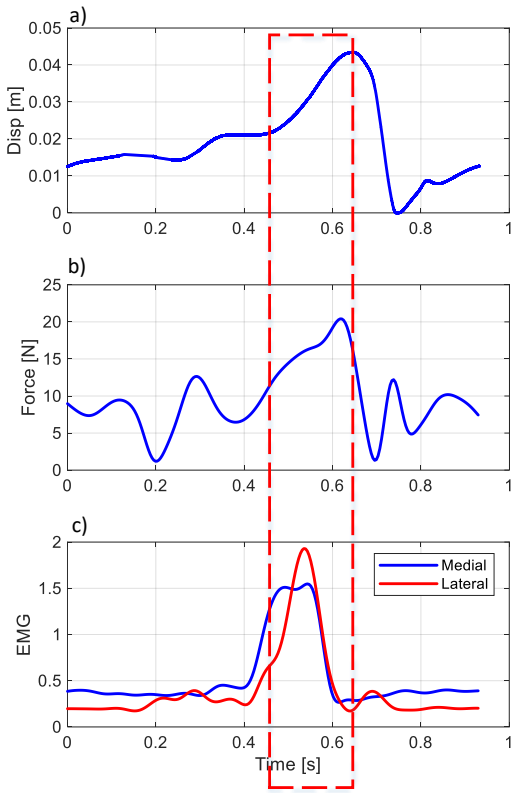


Figure 5.13: Energy harvesting vs gastrocnemius muscle activity in the time domain. a) harvester displacement (between the rod and the hollow rod); b) force on the harvester; c) EMG signal in lateral and medial gastrocnemius muscle.

domain, during which only force is obvious in the harvester. The soleus muscle is active as observed from the EMG graph, and it is doing negative work.

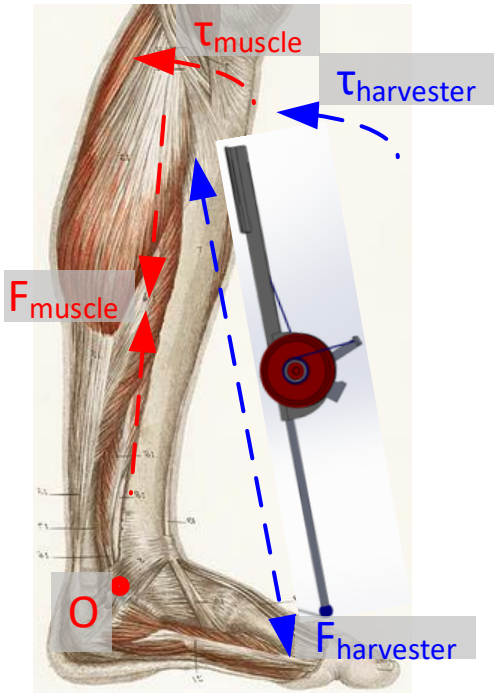


Figure 5.14: Torque analysis on the ankle joint: the muscle torque and the harvester torque.

From *Figure 5.13*, it is shown that the gastrocnemius muscle active and force active period is overlapped in 0.45-0.65 s. As illustrated in *Figure 5.14*, the shank moves clockwise pivoting ankle joint O. The gastrocnemius muscle is active and providing a counter-clockwise torque τ_{muslce}. As the motion is clockwise and the gastrocnemius muscle torque is counterclockwise, the gastrocnemius muscle is doing negative work. In the meaning time, the harvester provides an extending force $F_{harvester}$, and hence resulting a counterclockwise torque $\tau_{harvester}$. The direction of $\tau_{harvester}$ is the same as the τ_{muscle}. Hence, the harvester is assisting the gastrocnemius muscle in doing negative work.

Apply the parameters to the *Eq. 5.3* (refer to appendix for details), obtain torque on the ankle $\tau = 7.4 \times 10^{-2}\ddot{\alpha} + 2.4\dot{\alpha} + 8.5 \times e^{9.1(\alpha-1.6)} \times (\alpha - 1.6)$. The ankle angle, ankle velocity, and ankle acceleration from literature [8] [13] can be compare with experiment data, the comparison result can be found as *Figure 5.15*.

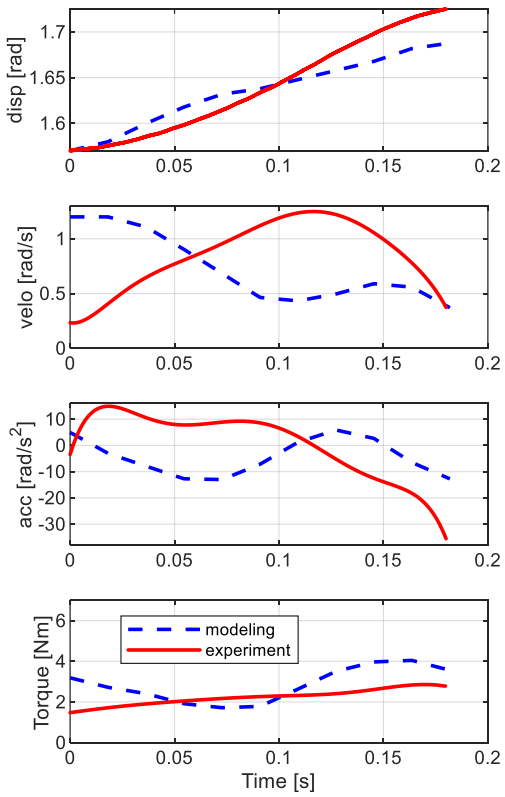


Figure 5.15: Ankle motion and corresponding torque produced from harvester.

From *Figure 5.15*, the ankle angle measured from the experiment matches with the data from the literature with acceptable error. However, the experimental angle velocity and acceleration data cannot match the data from the literature. The following are the possible reasons we have speculated but yet to verify:

1. The soft skin and soft tissue in the human body are not modeled. The connection between the harvester and the human body is modeled as rigid. However, the human skin is very flexible in small-scale motion. As a result, the velocity is supposed to be some large value in the initial contact (at time zero in *Figure 5.15*), but due to the soft connection, the velocity starts with some value close to zero.

2. The influence of the harvester on the ankle angle. The harvester will have torque on the ankle and that will change the acceleration and velocity of the ankle angle. However, since there is no specific equation to describe the interaction between the human body and the harvester, the interaction is not modeled. Instead, the human ankle angle is treated as definite input to the harvester. This might cause the difference between the experiment result and the modeling result.

3. Different from person to person. The experiment is from a single person. However, the difference between individuals is quite large. As observed from the experiment we did, the difference between individuals can be as much as 100%. 4. The changing shaft diameter due to the winding mechanism. The string will cumulate on the shaft because of the winding mechanism. The shaft radius is $0.0025m$ before winding, but can increase to $0.004m$ after winding for multiple rounds.

As a result, the experimental data can be explained roughly but not in detail.

This device was compared with biomechanical energy harvesting devices in literature based on the power harvested, weight, and negative work phase and the results are shown in *Table 5.4*. The metabolic cost increase due to the extra mass that has to carry is derived from [97]. Note that the human body is set at a typical value of $80kg$.

From the comparison in *Table 5.4*, the current device is the lightest while harvesting substantial power. It is noted that the harvester we presented has a decent power ratio (power harvested / metabolic power increase due to weight carrying), but it is still lower than the critical value of 1.

Device	Position	Power	Weight	Position	metabolic	efficiency	Negative
Backpack [4]	Backpack	5.6W	5.6kg	Back (3.6 W/kg)	20	0.28	NA
Knee [3]	Knee	5.0W	1.6kg	Knee (6.0 W/kg)	9.6	0.52	Yes
Ankle [94]	Ankle	1.0W	0.60kg	Ankle (1.7 W/kg)	9.6	0.10	Yes
Ankle [95]	Ankle	0.35W	0.40kg	Ankle (16 W/kg)	6.4	0.05	Yes
Current	Ankle	0.30W	0.10kg	Shank (6.1 W/kg)	0.60	0.50	Yes

Table 5.4: Performance comparison between different biomechanical energy harvesting (EH) devices.

5.6 Discussion

When assessing energy harvesting devices, five main factors must be considered: the muscles negative work phase during each motion, the means by which the device is attached to the body, the convenience of use of the device, the additional weight of the device on the amount of effort expended by the wearer, and finally the effect of the harvesting energy device on the body [1]. At the same time, the energy harvester should not affect the users preferred gait, as almost any deviation from the users natural gait will increase the metabolic cost [96]. As a result, the harvester should be designed to not impede the natural human motion. At the same time, the harvester should be as light as possible to decrease the impact on the human body. The cost of carrying weight on the human body is characterized in [97] and show that distal leg loads increase the metabolic rate required for swinging the leg. For electrical power generation over a longer duration, it would be desirable to harvest energy from everyday activities such as walking and backpacking. The energy harvester was designed by following the design criteria mentioned above.

However, due to the design goal of being lightweight and minimizing the influence on natural human gait, the power harvested is only 0.3 W, which is much less than the 1 W case previously published by our group [94]. There is a balance of harvesting more power and not impeding the wearer. We plan to do further experiments with the harvester while measuring the metabolic cost to evaluate the influence of the energy harvester on the wearer.

Chapter conclusions

In this paper, we designed an ankle energy harvester that only harvests negative work during human walking. The energy harvester mounts on the foot and harvests

energy during the ankle negative work phase. The harvester weighs less than $100g$ and is non-invasive. Treadmill experiments show that $0.3 \mp 0.05W$ of energy can be harvested during human walking ($4.8\ km/h$ or $3\ mph$). The device is shown to harvest energy only during the negative work phase, so it has the potential of not increasing the metabolic cost. Experiment results also show that the harvester is having torque at the same time and direction of the shank muscle, indicating the harvester is trying to assist the muscle doing negative muscle work. The modeling, design considerations, and parameter choice are discussed in detail. Harvesting energy with the potential of not increasing the burden on the human user is a promising way to power wearable and mobile electronic devices. Even though no clear evidence is shown this harvester can be net-zero harvester (energy harvesting at no increase of metabolic cost), this paper paves ways towards that goal. Further work should be done to improve the amount of power harvested and investigate the influence of the harvester on human metabolic cost and human gait.

5.7 Appendix

Apply $OM = 0.12m$, $ON = 0.3m$, $\alpha = 90°$, and $r = 0.0025m$ to *Eq. 5.6*, and obtain $n = 89$. Apply $J_g = 9.3 \times 10^{-6} kgm^2$, $k_{rubber} = 64e^{25x} N/m$,$r_{back} = 0.041m$, $R_{internal} = 1.2\Omega$,$R_{Load} = 1\Omega$, $k_t = 2.55 \times 10^{-2} Nm/A$, $k_t = 2.55 \times 10^{-2} V/rad$ to *Eq. 5.9* and obtain $J_e = n^2 J_g = 7.4 \times 10^{-2} kgm^2$, $c_e = n^2 c_g = 2.4Ns/rad$, $k = n^2 k_r otation = 8.5Nm/rad$. Then apply to *Eq. 5.3* and obtain torque on the ankle $\tau = 7.4 \times 10^{-2}\ddot{\alpha} + 2.4\dot{\alpha} + 8.5 \times e^{9.1(\alpha-1.6)} \times (\alpha - 1.6)$. The spring stiffness of the rubber is a little bit complicated due to the winding part. Even though the length of the rubber between the fix point and the winding wheel is does not change due to winding, the effective part (the length of the original rubber in length L) changes. The changing of effective length will change the stiffness. The photo of the winding mechanism and its illustration is shown in *Figure. 5.16*.

As illustrated in *Figure. 5.16*, the original length of the rubber band is L and the effective length is L' after winding by length x. Equation can be obtained as

$$L - L' = \int_0^x \frac{L'}{L} dx \tag{5.11}$$

Solve the equation and obtain

$$L' = Le^{-\frac{x}{L}} \tag{5.12}$$

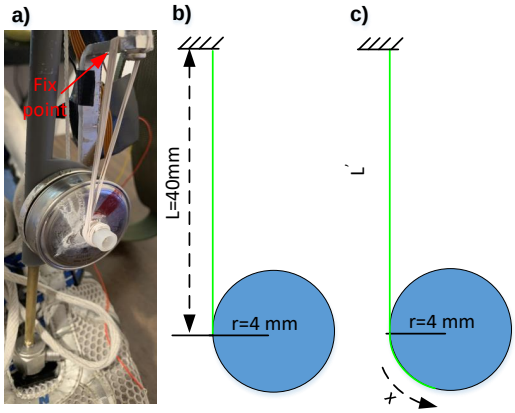


Figure 5.16: Rubber band spring illustration.

The original stiffness of the rubber band can be measured as k_{base}, as the spring stiffness is inverse proportional to the rubber band length, the effective rubber band stiffness is

$$k_{rubber}(x) = k_{base}\frac{L}{Le^{-\frac{x}{L}}} = k_{base}e^{\frac{x}{L}} = k_{base}e^{25x} = k_{base}e^{25x} \tag{5.13}$$

Chapter 6

Energy Harvesting tile/paver

6.1 Chapter introduction

Developments and deployment of smart infrastructure and the global expansion of digital inter-connectivity have been increasingly shaping our day-to-day activities. This is particularly evidenced by the Internet of Things where connectivity has extended to everyday objects, enabling them to send and receive data. Ubiquitous sensing is key to the Internet of Things [98]. However, powering the sensors can be a problem, especially in far and remote places. Running long wires or replacing batteries to power sensors can be costly, inconvenient, or even impractical. Harvesting energy from the ambient environment could be a key source for providing off-grid power supply for sensors used in smart infrastructure, structural health monitoring, and environment sensing [10] [23] [99]. As sensors and communication systems require less and less power, energy harvesting becomes more promising. Both piezoelectric [29] [100] [101] [102] and electromagnetic [103] [104] [105] [39] [106] transducers have been used at small-scale, mid-scale and large-scale energy harvesting.

Energy harvesting from the human body and human motion has many applications, including powering wearable and mobile devices [107]. Rome *et al.* [4] designed an energy harvesting backpack by using an electromagnetic generator to harvest kinetic energy from human walking. They experimentally obtained a maximum output power of $5.6W$. Donelan *et al.* [3] designed an electromagnetic energy harvester based on the motions of knees and legs. Their experiments demonstrated that an

average power of $5W$ can be harvested from these motions, while causing little extra human effort. Researchers have long been focusing on harvesting energy from the interaction between the human foot and the ground. MIT Media Lab's energy harvesting shoes proved capability of harvesting average $1.3mW$ from PVDF stave, $8.4mW$ from PZT unimorph and $250mW$ from electromagnetic generators [84] [70]. Fu *et al.* designed energy harvesting shoes based on footstep-induced airflow and harvested $6mW$ from pedestrians [108]. Wu *et al.* came up with an electromagnetic wearable 3-DoF resonance human motion energy harvester and harvested $2.3mW$ [109]. Hsu *et al.* devised a novel ultra-high power density energy harvesting method based on reverse electro-wetting [110]. They fabricated small lightweight energy harvesting devices capable of producing a wide range of power for the application of energy harvesting shoes.

Energy harvesting tiles have received attention because of multiple potential applications that include powering infrastructure sensors, ambient lighting fixtures, and nearby communication systems [111]. Zhao *et al.* [112] designed a cymbal-based piezoelectric energy harvester embedment in the asphalt pavement to harvest energy from automobiles. Their numerical simulation results showed a potential maximum power output of $1.2mW$ from passing vehicles. Xiong and Wang [113] installed a piezoelectric energy harvester on a public roadway and demonstrated the ability to harvest an average output power of 2 $3mW$ and a peak power of $100mW$ from passing trucks. Sharpes *et al.* [114] presented the concept of a piezoelectric tile energy harvester that is placed below the floor surface. They showed that the output energy from footsteps could be used for building automation or control in smart buildings. Yao *et al.* [16] used triboelectric material to design a triboelectric nano-generator. They were able to harvest $0.5mW$ of power from human steps. Although these different approaches used to harvest energy from tiles are interesting and meaningful, they do not take full advantage of the potential energy. As a result, the amount of energy harvested is still at the mW level.

Another approach to harvest energy from footsteps is the electromagnetic-based energy-harvesting tile. Pavegen has commercialized electromagnetic-based energy-harvesting tiles that convert the floor's up-and-down motion to the rotational motion of an attached generator to produce electricity [89]. Taliyan *et al.* [115] designed a footstep energy-harvesting device that uses a DC generator. Their experimental results show that $3 \sim 5J$ of electrical energy can be generated from each step. However, the tile top panel displacement is $3cm$, which is not only uncomfortable

for pedestrians, but also would not conform to the Americans with Disabilities Act (ADA) [116]. This act limits the amount of the vertical height difference between pavement joints. Bhatia *et al.* [117] designed an energy harvesting tile using rack and pinions. They were able to harvest $0.36W$ average power. The displacement of the device's top panel varied $13 \sim 38mm$, which incurs the same comfort and regulatory code issues as the Taliyan tile [115]. Furthermore, their overall efficiency, which is less than 20%, is still low. Another company, *Waydip* came up with an energy harvesting tile called Waynergy that can harvest $0.3 \sim 0.6J$ of energy per step. Considering the energy potential, their overall efficiency is 13.6% [118].

In summary, the overall efficiency of existing research on energy harvesting tiles is less than 20%. The energy output is far below the available potential energy during human walking. This paper presents a novel design of energy harvesting tile that efficiently harvests energy from human walking and makes them more useful in real-world applications. A DC generator is used to convert kinetic energy into electricity. A one-way-clutch is placed between the gears and the shaft to extend the energy harvesting period. Based on the mechanism of this clutch, energy harvesting continues even after the top panel reaches its displacement limit. The period of energy harvesting is further enhanced by using a flywheel that is attached to the electric generator rotor. A complete dynamic model is developed with the consideration of the Coulomb damping, electrical damping, and mechanical damping. Based on this model, system parameters are analyzed to optimize energy harvesting performance. The role of the flywheel and the load resistance is analyzed and discussed. Experiments are carried out to verify the dynamic model. The experimental results match well with numerical simulations. The experimental results show that the energy harvesting tile can produce an average power output of $3.6W$ over $0.5s$ of the step time, with a peak power of $12W$. The output of electrical energy is $1.8J$ per step. It is shown that 75% of the theoretically available potential energy during human walking is transmitted to the energy harvesting tile. This exceeds values in the published research work by a significant margin. The flywheel's influence on energy harvesting in walking, fast walking, and running conditions are compared and discussed.

This paper is organized as follows: Section 2 describes the working principle, design, and fabrication of the proposed energy harvesting tile. In Section 3, the dynamic model of the energy harvesting tile is developed and analyzed. The electric load and flywheel are optimized to harvest more energy with high efficiency. The tests and results of the proposed energy harvesting tile are presented in Section 4. Conclusions

are provided in Section 5.

6.2 Concept, design and prototype

6.2.1 Concept

According to literature [9] [119], human walking induces a 500 $\sim$ 1000 N dynamic force on the ground. In this section, the conceptualization and design of the proposed tile to harvest human motion energy efficiently are discussed. The idea is that when a pedestrian steps on the tile, it gently shifts 6mm downwards and harvests the work done by this motion. Compared with the pedestrian's height and stride length, a displacement of 6mm is small. This motion likely has a negligible effect on the human effort of walking. Although seemingly slight, this displacement can be used to generate electrical energy. Importantly, the 6mm displacement also falls within the range recommended by the Americans with Disabilities Act [116].

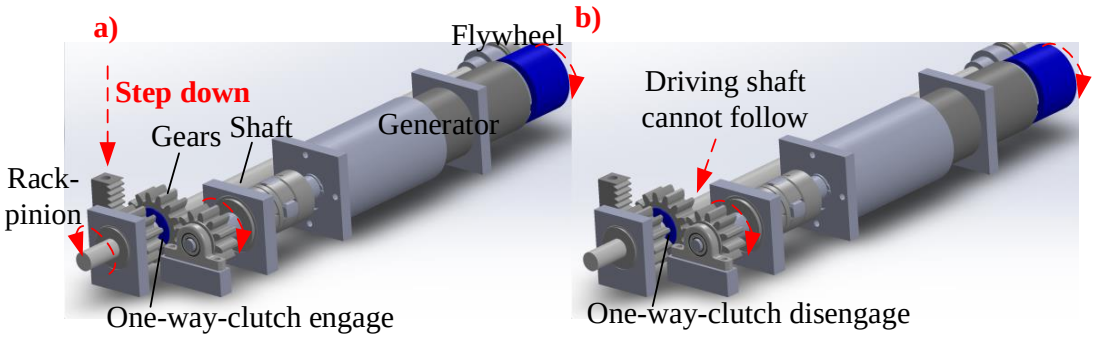


Figure 6.1: Working principle of the energy harvesting tile: (a) step down; (b) free rotation.

The working principle of the proposed energy harvesting tile is shown in *Figure 6.1*. The pinion gear rotates counter-clockwise when the step force acts on the rack. The shaft rotates with the pinion gears. The one-way-clutch is engaged and the gears between the shaft and the generator rotate and drive the generator to rotate clockwise.

As shown in *Figure 6.1(b)* , when the displacement of the rack reaches its limit or the movement of the rack cannot keep up with the rotational motion of the generator, the one-way-clutch disengages. This disengagement enables the generator to keep rotating due to the rotational inertia and to continue harvesting energy. A flywheel is attached to the end of the generator to increase the rotational inertia. This design enables the generator to have continuous output power while fully harvesting the potential energy.

6.2.2 Design and prototype

In order to make the energy harvesting tile easy to assemble and scale up to deploy as part of a pathway, the proposed tile is made of energy tile modules as shown in *Figure 6.2*. Taking the average human stride length of 72 cm [48] into consideration, the modular energy harvesting tile is designed to have a size of $40cm \times 40cm \times 5cm$.

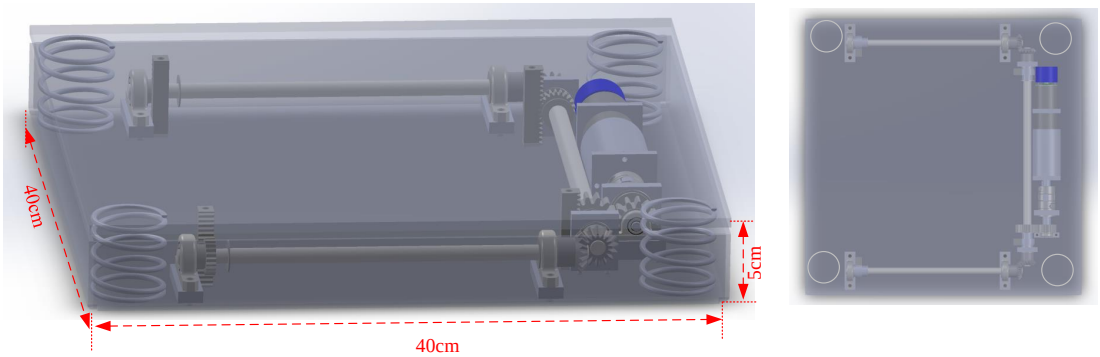


Figure 6.2: CAD design of the energy harvesting tile: (a) 3D view; (b) top view.

As shown in *Figure 6.2*, the cover (top panel) of the box will move up-and-down when it is stepped on. Four rack-and-pinion, one at each corner, are then used to transmit the up-and-down motion to the rotation motion of the shafts. Thus, the panel can always drive the generator no matter whether the step force is applied. Bevel gears synchronize the motion of all the three shafts. When the top panel reaches its displacement limit of 6 mm (stopped by the wall of the box) or the top panel cannot keep up with the rotation of the generator anymore, the one-way-clutch disengages. Meanwhile, the generator continues to rotate due to inertia and

to produce electrical energy. The flywheel attached at the high-speed shaft of the electric generator extends the duration of the rotation. When the step is released, the generator is disengaged by the one-way clutch. The springs in the four corners reset the top panel to its original position. *Figure 6.3* shows the prototype assembly of the presented energy tile.

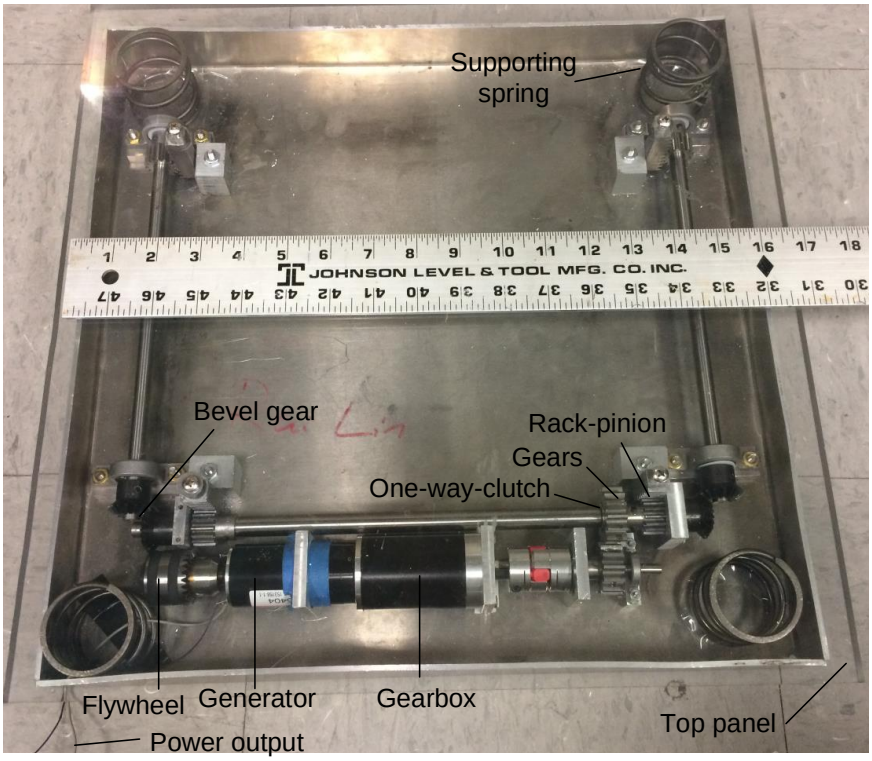


Figure 6.3: Prototype of the energy harvesting tile (one module).

6.3 Modeling and simulation

6.3.1 Potential Energy

Human walking results in a Vertical Ground Reaction Force (VGRF) on the ground. Tongen *et al.* [9] measured typical walking, speed walking, and running VGRF profiles, as shown in *Figure 6.4*.

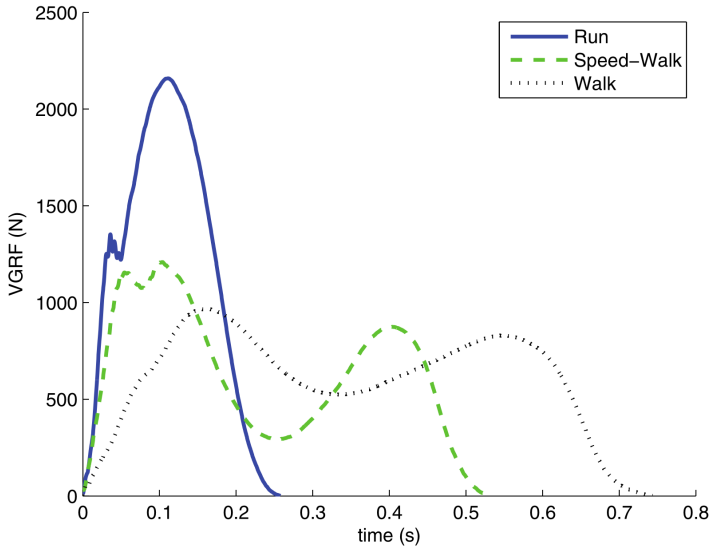


Figure 6.4: Typical vertical ground reaction force (VGRF) for one step during walking, speed walking and running [9].

The potential energy from the human walking is given by:

$$W = \int F ds \tag{6.1}$$

where W is the work done; F is the VGRF and S is the displacement of the tile's top surface. Based on the VGRF shown in *Figure 6.4*, a force of 800 N, and a total top panel displacement of 6 mm, the total potential energy is estimated to be 4.8 J. 3.2 System modeling 3.2.1 Modeling of the generator The generator shown in *Figure 6.5* can be modeled as a voltage source with internal and load resistances. An equivalent model is shown in *Figure 6.4*.

The voltage V produced by the generator is calculated as:

$$V = k_e \omega \tag{6.2}$$

where k_e is the speed constant of the generator; w is the rotational angle of the generator rotor; $\dot{\theta}$ is the generator rotational velocity. According to Kirchhoff's

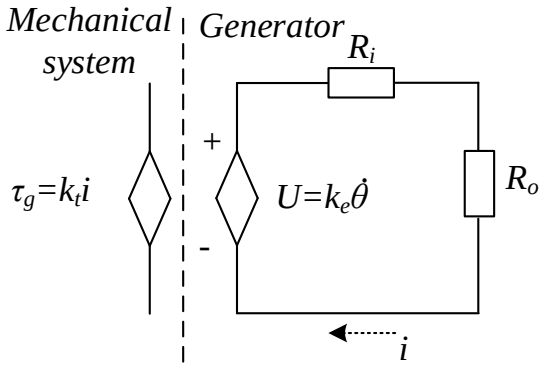


Figure 6.5: Modeling of the electrical generator.

voltage law:

$$k_e w = iR_i + iR_L \Rightarrow i = \frac{k_e w}{R_i + R_L} \tag{6.3}$$

where i is the current,R_i and R_L are respectively the internal and load resistances of the generator. The torque produced by the generator is written as:

$$\tau g = k_t \Rightarrow i = \frac{(k_t k_e) w}{R_i + R_L} \tag{6.4}$$

where τg denotes the torque produced by the generator and kt is the torque constant of the generator. As such, the force produced by the generator is proportional to rotational velocity $\dot{\theta}$ and the generator can be treated as a damping term with a damping coefficient c_e given by:

$$c_e = \frac{k_t k_e}{R_i + R_L} \tag{6.5}$$

6.3.2 Overall model

Based on the above modeling of the generator and the working principle, the energy harvesting tile can be modeled as a mass-spring-damper system as shown in *Figure 6.6*. The response upon a human footstep has two phases: Phase I during the step-down and Phase II during the free rotation.

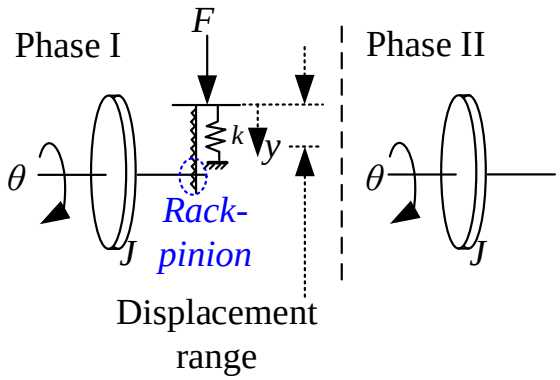


Figure 6.6: Working principle of the energy harvesting tile. Phase I: the step down and Phase II: free rotation.

As the step force F acts on the top surface of the tile, the rack and pinion turn the vertical displacement into a rotational motion. As shown in *Figure 6.6*, the input is the step force F during which the one-way-clutch engages. When the one-way-clutch engages, the top panel displacement will be coupled with the generator, i.e. $y = \frac{\theta r}{n}$, where θ, n and r are respectively the rotational angle of the generator rotor, the overall gear ratio that consists of the gears and gearbox, and the radius of the pinion gear. The governing equation of motion during Phase I is written as:

$$J\dot{\omega} + (c_m + c_e)\omega + T_f = \frac{F - ky}{nr} \tag{6.6}$$

where J is the equivalent rotational inertia, which is the total rotational inertia of the generator rotor, flywheel, and gearbox. The parameters c_m and c_e represent respectively the equivalent mechanical damping and electrical damping of the system. The mechanical damping force is modeled as viscous damping force cm $\dot{\theta}$ and Coulomb damping torque T_f. The parameter k is the total stiffness of the four supporting springs in parallel. The springs are designed to push the tile top panel back to its original position after the foot releases. When the top panel hits the walls of the supporting box or the top panel cannot keep up with the rotation of the generator, the one-way-clutch disengages. At that time, the system becomes a mass-damping system as presented by Phase II in *Figure 6.6*. The corresponding governing equation becomes:

$$J\dot{\omega} + (c_m + c_e)w + T_f = 0 \tag{6.7}$$

As the step force F decreases, the springs will push the top panel back to its original position. Overall, the governing equations are written as follows:

$$\begin{cases} (J\dot{\theta} + (cm + ce)\dot{\theta} + Tf = \frac{F-ky}{n}r; y = \frac{\theta r}{n}F > ky, y < 0.006(PhaseI) \\ J\ddot{\theta} + (cm + ce)\dot{\theta} + Tf = 0; F > ky, y = 0.006(PhaseII)) \end{cases} \tag{6.8}$$

Based on this model and the input force, the output of the energy harvesting tile can be predicted. The numerical results are presented in the next section. In addition, a comparison between numerical simulation and experimental results is presented in Section 4.

6.3.3 Simulation and parameter optimization

All of the system parameters can be obtained from datasheets (Table 1) except the system's mechanical damping cm and the Coulomb damping torque Tf. These two parameters depend on the system assembly and material characteristics. They cannot be obtained directly. For this paper, these parameters are determined by fitting numerical simulation to experimental results. The experimental VGRF shown in *Figure 6.7 (a)* constitutes the input to the system model. By varying cm and Tf and then getting the smallest error between the two results, the value of cm and Tf were determined. With this approach, the values of these parameters were determined to be cm=0.011 Nms/rad and $T_f = 2.9 \times 10^{-3} Nm$. The input force and fitting results are presented in *Figure 6.7 (a) and (b)*, respectively.

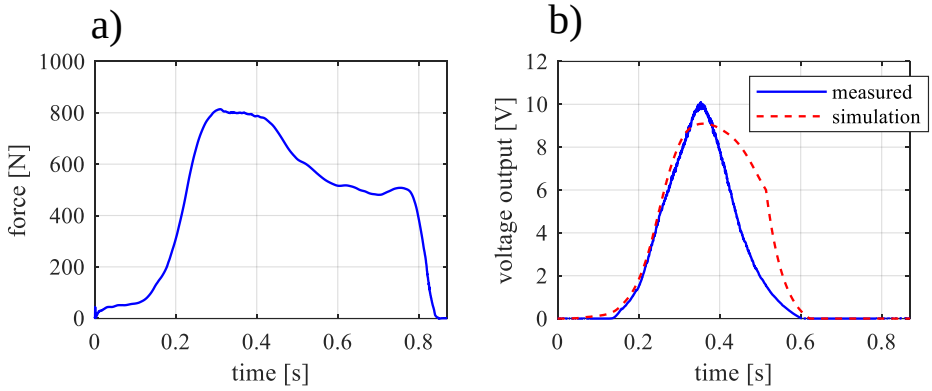


Figure 6.7: Parameter identification result: (a) Vertical Ground Reaction Force (VGRF) from experiments; (b) voltage output comparison.

Table 6.1: System parameters of the energy harvesting tile.

Symbol	Quantity	Parameter meaning
J	$2.5 \times 10{-}5kgm^2$	total rotational inertia of generator rotor and the flywheel
r	$7.5 \times 10^{-3}m$	radius of the pinion gear
c_e	$0.012Nms/rad$	equivalent electrical damping (load resistance: 10ω)
c_m	$0.011Nms/rad$	mechanical damping
k	$3.6 \times 10^4 \frac{N}{m}$	total stiffness
n	52	overall gear ratio
k_t	$5.3 \times 10^{-2}Nm/A$	torque constant
k_e	$5.3 \times 10^{-2}Vs/rad$	speed constant
R_i	2Ω	internal resistance
T_f	$2.9 \times 10^{-3}Nm$	Coulomb damping torque

Upon determining all of the parameters, the VGRF data obtained from experiments is used as an input to the system model. The system has a flywheel attached to the end of the generator. The flywheel has 1.9 times the rotational inertia of the generator rotor. The results are presented in *Figure 6.8*.

As shown in *Figure 6.9* at the onset of phase I, the generator starts to rotate when the input force is applied to the top panel. When the top panel cannot keep up with the rotation of the generator or stopped by the sidewalls of the energy harvesting tile, the one-way-clutch disengages and the generator continues to rotate due to inertia, as shown in *Figure 6.9 (b)*. If the friction force is small compared to the damping force, it can be neglected in the model. The rotational velocity can be modeled as:

$$w = e^{\frac{-(c_m+c_e)}{J(t-t_0)}} w_0 \tag{6.9}$$

where $\omega = \dot{\theta}$ is the rotational velocity of the electric generator, t0 is the disengagement time and w0 is the rotational velocity when the one-way-clutch disengages. As such, the rotational velocity follows an exponential decay, as shown in *Figure 6.9 (b)*. Because the voltage output is proportional to the rotational velocity, it follows the same exponential decay rate. The kinetic energy stored as rotational inertia is harvested, as shown in *Figure 6.9 (c)*. As the foot lifts off, the top panel is pushed back to its original position by the springs. With this design, more energy induced by the footstep can be harvested. Different electrical loads will result in different dynamic profiles and, thus result in different levels of energy output. In order to find

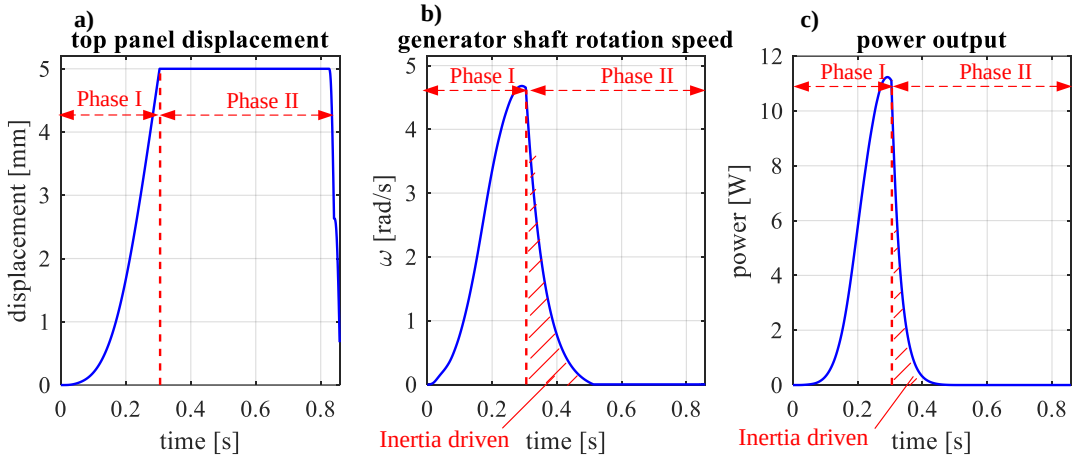


Figure 6.8: Numerical simulation results of the energy harvesting tile: (a) top panel displacement; (b) generator rotational angular velocity; (c) power output. All system parameters are from the energy harvester prototype. 10 ω load resistor is used in the simulation.

out the optimal load resistance for maximum energy output, the system is simulated using different values of the load resistance. The variations of the displacement, rotation speed of the generator's shaft, and the power output as a function of the load resistance levels are presented in *Figure 6.9*.

The electrical energy output W is determined by integrating the output power over the time span of one-step. It is defined as follows:

$$W = \int_{t_e}^{t_s} P dt \tag{6.10}$$

where P is the power output and t_s and t_e are respectively the starting and ending points of energy harvesting over the period corresponding to one footstep. When the load resistance is small, the equivalent damping is large. It will take a relatively long time for the top panel to reach its limit. This is illustrated by the 1 ω case in *Figure 6.9*. The rotational velocity is small due to the increased working time. The small rotational velocity means a small voltage output. The electrical efficiency is calculated by:

$$\eta_e = \frac{R_L}{R_i + R_L} \tag{6.11}$$

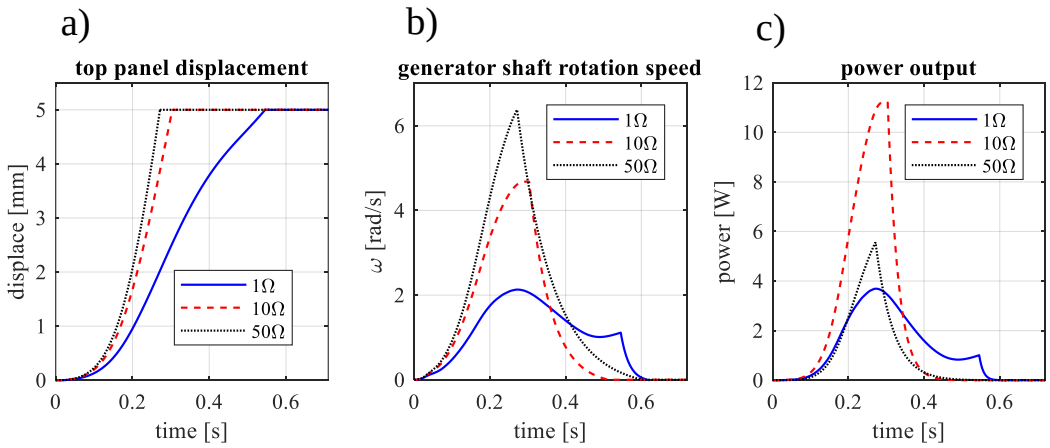


Figure 6.9: Variations of the (a) top panel displacement; (b) generator rotational speed; (c) power output as the load resistance changes.

where the electrical efficiency η_e decreases when$R_L$decreases. Therefore, the energy efficiency is low, and total energy output is low when load resistance is small. When the load resistance is large, as illustrated with 50 Ω case in *Figure 6.9*, the top panel velocity and the generator rotational velocity are large. Thus, the output voltage is large. However, the electrical power output $\frac{U^2}{Ri+Ro}$ will become small because$R_L$is large. Therefore, the level of harvested energy is low. Based on the above analysis, it is determined that in both small and large load resistance cases, the output electrical energy is small. The energy output reaches its maximum in the middle range of the load resistance. In order to find the optimal resistance for the maximum energy output, a profile of different energy outputs based on different load resistance is simulated and presented in *Figure 6.10*.

Figure 6.10 shows that the electrical energy harvested per step is low for both small and large load resistance cases. The energy output reaches its maximum when load resistance Ro=7 ω. In this way, the optimal load resistance can be found by modeling and simulation. The numerical simulation helps the experiment design process by guiding the choice of system parameters. Based on the performance of the generator in the test, 70% generator efficiency is assumed in this figure. As shown in *Eq. 6.6*, when the foot touches the top panel, the governing equation of motion is written as:

$$\ddot{\theta} = \frac{\frac{Fr-kyr}{n} - (cm + ce)\dot{\theta} - Tf}{J} \tag{6.12}$$

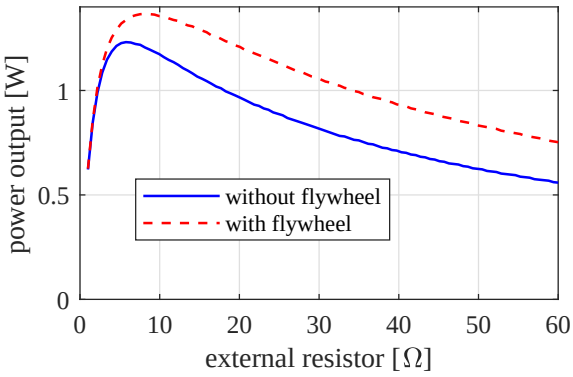


Figure 6.10: Harvested energy versus load resistance.

When the foot touches the top panel, both the top panel displacement y and generator rotational velocity $\dot{\theta}$ are small. The Coulomb damping T_f is designed to be small. As a result, the acceleration of the rotational angle $\theta = F_r/J_n$ will be large, i.e. the step force is mostly used to push the rotor to accelerate. This will lead to a large θ in a short time. As the one-way-clutch is engaged in this phase, the top panel will move down with the rack quickly. However, as shown in *Figure 6.4*, the step force F is small when the foot starts to touch the ground. The mechanical energy input to the tile $W = \int Fds$ will be small. This is illustrated by the no flywheel enclosed line area in *Figure 6.11*. In order to solve this problem and harvest more energy, a flywheel is added. The flywheel makes rotational inertia J large and hard to accelerate. Then the step force F reaches its full extent shortly after the foot touches the top panel. In this way, the mechanical energy input $W = \int Fds$ increases, as shown in by the flywheel line in *Figure 6.11*. This simulation is done by feeding the VGRF profile from the experiment to the system's equation of motion.

A numerical simulation of the system was performed to compare the three rotational inertia in *Figure 6.11*. The mechanical energy input to the energy harvesting tile is calculated by the enclosed area of the force-displacement loop. As the equivalent inertia increases, the mechanical energy input increases. The increase rate slows down and eventually reaches a maximum value, i.e. the potential energy. The reason is that the VGRF will increase due to the increase in the rotational inertia. However, the VGRF cannot exceed the force on solid ground as shown in *Figure 6.4* [9], because the motion of the tile will yield less VGRF compared with force yield by solid ground. So the mechanical energy input to the energy harvesting tile has a saturation relationship with the size of the flywheel. The input energy is small when the

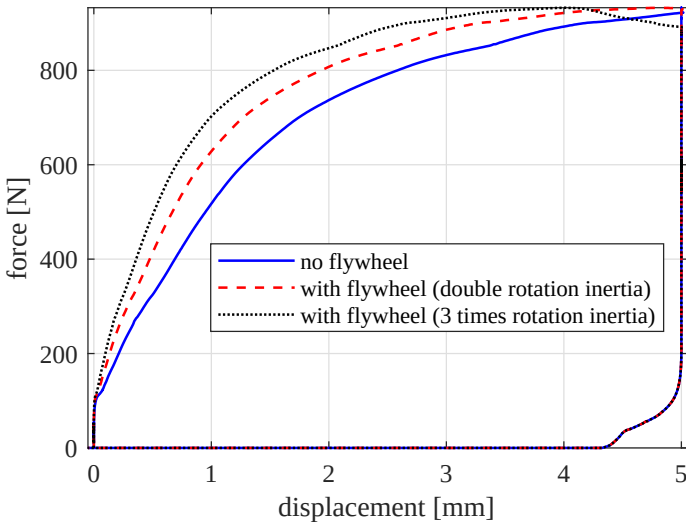


Figure 6.11: Comparison of force-displacement loop of the energy harvesting tile with different flywheel rotational inertia.

flywheel size is small. The input energy increases and eventually reaches a maximum value. The maximum value is equal to the theoretical potential energy.

The simulation result is obtained by inputting the vertical ground reaction force (VGRF) from experiments. However, the VGRF profile will change due to the change in the flywheel rotational inertia and external electrical load resistance. This is illustrated by the force profile with and without a flywheel in the experiment section. The change of force profile will result in a different displacement profile. The total mechanical energy input into the energy harvesting tile is the enclosed area by the force-displacement loop. As we cannot obtain the vertical ground reaction force for all the conditions we simulated, a typical vertical ground reaction force is used for all simulations. Because of this, the simulation results do not match the experimental results very well. The simulation is performed by using Coulomb friction estimated from experiments. However, the actual friction in the system will vary at different VGRFs and will be more complicated than the current model. In this sense, the numerical results only show the trend in the energy change to guide the design.

6.4 Experiments and evaluation

In order to verify the output power of the energy harvesting tile, we tested it using an Ozark Trail 500-Lumen Spotlight. It turns out that the harvested energy is enough to power the torch light at its specified conditions. The result is shown in *Figure 6.12*.



Figure 6.12: Experiment: upon stepping on the top panel, the prototype powers an Ozark Trail 500-Lumen Spotlight.

In order to compare the experimental results with the numerical simulation, evaluation sensors were employed to test the prototype. The tested setup is shown in *Figure 6.13*. A force sensor (PCB Model 208C03) is used to measure the VGRF on the top panel. A laser ranger (Micro Epsilon optoNCDT 1302) measures the displacement of the top panel. The system output is connected with a resistor (load resistance) to dissipate energy. The voltage on the resistor was measured. All the measurements were transferred to digital signal by a data acquisition system Coco-80 with three of its channels working simultaneously: voltage, displacement and force.

The force sensor was attached to the bottom of the test subject's shoes. The subject was asked to walk several steps in order to reach a steady speed. Then the subject stepped on the energy harvesting tile. The results of the experiment are shown in *Figure 6.14*, and are compared with numerical simulation using the same measured input VGRF fed to the system model.

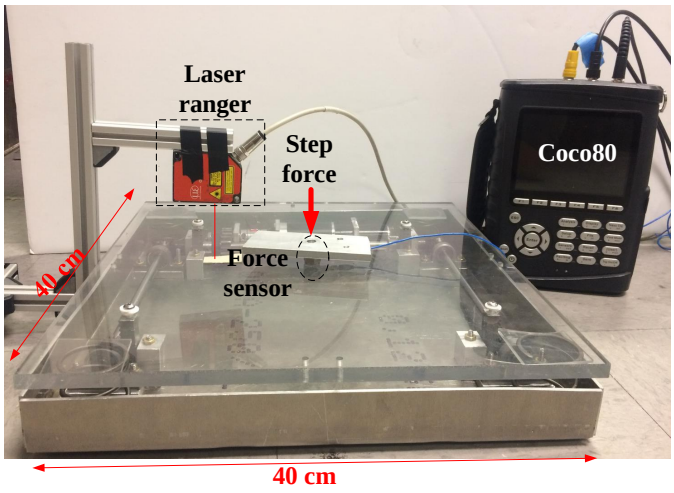


Figure 6.13: Test experiment setup.

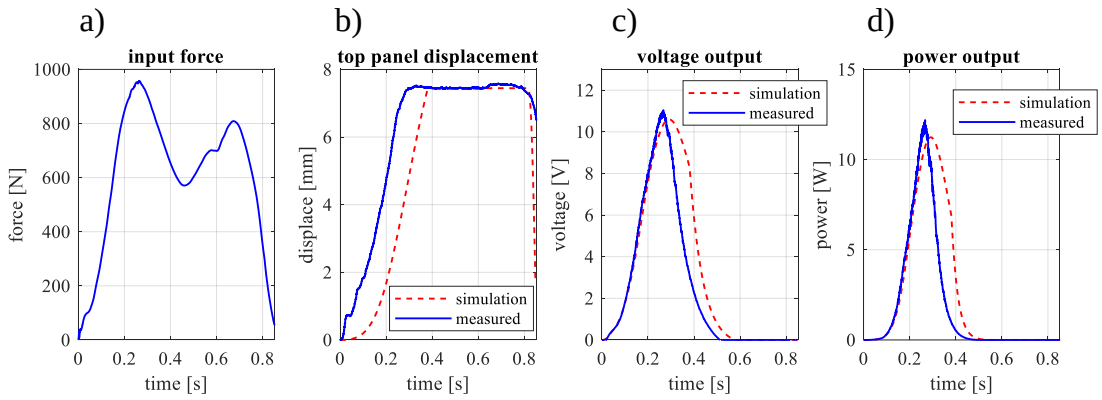


Figure 6.14: Experimental results: (a) Force input measured from experiments, (b) top panel displacement, (c) voltage output and (d) power output. The load resistance is 10 ω and the subject tested has a body weight of 80 kg.

As shown in *Figure 6.14*, the experimental results match quite well with the numerical simulation results. This verifies the accuracy of the presented model. The mismatch at the top panel displacement can be explained by the backlash in the gears and the deflection of the transmission system. The mismatch can be noted from the delay in the experimental top panel displacement and the simulation data in *Figure 6.14(a)*. The top panel displacement in this experiment is 7 mm, which is different from the designed 6 mm. Given the 400 mm 400 mm panel dimensions, a slight tilt of the top panel would easily result in a 1 2 mm displacement difference in the measurement. In order to find out the optimal resistance for maximizing the energy output per step, the relationship between the harvested energy and load resistance is mapped by changing the load resistance. The corresponding experimental results are shown in *Figure 6.15*.

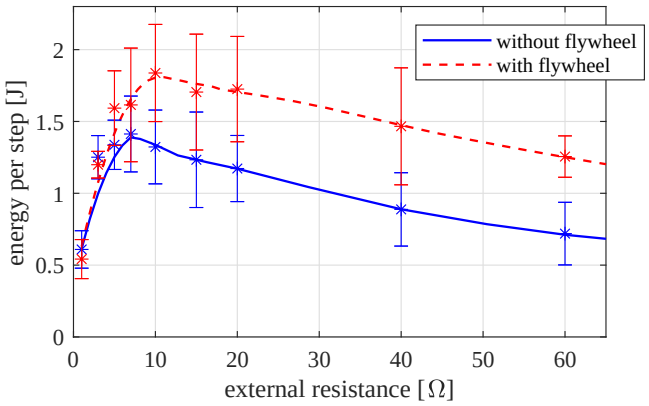


Figure 6.15: Energy harvesting performance with respect to the load resistance. The flywheel has 1.9 times the rotational inertia of the electric generator.

The average energy output from six individual tests is plotted with errorbar. A line is fitted to the experimental data. This line shows the general power output trend for both with and without flywheel cases. The flywheel has 1.9 times the rotational inertia compared with the generator rotor. Thus, the total rotational inertia in the case with the flywheel is 2.9 times the system without a flywheel. The average total energy for each step can be 1.8 J with the flywheel and a 10Ωload resistance. Aikaterini and Ji [48] [48] measured the human walking conditions in various locations, and estimated the average walking frequency to be around 2 Hz, i.e. the average step time is 0.5 s. Therefore, the average power output per person from the energy harvesting tile is 3.6 W. Considering the movement of the top panel of the energy harvesting tile is 6 mm, a total potential energy of 4.8 J can be obtained,

which is body weight times displacement (80kg × g × 6mm). This is shown by the enclosed dash rectangular area in *Figure 6.16(e) and (f)*. However, by analyzing the enclosed area of the force-displacement loop from the experiment, we found that 2.2 J (without flywheel) and 3.6 J (with flywheel) mechanical energy out of the 4.8 J maximum potential energy is input into the energy harvesting tile, which are 45.8% and 75% of the maximal potential energy. For the with flywheel case, the mechanical energy input into the tile increases by 63.6% compared with the case without a flywheel.

For the energy harvesting tile with flywheel, the total mechanical energy input is 3.6 J and the electrical energy output is 1.8 J, which indicates that 50% of mechanical energy is transferred into electric energy. The energy lost results from mechanical damping, friction, and motor efficiency loss. Without flywheel, 1.1 J of the 2.2 J mechanical energy input in converted into electricity. This indicates that flywheel increases the capture ratio of mechanical energy but didn't increase the energy conversion ratio from mechanical energy to electricity. The experiments so far are all based on normal walking conditions. In order to find out the influence of the flywheel in fast walking and running conditions, more experiments were performed and the results are shown in *Figure 6.17*.

As shown in *Figure 6.17*, the energy harvesting tile has more electrical energy output in faster walking conditions. This is because faster walking results in more vertical ground reaction force from impulse than slower walking and the flywheel stores more energy. The flywheel increases the amount of energy harvested for normal walking conditions. However, during fast walking and running conditions, the flywheel does not have an obvious effect of increasing energy output. The reason is that in the case with a flywheel, the force-displacement loop enclosed area is already close to saturation during walking conditions. (As shown by the rectangular enclosed area in *Figure 6.16(f)*. Fast walking and running will not make the enclosed loop significantly larger. For the case without flywheel, fast walking and running steps induce a larger acceleration motion of the harvester, which makes the force-displacement loop enclosed area much larger compared with normal walking conditions. This explains why the flywheel significantly increases the electricity output in normal walking but not in fast walking and running.

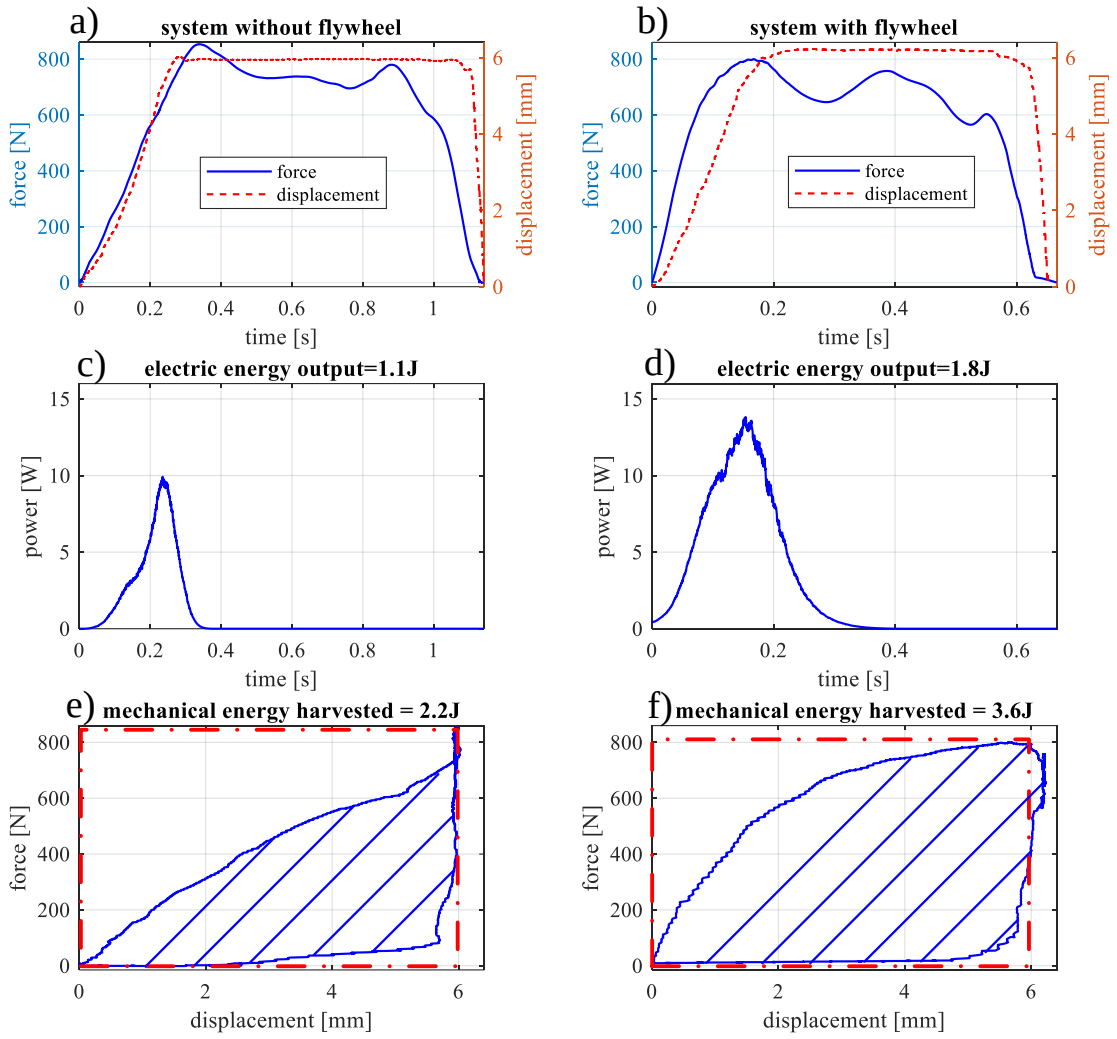


Figure 6.16: Force-displacement analysis: (a) time domain data of force and displacement of the system without flywheel; (b) time domain data of force and displacement of the system with flywheel (1.9 times of the generator rotational inertia); (c) time domain electric power output for the system without flywheel; (d) time domain electric power output for the system with flywheel; (e) force-displacement loop of the system without flywheel; (f) force-displacement loop of the system with flywheel.

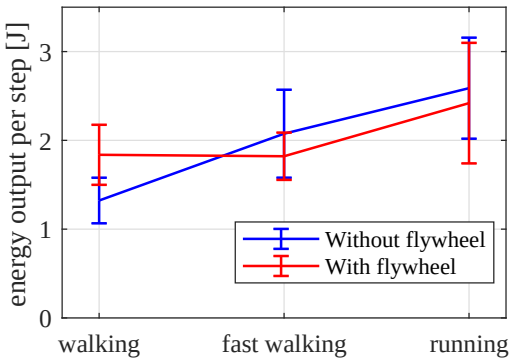


Figure 6.17: Energy output comparison of system with and without flywheel in walking, fast walking and running conditions.

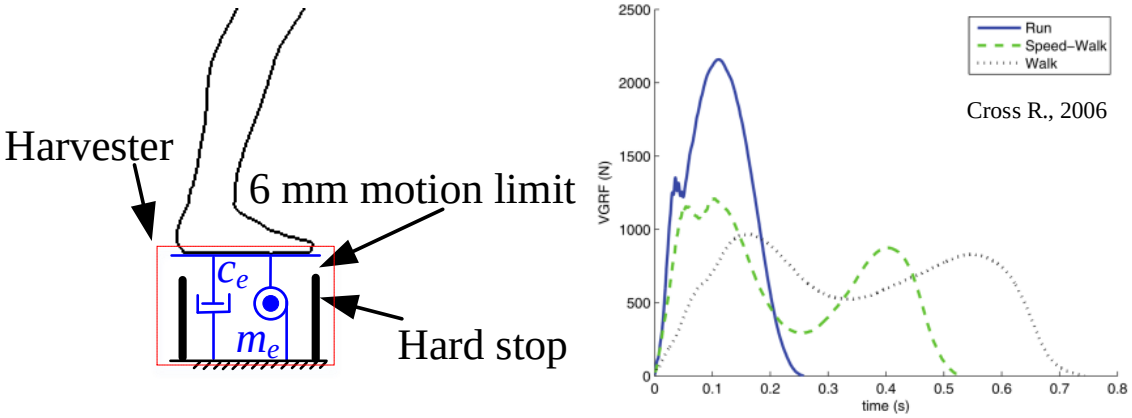


Figure 6.18: Modeling of the energy-harvesting paver (left) with its force input from foot.

6.5 Why the flywheel can improve the power performance

We have shown both by simulation and experiment that more power can be harvested by increasing the flywheel. The question here is why that is the case? In order to answer that question, I have built a model and prove it mathematically.

I have updated the figure to illustration more clearly. The human step force can be obtained from the literature. The motion of the energy harvester top panel is limited by 6 mm to not bother with human walking and ensure safety. The equation of motion is

$$VGRF = m_e\ddot{x} + c_e\dot{x} \tag{6.13}$$

where x is the top panel motion and maximums at 6 mm. The scientific question is how to obtain the maximum power within limited motion with a known force profile.

After the foot contacts the ground, the VGRF increases from $0N$ to $1000N$ in approximately $0.2s$ (observed from *Figure 6.4*, the walking case). The problem is simplified as obtain the largest energy in the step function force. The equation of motion is

$$VGRF = m_e\ddot{x} + c_e\dot{x} \tag{6.14}$$

With input as

$$VGRF(t) = 5000t \tag{6.15}$$

The Laplace transform of the displace x is

$$x(t) = \frac{VGRF(t)}{m_e s^2 + c_e s} \tag{6.16}$$

with Laplace transform of the input as

$$F(VGRF(t)) = \frac{5000}{s^2} \tag{6.17}$$

Then the response is

$$\begin{aligned} &X(s) = L(x(t)) = \tfrac{L(VGRF(t))}{c_e s + m_e s^2} = \tfrac{5000}{s^2}\tfrac{1}{c_e s + m_e s^2} \\ &= \tfrac{5000}{c_e}\tfrac{1}{s^3} - \tfrac{m_e}{c_e s^2} + \tfrac{m_e^2}{c_e^2 s} - \tfrac{m_e^2}{c_e^2}\tfrac{1}{s + c_e/m_e} \end{aligned} \tag{6.18}$$

Inverse Laplace transform can obtain

$$x(t) = L^{-1}(X(s)) = \frac{5000}{c_e}[\frac{t^2}{2} - \frac{m_e}{c_e}t + \frac{m_e^2}{c_e^2} - \frac{m_e^2}{c_e^2}e^{-\frac{c_e}{m_e}t}] \tag{6.19}$$

As the Taylor series of $e^{-\frac{c_e}{m_e}t} = 1 - \frac{c_e}{m_e}t + \frac{c_e^2}{m_e^2}\frac{t^2}{2} - \frac{c_e^3}{m_e^3}\frac{t^3}{6} + O(t^2)$,

$$\begin{aligned} &x(t) = 5000/c_e[\tfrac{t^2}{2} - \tfrac{m_e}{c_e}t + \tfrac{m_e^2}{c_e^2} - \tfrac{m_e^2}{c_e^2}(1 - \tfrac{c_e}{m_e}t + \tfrac{c_e^2}{m_e^2}\tfrac{t^2}{2} - \tfrac{c_e^3}{m_e^3}\tfrac{t^3}{6} + O(t^3))] \\ &= \tfrac{5000}{c_e}[\tfrac{t^2}{2} - \tfrac{m_e}{c_e}t + \tfrac{m_e^2}{c_e^2} - \tfrac{m_e^2}{c_e^2} + \tfrac{m_e}{c_e}t - \tfrac{t^2}{2} + \tfrac{c_e}{m_e}\tfrac{t^3}{6} + O(t^3)] \\ &= 5000[\tfrac{1}{m_e}\tfrac{t^3}{6} + O(t^3)] \\ &\approx \tfrac{2500t^3}{3m_e} \end{aligned} \tag{6.20}$$

Solve

$$\frac{2500t^3}{3m_e} = 0.006 \tag{6.21}$$

and obtain

$$t_0 = \sqrt[3]{\frac{0.018m_e}{2500}} \tag{6.22}$$

From $x(t)$ obtain $\dot{x}(t)$

$$\dot{x}(t) = \frac{2500t^2}{m_e} \tag{6.23}$$

Then the power harvested is

$$P = Fv = F\dot{x}(t) = 5000t\frac{2500t^2}{m_e} = 5000^2\frac{t^3}{2m_e} \tag{6.24}$$

Then the energy collected is the integration of the power over time

$$\begin{aligned} &E = \textstyle\int_0^{t_0} 5000^2\frac{1}{m_e}\frac{t^3}{2}dt \\ &= 5000^2\frac{1}{m_e}\frac{t^4}{8}\Big|_0^{\sqrt[3]{\frac{0.018m_e}{2500}}} \\ &= 5000^2\frac{0.018m_e}{2500}^{\frac{4}{3}}\frac{1}{8m_e} \\ &= 5000^2\frac{0.018}{2500}^{\frac{4}{3}}\frac{m_e^{\frac{1}{3}}}{8} \end{aligned} \tag{6.25}$$

Then do partial differential equation of energy E over m_e, which will lead to

$$\frac{\partial E}{\partial m_e} = 5000^2 \frac{\sqrt[\frac{4}{3}]{\frac{0.018}{2500}})}{8} \frac{1}{3} m_e^{-\frac{2}{3}} > 0 \tag{6.26}$$

This indicates that the energy harvested will increase as the increase of m_e.As a result, this proves mathematically that increase of m_e will increase the power harvested. If the force is closer to a step response, such as in the case of running, the power harvested is closer to $W = FS$, which F is force and S is travel distance, in this case it is $0.006m$. As a result, the energy harvested is a fixed value. This analysis explains why in the experiment, the flywheel cannot increase the energy harvested in the running case.

Chapter conclusions

We presented the design, modeling, analysis, simulations, and experimental tests of a novel high-efficiency energy harvesting tile. Based on the novel design, high power output and high energy harvesting efficiency are obtained. A complete dynamic model is developed. Based on the modeling and simulation, optimal parameters are obtained. The role of the components, such as load resistance and the flywheel, is analyzed and discussed in order to harvest more energy at a high rate of efficiency. The flywheel's influence on energy harvesting in walking, fast walking, and running conditions are compared and discussed. The experimental results match well with numerical simulations. For the first time, the design criteria of electromagnetic based energy harvester tile are presented The experimental results show that the energy harvesting tile can produce an average power output of 3.6 W over 0.5 seconds of the step time, with a peak power of 12 W in walking conditions. The output electrical energy is 1.8 J per step. 75% of all the theoretically available potential energy is transmitted into the energy harvesting tile and 50% of them converted into electricity. This is significantly higher than the values published in the literature. The top panel displacement is around 6 mm, which will likely have a negligible effect on the pedestrian's walking behavior. By increasing the amount of harvested energy at small tile top panel movement, this paper shows an applicable amount of energy can be obtained while not affect human walking. The presented dynamic model, analytic method, and optimization method can also be used in the design of similar vibration energy harvesting devices.

Chapter 7

Conclusions and future work

In this dissertation, different topics on energy harvesting from the human body for mobile and wearable devices are presented.

1. An energy harvesting backpack is built. Mechanical Motion Rectifier (MMR) was introduced to the energy harvesting system and makes the generator rotates in one direction instead of rotating back-and-forth, thus decrease the inertia term and increase the frequency bandwidth.

2. One more spring is added and by taking advantage of the inerter in the generator, a large equivalent mass can be achieved by using a small physical mass. In this way, one more degree of freedom is obtained, and thus having two resonance frequencies instead of one. Large power can be obtained by tuning the two resonance frequencies around the target frequency. This leads to more power output and thus the benefits of the 2DOF system are obtained without adding a large physical mass.

3. By adding MMR to the 2DOF system, the effect of the equivalent mass of the generator rotor m_e is decreased and the stroke response is frequency domain is much more flat. This result in a small peak stroke.

4. A harvester is designed to harvest negative work from human walking while does not impede normal human gait. This is the first harvester designed on the ankle to harvest negative work with experimental validation. Pilot experiments (with the hu-

man participant as the first author himself) show that the device harvests $0.3 \pm 0.05W$ of power and works at the muscle negative work phase, and is trying to assist the muscle. A model of the harvester is built to guide the harvester design.

5. Designed an energy harvesting tile/paver that can harvest the impact energy in human walking. The system harvests the most power while the effect on normal human walking is controlled. The modeling of the human foot and the harvester is built. The modeling points out how and why more power can be harvested by parameter tuning. The modeling is validated by experiment.

The future work is summarized as follows:

1. In the backpack design, the human body is considered as a constant fixed amplitude sinusoidal vertical input to the backpack. However, in the real application, there might be an interaction between the human body and the energy harvesting backpack. Future work should be done either by modeling and/or experiment to find out the inter influence between the human body and the energy harvesting backpack.

2. Even though it is shown by the pilot experiment (by the author himself) that the negative energy harvester harvests energy from the negative muscle work phase, no solid experiment is done to show that the harvester is assisting the human walking, and no validation has shown that the negative harvester will not increase the metabolic cost required for walking. Future work should recruit multiple participants to statistically show that the negative energy harvester will assist human walking and will not increase the metabolic required for walking.

3. In terms of energy harvesting and the extra metabolic cost for harvester weight carrying, none of the previous work or the work in this dissertation has reached the critical point (i.e. the power harvested is the same as the extra metabolic cost of weight carriage). Further work still needs to be done to increase the power output, and decrease the device weight.

4. Although this dissertation present pioneer work and the cost has not taken into consideration, a real application has to consider the cost v.s. benefit, and compete with currently existing technologies (such as batteries). In order to make the energy

harvester practical, future work should be done to make the harvester low in cost and practical for everyday use.

5. When designing the energy harvesting backpack, more consideration is put on the power output, broad bandwidth. Human comfort is simply considered by having a stroke control. There should be some trade-off between the energy harvesting and human comfort but the details are not clear. Future work can focus on this trade-off and figure how to balance those two.

Bibliography

[1] R. Riemer, A. Shapiro, Biomechanical energy harvesting from human motion: theory, state of the art, design guidelines, and future directions, Journal of neuroengineering and rehabilitation 8 (1) (2011) 22.

[2] S. H. Collins, M. B. Wiggin, G. S. Sawicki, Reducing the energy cost of human walking using an unpowered exoskeleton, Nature 522 (7555) (2015) 212–215.

[3] J. M. Donelan, Q. Li, V. Naing, J. A. Hoffer, D. Weber, A. D. Kuo, Biomechanical energy harvesting: generating electricity during walking with minimal user effort, Science 319 (5864) (2008) 807–810.

[4] L. C. Rome, L. Flynn, E. M. Goldman, T. D. Yoo, Generating electricity while walking with loads, Science 309 (5741) (2005) 1725–1728.

[5] L. C. Rome, L. Flynn, T. D. Yoo, Rubber bands reduce the cost of carrying loads, Nature 444 (7122) (2006) 1023–1024.

[6] M. Liu, W.-C. Tai, L. Zuo, Enhanced vibration energy-harvesting using inerter-based two-degree-of-freedom system, in: ASME 2018 Dynamic Systems and Control Conference, American Society of Mechanical Engineers Digital Collection, 2018.

[7] M. Liu, W.-C. Tai, L. Zuo, Toward broadband vibration energy harvesting via mechanical motion-rectification induced inertia nonlinearity, Smart Materials and Structures 27 (7) (2018) 075022.

[8] D. A. Winter, Biomechanics and motor control of human movement, John Wiley & Sons, 2009.

[9] R. Cross, Standing, walking, running, and jumping on a force plate, American Journal of Physics 67 (4) (1999) 304–309.

[10] S. Priya, D. J. Inman, Energy harvesting technologies, Vol. 21, Springer, 2009.

[11] R. Kurzweil, The singularity is near: When humans transcend biology, Penguin, 2005.

[12] T. Starner, Human-powered wearable computing, IBM systems Journal 35 (3.4) (1996) 618–629.

[13] T. M. Griffin, T. J. Roberts, R. Kram, Metabolic cost of generating muscular force in human walking: insights from load-carrying and speed experiments, Journal of Applied Physiology 95 (1) (2003) 172–183.

[14] V. Leonov, Thermoelectric energy harvesting of human body heat for wearable sensors, IEEE Sensors Journal 13 (6) (2013) 2284–2291.

[15] J. Granstrom, J. Feenstra, H. A. Sodano, K. Farinholt, Energy harvesting from a backpack instrumented with piezoelectric shoulder straps, Smart Materials and Structures 16 (5) (2007) 1810.

[16] C. Yao, A. Hernandez, Y. Yu, Z. Cai, X. Wang, Triboelectric nanogenerators and power-boards from cellulose nanofibrils and recycled materials, Nano Energy 30 (2016) 103–108.

[17] L. Zuo, X. Tang, Large-scale vibration energy harvesting, Journal of intelligent material systems and structures 24 (11) (2013) 1405–1430.

[18] V. Radhakrishnan, Locomotion: Dealing with friction, Proceedings of the National Academy of Sciences 95 (10) (1998) 5448–5455.

[19] P. DeVita, J. Helseth, T. Hortobagyi, Muscles do more positive than negative work in human locomotion, Journal of Experimental Biology 210 (19) (2007) 3361–3373.

[20] T. Ryschon, M. Fowler, R. Wysong, A.-R. Anthony, R. Balaban, Efficiency of human skeletal muscle in vivo: comparison of isometric, concentric, and eccentric muscle action, Journal of applied physiology 83 (3) (1997) 867–874.

[21] N. G. Stephen, On energy harvesting from ambient vibration, Journal of sound and vibration 293 (1-2) (2006) 409–425.

[22] C. Williams, R. B. Yates, Analysis of a micro-electric generator for microsystems, in: Proceedings of the International Solid-State Sensors and Actuators Conference-TRANSDUCERS'95, Vol. 1, IEEE, 1995, pp. 369–372.

[23] N. Elvin, A. Erturk, Advances in energy harvesting methods, Springer Science & Business Media, 2013.

[24] D. Zhu, M. J. Tudor, S. P. Beeby, Strategies for increasing the operating frequency range of vibration energy harvesters: a review, Measurement Science and Technology 21 (2) (2009) 022001.

[25] A. V. Rowlands, M. R. Stone, R. G. Eston, Influence of speed and step frequency during walking and running on motion sensor output, Medicine & Science in Sports & Exercise 39 (4) (2007) 716–727.

[26] E. S. Leland, P. K. Wright, Resonance tuning of piezoelectric vibration energy scavenging generators using compressive axial preload, Smart Materials and Structures 15 (5) (2006) 1413.

[27] R. Ramlan, M. Brennan, B. Mace, I. Kovacic, Potential benefits of a non-linear stiffness in an energy harvesting device, Nonlinear dynamics 59 (4) (2010) 545–558.

[28] X. Wu, J. Lin, S. Kato, K. Zhang, T. Ren, L. Liu, A frequency adjustable vibration energy harvester, Proceedings of PowerMEMS (2008) 245–248.

[29] F. Cottone, H. Vocca, L. Gammaitoni, Nonlinear energy harvesting, Physical Review Letters 102 (8) (2009) 080601.

[30] L. Gu, C. Livermore, Passive self-tuning energy harvester for extracting energy from rotational motion, Applied Physics Letters 97 (8) (2010) 081904.

[31] M. Soliman, E. Abdel-Rahman, E. El-Saadany, R. Mansour, A wideband vibration-based energy harvester, Journal of micromechanics and microengineering 18 (11) (2008) 115021.

[32] S. Shahruz, Design of mechanical band-pass filters for energy scavenging, Journal of sound and vibration 292 (3-5) (2006) 987–998.

[33] D. Upadrashta, Y. Yang, Nonlinear piezomagnetoelastic harvester array for broadband energy harvesting, Journal of Applied Physics 120 (5) (2016) 054504.

[34] X. Tang, T. Lin, L. Zuo, Design and optimization of a tubular linear electromagnetic vibration energy harvester, IEEE/ASME Transactions on Mechatronics 19 (2) (2013) 615–622.

[35] Z. Li, L. Zuo, J. Kuang, G. Luhrs, Energy-harvesting shock absorber with a mechanical motion rectifier, Smart materials and structures 22 (2) (2012) 025008.

[36] I. L. Cassidy, Modeling and control of an electromagnetic transducer for vibratory energy harvesting applications, in: Masters Abstracts International, Vol. 50-01, 2011.

[37] Z. Li, L. Zuo, G. Luhrs, L. Lin, Y.-x. Qin, Electromagnetic energy-harvesting shock absorbers: design, modeling, and road tests, IEEE Transactions on vehicular technology 62 (3) (2012) 1065–1074.

[38] M. C. Smith, Synthesis of mechanical networks: the inerter, IEEE Transactions on automatic control 47 (10) (2002) 1648–1662.

[39] Y. Liu, C.-C. Lin, J. Parker, L. Zuo, Exact h2 optimal tuning and experimental verification of energy-harvesting series electromagnetic tuned-mass dampers, Journal of Vibration and Acoustics 138 (6).

[40] P. Li, L. Zuo, Equivalent circuit modeling of vehicle dynamics with regenerative shock absorbers, in: ASME 2013 International Design Engineering Technical Conferences and Computers and Information in Engineering Conference, American Society of Mechanical Engineers Digital Collection, 2013.

[41] C. Liang, Y. Wu, L. Zuo, Broadband pendulum energy harvester, Smart Materials and Structures 25 (9) (2016) 095042.

[42] Y. Kawamoto, Y. Suda, H. Inoue, T. Kondo, Modeling of electromagnetic damper for automobile suspension, Journal of system design and dynamics 1 (3) (2007) 524–535.

[43] P. N. Barnes, M. D. Sumption, G. L. Rhoads, Review of high power density superconducting generators: Present state and prospects for incorporating ybco windings, Cryogenics 45 (10-11) (2005) 670–686.

[44] L. Zuo, G. R. Penamalli, J. Wang, R. H. Zheng, X. H. Lei, J. F. Lam-Ki, Z. Li, T. Lin, High-efficiency energy generator for harnessing mechanical vibration power, uS Patent 9,394,876 (Jul. 19 2016).

[45] A. Pourghodrat, Energy harvesting systems design for railroad safety.

[46] C. Liang, J. Ai, L. Zuo, Design, fabrication, simulation and testing of an ocean wave energy converter with mechanical motion rectifier, Ocean Engineering 136 (2017) 190–200.

[47] S. Guo, L. Xu, Y. Liu, X. Guo, L. Zuo, Performances of energy-harvesting shock absorbers on various types of vehicles, in: ASME 2015 Dynamic Systems and Control Conference, American Society of Mechanical Engineers Digital Collection, 2015.

[48] T. Ji, A. Pachi, Frequency and velocity of people walking, Structural Engineer 84 (3) (2005) 36–40.

[49] G. Gebresenbet, S. Aradom, F. S. Bulitta, E. Hjerpe, Vibration levels and frequencies on vehicle and animals during transport, Biosystems Engineering 110 (1) (2011) 10–19.

[50] S. S. Rao, Mechanical Vibrations Laboratory Manual, Year, Edition Addison-Wesley Publishing Company, 1995.

[51] H. Zhang, L. R. Corr, T. Ma, Issues in vibration energy harvesting, Journal of Sound and Vibration 421 (2018) 79–90.

[52] S. A. Gard, S. C. Miff, A. D. Kuo, Comparison of kinematic and kinetic methods for computing the vertical motion of the body center of mass during walking, Human movement science 22 (6) (2004) 597–610.

[53] L. Wang, P. Todaria, A. Pandey, J. O'Connor, B. Chernow, L. Zuo, An electromagnetic speed bump energy harvester and its interactions with vehicles, IEEE/ASME Transactions on Mechatronics 21 (4) (2016) 1985–1994.

[54] M. Liu, R. Lin, S. Zhou, Y. Yu, A. Ishida, M. McGrath, B. Kennedy, M. Hajj, L. Zuo, Design, simulation and experiment of a novel high efficiency energy harvesting paver, Applied energy 212 (2018) 966–975.

[55] D. J. Inman, R. C. Singh, Engineering vibration, Vol. 3, Prentice Hall Englewood Cliffs, NJ, 1994.

[56] L. Tang, Y. Yang, C. K. Soh, Broadband vibration energy harvesting techniques, in: Advances in energy harvesting methods, Springer, 2013, pp. 17–61.

[57] V. Chonhenchob, S. P. Singh, J. J. Singh, J. Stallings, G. Grewal, Measurement and analysis of vehicle vibration for delivering packages in small-sized and medium-sized trucks and automobiles, Packaging Technology and Science 25 (1) (2012) 31–38.

[58] S. Roundy, E. S. Leland, J. Baker, E. Carleton, E. Reilly, E. Lai, B. Otis, J. M. Rabaey, P. K. Wright, V. Sundararajan, Improving power output for vibration-based energy scavengers, IEEE Pervasive computing 4 (1) (2005) 28–36.

[59] I.-H. Kim, H.-J. Jung, B. M. Lee, S.-J. Jang, Broadband energy-harvesting using a two degree-of-freedom vibrating body, Applied Physics Letters 98 (21) (2011) 214102.

[60] P. S. Ma, J. E. Kim, Y. Y. Kim, Power-amplifying strategy in vibration-powered energy harvesters, in: Active and Passive Smart Structures and Integrated Systems 2010, Vol. 7643, International Society for Optics and Photonics, 2010, p. 76430O.

[61] X. Tang, L. Zuo, Enhanced vibration energy harvesting using dual-mass systems, Journal of sound and vibration 330 (21) (2011) 5199–5209.

[62] O. Aldraihem, A. Baz, Energy harvester with a dynamic magnifier, Journal of Intelligent Material Systems and Structures 22 (6) (2011) 521–530.

[63] A. Aladwani, M. Arafa, O. Aldraihem, A. Baz, Cantilevered piezoelectric energy harvester with a dynamic magnifier, Journal of vibration and acoustics 134 (3).

[64] W. Zhou, G. R. Penamalli, L. Zuo, An efficient vibration energy harvester with a multi-mode dynamic magnifier, Smart Materials and Structures 21 (1) (2011) 015014.

[65] M. Peigney, D. Siegert, Piezoelectric energy harvesting from traffic-induced bridge vibrations, Smart Materials and Structures 22 (9) (2013) 095019.

[66] X. Tang, L. Zuo, Regenerative semi-active control of tall building vibration with series tmds, in: Proceedings of the 2010 American Control Conference, IEEE, 2010, pp. 5094–5099.

[67] L. Xie, M. Cai, Increased energy harvesting and reduced accelerative load for backpacks via frequency tuning, Mechanical Systems and Signal Processing 58 (2015) 399–415.

[68] A. Waterbury, S. Lin, P. Wright, Vibration energy harvesting from the unsprung suspension of a vehicle for asset monitoring using an electromagnetic transducer (2012).

[69] J. Scruggs, Causal control design for wave energy converters with finite stroke, IFAC-PapersOnLine 50 (1) (2017) 15678–15685.

[70] J. Kymissis, C. Kendall, J. Paradiso, N. Gershenfeld, Parasitic power harvesting in shoes, in: Digest of Papers. Second International Symposium on Wearable Computers (Cat. No. 98EX215), IEEE, 1998, pp. 132–139.

[71] J. Elmes, V. Gaydarzhiev, A. Mensah, K. Rustom, J. Shen, I. Batarseh, Maximum energy harvesting control for oscillating energy harvesting systems, in: 2007 IEEE Power Electronics Specialists Conference, IEEE, 2007, pp. 2792–2798.

[72] Z. Yang, A. Khaligh, A flat linear generator with axial magnetized permanent magnets with reduced accelerative force for backpack energy harvesting, in: 2012 Twenty-Seventh Annual IEEE Applied Power Electronics Conference and Exposition (APEC), IEEE, 2012, pp. 2534–2541.

[73] Y. Yuan, M. Liu, W.-C. Tai, L. Zuo, Design and experimental studies of an energy harvesting backpack with mechanical motion rectification, in: Sensors and Smart Structures Technologies for Civil, Mechanical, and Aerospace Systems 2017, Vol. 10168, International Society for Optics and Photonics, 2017, p. 1016825.

[74] S. Pakdelian, A compact and light-weight generator for backpack energy harvesting, in: 2016 IEEE Energy Conversion Congress and Exposition (ECCE), IEEE, 2016, pp. 1–8.

[75] E. A. Hansen, L. A. R. Kristensen, A. M. Nielsen, M. Voigt, P. Madeleine, The role of stride frequency for walk-to-run transition in humans, Scientific reports 7 (1) (2017) 1–8.

[76] Y. Liu, L. Xu, L. Zuo, Design, modeling, lab, and field tests of a mechanical-motion-rectifier-based energy harvester using a ball-screw mechanism, IEEE/ASME Transactions on mechatronics 22 (5) (2017) 1933–1943.

[77] X. Xu, et al., An investigation on the interactivity between suspended-load backpack and human gait.

[78] P. E. Gill, W. Murray, M. H. Wright, Practical optimization, SIAM, 2019.

[79] T. Starner, J. A. Paradiso, Human generated power for mobile electronics, Low-power electronics design 45 (2004) 1–35.

[80] E. Romero-Ramirez, Energy harvesting from body motion using rotational micro-generation.

[81] A. Carroll, G. Heiser, et al., An analysis of power consumption in a smartphone., in: USENIX annual technical conference, Vol. 14, Boston, MA, 2010, pp. 21–21.

[82] Y.-M. Choi, M. G. Lee, Y. Jeon, Wearable biomechanical energy harvesting technologies, Energies 10 (10) (2017) 1483.

[83] G. Zhu, Z.-H. Lin, Q. Jing, P. Bai, C. Pan, Y. Yang, Y. Zhou, Z. L. Wang, Toward large-scale energy harvesting by a nanoparticle-enhanced triboelectric nanogenerator, Nano letters 13 (2) (2013) 847–853.

[84] N. S. Shenck, J. A. Paradiso, Energy scavenging with shoe-mounted piezoelectrics, IEEE micro 21 (3) (2001) 30–42.

[85] S. Boisseau, G. Despesse, B. A. Seddik, Electrostatic conversion for vibration energy harvesting, Small-Scale Energy Harvesting (2012) 1–39.

[86] J. A. Paradiso, M. Feldmeier, A compact, wireless, self-powered pushbutton controller, in: International Conference on Ubiquitous Computing, Springer, 2001, pp. 299–304.

[87] T. Wacharasindhu, J. Kwon, A micromachined energy harvester from a keyboard using combined electromagnetic and piezoelectric conversion, Journal of Micromechanics and Microengineering 18 (10) (2008) 104016.

[88] S. Schmitt, M. Günther, Human leg impact: energy dissipation of wobbling masses, Archive of Applied Mechanics 81 (7) (2011) 887–897.

[89] L. Kemball-Cook, P. Tucker, Energy harvesting, uS Patent 8,736,088 (May 27 2014).

[90] A. D. Kuo, The six determinants of gait and the inverted pendulum analogy: A dynamic walking perspective, Human movement science 26 (4) (2007) 617–656.

[91] Terminology of human walking, North American Society for Gait and Human Movement.

[92] S. C. Walpole, D. Prieto-Merino, P. Edwards, J. Cleland, G. Stevens, I. Roberts, The weight of nations: an estimation of adult human biomass, BMC public health 12 (1) (2012) 439.

[93] K. E. Zelik, T.-W. P. Huang, P. G. Adamczyk, A. D. Kuo, The role of series ankle elasticity in bipedal walking, Journal of theoretical biology 346 (2014) 75–85.

[94] M. Liu, W.-C. Tai, L. Zuo, Energy harvesting from ankle: Generating electricity by harvesting negative work, in: ASME 2018 Conference on Smart Materials, Adaptive Structures and Intelligent Systems, American Society of Mechanical Engineers Digital Collection, 2018.

[95] M. Cai, W.-H. Liao, J. Cao, A smart harvester for capturing energy from human ankle dorsiflexion with reduced user effort, Smart Materials and Structures 28 (1) (2018) 015026.

[96] J. E. Bertram, Constrained optimization in human walking: cost minimization and gait plasticity, Journal of experimental biology 208 (6) (2005) 979–991.

[97] R. C. Browning, J. R. Modica, R. Kram, A. Goswami, The effects of adding mass to the legs on the energetics and biomechanics of walking, Medicine & Science in Sports & Exercise 39 (3) (2007) 515–525.

[98] J. M. Batalla, G. Mastorakis, C. X. Mavromoustakis, E. Pallis, Beyond the Internet of Things, Springer, 2017.

[99] P. Mane, J. Xie, K. K. Leang, K. Mossi, Cyclic energy harvesting from pyroelectric materials, IEEE transactions on ultrasonics, ferroelectrics, and frequency control 58 (1) (2011) 10–17.

[100] M. F. Daqaq, Transduction of a bistable inductive generator driven by white and exponentially correlated gaussian noise, Journal of Sound and Vibration 330 (11) (2011) 2554–2564.

[101] X. Wang, C. Chen, N. Wang, H. San, Y. Yu, E. Halvorsen, X. Chen, A frequency and bandwidth tunable piezoelectric vibration energy harvester using multiple nonlinear techniques, Applied energy 190 (2017) 368–375.

[102] S. Zhou, J. Cao, D. J. Inman, J. Lin, S. Liu, Z. Wang, Broadband tristable energy harvester: modeling and experiment verification, Applied Energy 133 (2014) 33–39.

[103] S. P. Beeby, R. Torah, M. Tudor, P. Glynne-Jones, T. O'donnell, C. Saha, S. Roy, A micro electromagnetic generator for vibration energy harvesting, Journal of Micromechanics and microengineering 17 (7) (2007) 1257.

[104] B. Mann, N. Sims, Energy harvesting from the nonlinear oscillations of magnetic levitation, Journal of sound and vibration 319 (1-2) (2009) 515–530.

[105] A. Costanzo, M. Dionigi, D. Masotti, M. Mongiardo, G. Monti, L. Tarricone, R. Sorrentino, Electromagnetic energy harvesting and wireless power transmission: A unified approach, Proceedings of the IEEE 102 (11) (2014) 1692–1711.

[106] D. Younesian, M.-R. Alam, Multi-stable mechanisms for high-efficiency and broadband ocean wave energy harvesting, Applied energy 197 (2017) 292–302.

[107] P. D. Mitcheson, E. M. Yeatman, G. K. Rao, A. S. Holmes, T. C. Green, Energy harvesting from human and machine motion for wireless electronic devices, Proceedings of the IEEE 96 (9) (2008) 1457–1486.

[108] H. Fu, R. Xu, K. Seto, E. Yeatman, S. Kim, Energy harvesting from human motion using footstep-induced airflow, in: Journal of Physics: Conference Series, Vol. 660, IOP Publishing, 2015, p. 012060.

[109] S. Wu, P. C.-K. Luk, C. Li, X. Zhao, Z. Jiao, Y. Shang, An electromagnetic wearable 3-dof resonance human body motion energy harvester using ferrofluid as a lubricant, Applied Energy 197 (2017) 364–374.

[110] T.-H. Hsu, S. Manakasettharn, J. A. Taylor, T. Krupenkin, Bubbler: a novel ultra-high power density energy harvesting method based on reverse electrowetting, Scientific reports 5 (2015) 16537.

[111] A. Dawson, R. Mallick, A. G. Hernandez, P. K. Dehdezi, Energy harvesting from pavements, in: Climate Change, Energy, Sustainability and Pavements, Springer, 2014, pp. 481–517.

[112] H. Zhao, J. Ling, J. Yu, A comparative analysis of piezoelectric transducers for harvesting energy from asphalt pavement, Journal of the Ceramic Society of Japan 120 (1404) (2012) 317–323.

[113] H. Xiong, L. Wang, Piezoelectric energy harvester for public roadway: On-site installation and evaluation, Applied Energy 174 (2016) 101–107.

[114] N. Sharpes, D. Vučković, S. Priya, Floor tile energy harvester for self-powered wireless occupancy sensing, Energy Harvesting and Systems 3 (1) (2016) 43–60.

[115] S. Taliyan, B. Biswas, R. Patil, G. Srivastava, T. Basu, Electricity from footsteps, IEEE Trans. On Power Generation 23 (4) (2010) 2521–2530.

[116] A. with Disabilities Act, Accessibility guidelines for buildings and facilities (2000).

[117] A. Bhatia, V. Sanghwan, T. Kaistha, V. Varshney, S. Dalal, Energy harvesting through footsteps, Int J Adv Res Technol 1 (2016) 405–412.

[118] F. Duarte, F. Casimiro, D. Correia, R. Mendes, A. Ferreira, A new pavement energy harvest system, in: 2013 International Renewable and Sustainable Energy Conference (IRSEC), IEEE, 2013, pp. 408–413.

[119] A. Tongen, R. E. Wunderlich, Biomechanics of running and walking, Mathematics and Sports 43 (2010) 1–12.